Probing the Stability of Nickel Phosphide Nanoparticle Electrocatalysts via Advanced Benchtop X-ray Spectroscopy

Ricardo Andres Rivera-Maldonado

A dissertation

submitted in partial fulfillment of the

requirements for the degree of

Doctor of Philosophy

University of Washington

2024

Reading Committee:

Brandi Cossairt, Chair

Gerald T. Seidler

Dianne Xiao

Program Authorized to Offer Degree:

Chemistry

University of Washington

Abstract

Probing the Stability of Nickel Phosphide Nanoparticle Electrocatalysts via Advanced Benchtop X-ray Spectroscopy

Ricardo Andres Rivera-Maldonado

Chair of the Supervisory Committee:
Brandi Cossairt
Department of Chemistry

The electrification of the petrochemical industry will significantly reduce greenhouse gas emissions in the manufacturing of commodity chemicals; however, electrification on a global scale is only achievable using earth-abundant materials for electrocatalysis in place of state-of-the-art catalysts made from precious metals. A promising catalyst that has been used for industrial hydrodesulfurization and electrocatalytic hydrogen evolution, nitrate reduction, carbon dioxide reduction, and oxygen evolution is Ni_2P. Ni_2P and other transition metal phosphides benefit from active site ensembles that moderate the binding of reaction intermediates, making them promising electrocatalysts for reactions beyond the ones listed, especially other hydrogenation reactions. However, Ni_2P and other TMPs are susceptible to oxidation, leading to catalyst degradation and loss in certain conditions. Stability is an important part of catalysis; therefore, it is important to

understand the degradation mechanism of Ni_2P in order to mitigate corrosion, accurately predict surface reactivity, and prepare Ni_2P for industrial electrocatalysis. In the present work, *operando* Ni K-edge X-ray absorption spectroscopy (XAS) and *ex situ* P Kα and Kβ X-ray emission spectroscopy (XES) couple together to understand the degradation of Ni_2P and show the effects of electrolyte and air on Ni_2P nanoparticles. Upon exposure to air, as-synthesized Ni_2P nanoparticles were studied via P Kα and Kβ XES in an inert atmosphere glovebox. Results showed that the phosphide species converted to phosphate with analysis of intermediates well fit by a simple two-component mixture. Electrochemical corrosion results demonstrate that Ni_2P nanoparticles corrode significantly before achieving a passive surface. The corrosion follows a phosphate-first pathway, followed by the rapid oxidation of excess Ni to form a passive surface. Approximately 80-90% of Ni dissolves before passivation is achieved. Future work with Ni_2P should consider the chemical structure of its surface in aqueous conditions and take advantage of its anodic passivation.

TABLE OF CONTENTS

LIST OF FIGURES

ACKNOWLEDGEMENTS

First, I would like to thank my mentor and advisor, Brandi. Thank you for your endless support, for adapting your advising style to help me succeed, meeting with me every other week to keep me focused and on track, and creating a welcoming lab environment for everyone in your group.

I would also like to thank the Cossairt lab for welcoming me with open arms as a summer student in 2019. I am grateful to my mentors in the lab, David, Ian, and Ding-Yuan, for guiding me, encouraging me to persevere, and teaching me how to be a scientist. Special thanks to our electrochemistry team, especially Emily N., for encouraging me to present at the ECS conference in Sweden. Thank you to the remaining residents of Australia as well, Florence, Hao, Michaela, Reed, and Pedro, for making each day in the office a good day. Thank you, Cecilia, for teaching me to be a responsible lab safety officer. I'm glad to see this vital role in good hands with Emily M.-S. and Ezra.

I would be remiss if I did not thank my mentees Abraham, Raiyan, Tracee, and Peter. Thank you for your patience as I learned the ropes of good mentorship and for your hard work advancing the projects we worked on together.

I want to express my gratitude to my favorite X-ray spectroscopists. First, Jerry, thank you for being a second mentor to me throughout my PhD journey. Anthony, Diwash, Helen, Jared, and Sam, I appreciate your collaboration and support while working alongside me on my XES and XAS experiments. Additionally, I would like to thank Zach and Lisa at easyXAFS LLC for

welcoming us into their offices and assisting me in conducting some of the most impactful experiments of my career.

I also want to express my gratitude to my collaborators and lab mates at the University of Hawaii, especially Godwin, for welcoming me into your lab and giving me the opportunity to mentor Tracee and Peter while conducting exploratory synthesis research. My summer in your lab will always be a cherished memory.

Thank you to the scientists at the Molecular Analysis Facility, especially Samantha, Ellen, and Scott, for enabling my research with world-class tools like XRD, XPS, TEM, and SEM.

I am also thankful for the Clean Energy Institute. CEI helped me meet great friends, learn about advancements in the clean energy field, and build many valuable connections. Thank you, Danica and Madelynne, for helping me become the best educator I could be and encouraging me to pursue my passions during my fellowship. Thank you, Jacob and Miguel, for working alongside me and for your support during the many educational activities we coordinated and led together.

I would like to recognize my mentors who have helped me get to where I am today. Michael, thank you for taking me under your wing during my freshman year. Nicholas, I appreciate your patience and guidance while teaching me about working with boron nitride. Prof. Wilson, thank you for welcoming me into your lab and encouraging me to pursue independent research for a semester. Prof. Martí, I am grateful for your inspiration and for the support you have provided to Puerto Rican and Latino students and scientists. Carlos, thank you for pushing me to be a responsible and independent researcher. Kendahl, I appreciate your friendship and encouragement in joining the chemistry department at UW.

I extend my gratitude to the Liberty Science Center Partners in Science program for introducing me to chemistry research in high school, to Prof. Rodenburg for welcoming me into

your lab when I was just 16, and to Staci for being my first research mentor. I would not be where I am today without this introduction to research.

I also want to thank all my friends and mentors outside of work for always helping me re-focus on what is truly important in life. Thank you to Fr. Augustine, Fr. Dominic David, Fr. Chrysostom, and Daniel for your spiritual guidance. Thank you to Matt, Sarah, Mercie, Evan, Chandler, and Mackenzie for providing a place to escape the stresses of graduate school. I appreciate Chris, Andrew, Chukwudi, David, Liam, and Carlos for sharing significant moments in life together. Thank you, Knights, for modeling family life and hospitality, especially Steve, Max, Fernando, Joe, and Brian.

I am immensely grateful to my parents for your constant support and example. You both inspire me and set a model I will always strive to follow. I am proud to be your son.

Most importantly, I want to thank my darling wife, Sierra. You stood by me through all the highs and lows of the past five years. Thank you for your companionship, humor, love, kindness, and encouragement. Thank you for spending countless hours helping me revise my writing and for listening to my presentations about topics unfamiliar to you. Thank you for marrying me and for making me the happiest man in the world. I love you.

DEDICATION

To my wife.

Chapter 1. INTRODUCTION

Significant portions of the following have previously been published in collaboration with F. W. Eagle, D.-Y. Kuo, E. Nishiwaki, and B. M. Cossairt.[1,2]

Global emissions from the chemical and petrochemical industry totaled 1.33 Gt CO_2 globally in 2022, approximately 4% of total global energy system emissions and 15% of industrial emissions.[3] In addition, the chemical industry is the largest industrial consumer of energy since it uses half of its energy input (carbon-based fuels) as chemical feedstock for various high-temperature and high-pressure reactions. Of the emissions from the chemical industry, 45% were from ammonia production, 28% from methanol production, and 27% from the production of high-value chemicals (e.g., ethylene, propylene, benzene, and toluene). These statistics point to a significant need to reduce the use of petroleum-based feedstocks and thermal reactions to synthesize the chemicals needed to sustain modern life on Earth. Combining advancements in clean electricity with low carbon emission resources like H_2O, N_2, and biomass could provide an alternative to our current reality in the chemical industry.[4] The greatest impact of electrification will be seen by targeting high-polluting reactions like ammonia production, which currently relies on reacting N_2 with H_2 at high temperatures and high pressures in centralized large-scale facilities. Additionally, most H_2 used in these reactions is acquired from the steam reforming of natural gas, another process contributing significantly to the total emissions from ammonia production. There are, therefore, two avenues to minimize emissions from ammonia production: 1) to produce H_2 from water using renewable electricity to replace the steam reforming of natural gas or 2) to produce ammonia from H_2O and N_2 outright using clean energy.

The global electrification of the chemical industry requires electrocatalysts that make these electrochemical reactions feasible and more energetically favorable. Today, most state-of-the-art catalysts use noble metals whose scarcity and high prices make them prohibitive for a global shift towards electrification.[5] Therefore, there is a need for earth-abundant catalyst alternatives. One particularly promising class of materials is transition metal phosphides (TMP), which were first predicted to catalyze the hydrogen evolution reaction (HER) effectively and were later realized as effective catalysts for various reactions.[6–12] Throughout this introductory chapter, we will introduce the chemistry of transition metal phosphides, including 1) the surface chemistry of TMP nanoparticles, 2) catalysis on TMPs, and 3) challenges with the corrosion of TMPs.

1.1 Overview of Transition Metal Phosphide Surface Chemistry

The history of metal phosphides dates back to the 1700s with the synthesis of Zn_3P_2 by Andreas Marggraf, followed later that century by Bertrand Pelletier's synthesis of 20 more metal phosphides from the pure metals and white phosphorus.[13] Applications of these metal phosphides, however, came much later. Among the metal phosphides are both metallic phases like Ni_2P, Cu_3P, and Ir_2P and semiconducting phases like Zn_3P_2, GaP, and InP.[14] This electronic structure is, in part, what dictates the ultimate utility of these materials. Since the development of III-V semiconductors for electronic applications in the 1950s,[15] the importance of metal phosphides in materials science and engineering has grown. This development has continued to this day, with the new dimension of physical scaling playing a prominent role.

For nanoscale metal phosphides, it is not only the electronic structure of the core that controls function but also the structure and composition of the nanomaterial surface. The covalency of metal phosphide lattices (arising from the relatively low electronegativity of P)[16] and their ease of oxidation [arising from the ease of accessing the P(V) oxidation state][14] make the

surface even more important for this class of materials relative to others. The facet termination (M versus P) and the degree of nonstoichiometry are the primary factors that establish surface chemistry in binary metal phosphide nanocrystals (Figure 1.1). Nanocrystals can range from stoichiometric, bearing the expected numbers of anions and cations needed to perfectly balance charge (i.e., 1:1 In:P for InP or 3:2 Zn:P for Zn_3P_2), to excessively nonstoichiometric, as can be the case for semiconductor nanocrystals like InP, which may be prepared with nearly a monolayer of excess cations.

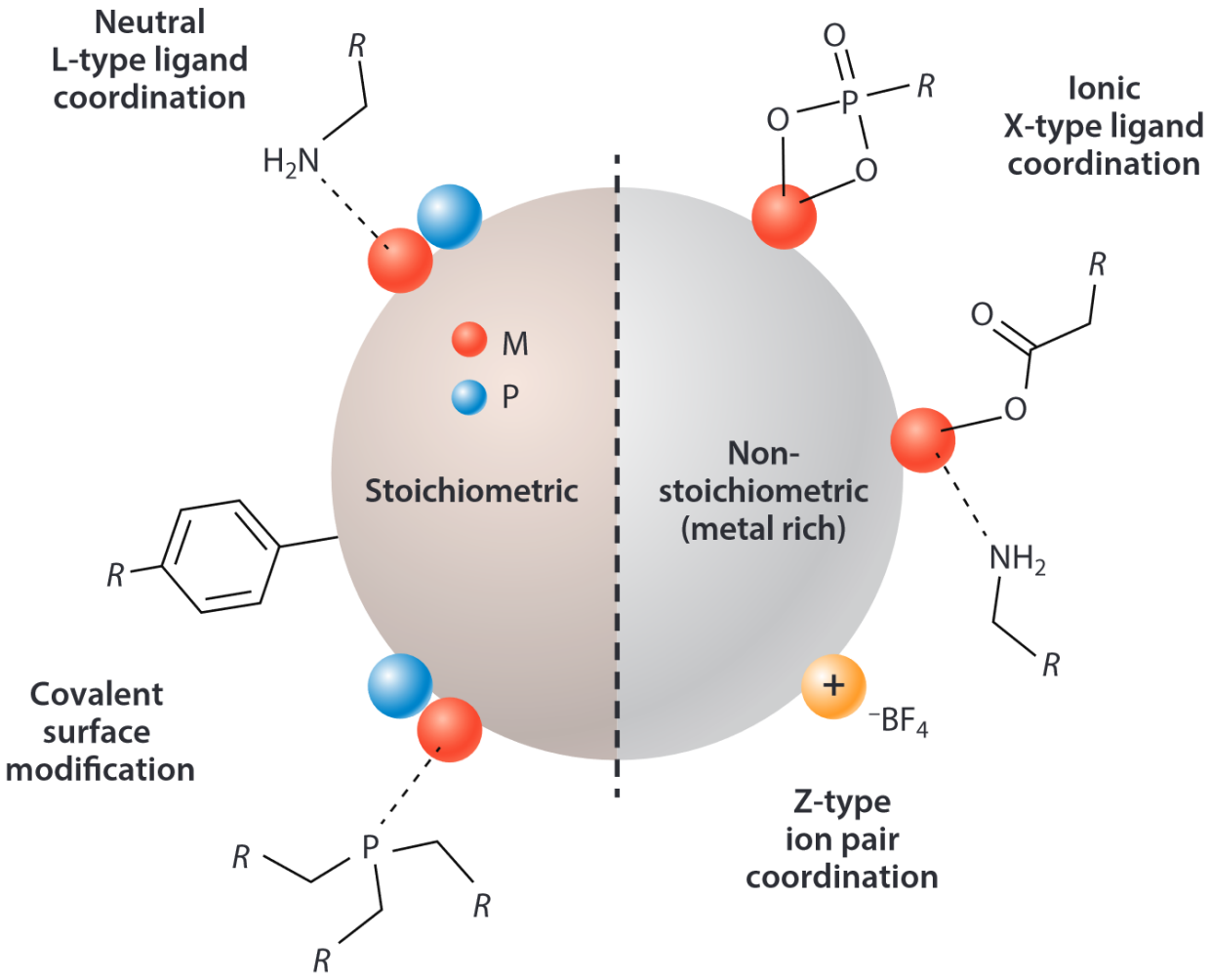

Figure 1.1. Representative surface chemistry of stoichiometric (left) and nonstoichiometric (right) metal phosphide nanocrystals illustrating neutral L-type ligand coordination, Z-type ion pair coordination, ionic X-type ligand coordination, and covalent surface modification.

The binding of ligands to all types of nanocrystal surfaces can be systematically described using an adapted version of the covalent bond classification method.[17–19] Using this formalism, neutral L-type Lewis bases like trioctylphosphine (TOP) and primary amines are the predominant type of surface termination in the case of stoichiometric nanocrystals. In the case of nonstoichiometric, metal-rich nanocrystals, anionic X-type ligands are an important contributor to the surface chemistry due to the need for charge balance. Interestingly, excess metal cations,

together with their X-type ligands, can be displaced from nanocrystal surfaces as Z-type metal-ligand complexes.[20,21] Such metal-ligand complexes can also be added to nanocrystal surfaces and exchanged for preexisting surface complexes.[22–24] Surface lability can lead to changes in nanocrystal stoichiometry during purification and manipulation. Variability in nanocrystal composition and its evolution as a function of reaction conditions have been most well studied for II-VI nanocrystals but are becoming a primary focus for metal phosphide nanocrystals as their properties are optimized for technological applications.

TMP nanocrystals have been widely explored as catalysts for various reactions, including hydrodesulfurization (HDS),[25,26] HER,[27–33] the oxygen evolution reaction (OER),[11,34,35] and hydrogenation.[36] Additionally, they are interesting for their magnetic properties,[37–39] their ability to serve as cocatalysts in photocatalytic hydrogen evolution,[40–42] and their applications in battery technologies.[43,44] While transition metal oxides and chalcogenides have been well known as catalysts in industry for over a century, phosphides have, by comparison, received less attention until more recently. Part of the reason for this recent attention is the unique way in which phosphorus modulates the activity of the transition metals themselves. In 2005, Liu & Rodriguez[6] predicted that the (001) plane of Ni_2P should be a suitable HER and HDS catalyst based on binding energetics because of a synergistic ensemble effect between Ni and P. Phosphorus moderates the binding of H-atoms to the Ni_2P surface so that they neither bind too strongly nor too weakly. Since then, others have explored surfaces on TMPs that are ideal for various forms of catalysis, such as deoxygenation reactions and the OER,[45–47] and additional surfaces that are HER active.[29,47,48] Taking TMPs to the nanometer length scale, as with most catalytic materials, allows for increased surface area, access to nonthermodynamic phases with distinct reactivity, and the ability to chemically design and tailor active sites and nanocrystal morphologies through surface chemistry.

In this section, we outline what is known about the surface chemistry of this unique class of materials, both in as-synthesized samples and through postsynthetic modification, with the aim of altering activity and stability.

1.1.1 *Transition Metal Phosphides: As Synthesized*

Some of the earliest colloidal syntheses of TMP nanocrystals were demonstrated by Brock and coworkers[37,49,50] modeling reactions after the more well-developed syntheses of semiconducting main group metal phosphides like InP. In this approach, $P(SiMe_3)_3$ was used as the primary phosphorus source, with trioctylphosphine oxide (TOPO) acting as both a weakly coordinating solvent and a secondary phosphorus source. Dodecylamine, myristic acid, and hexylphosphonic acid served as ligands to stabilize and solubilize the resulting FeP, MnP, and CoP nanocrystals. They concluded that ligands must bind neither too strongly nor too weakly to get the desired nanoparticle size and structure. TOPO does not bind strongly enough and leads to aggregation, whereas hexylphosphonic acid binds too strongly and leads to small, amorphous particles when used in high concentrations; dodecylamine and myristic acid successfully acted to moderate nucleation and growth.

In the years following, the use of TOPO as a P source and/or a coordinating solvent continued; however, many researchers saw advantages when moving to its reduced form, TOP, due to its more favorable release of PH_3 at elevated temperatures, improving reactivity toward phosphidation.[25,38,51–53] TOP has been demonstrated to decompose on metal surfaces at quite mild temperatures (~150°C) and has been implicated in carbon contamination of metal and metal phosphide materials.[54] Similar to hexylphosphonic acid, TOP can bind metal phosphide nanocrystals strongly and inhibit growth despite its dual function as a source of phosphide. Interestingly, oleylamine has been shown to give rise to metal-rich metal phosphides in syntheses

that use TOP as a P source by acting as a reducing agent and by competing with TOP at the nanocrystal surface, reducing the effective P concentration at the nanocrystal growth front.[55] Long-chain amines have continued to be ubiquitous capping ligands for TMP nanocrystals, with oleylamine being a dominant synthetic choice.[7,11,26–28,30,39,42,52,53,56–58] Other common capping ligands include alkylphosphonic acids (which can also serve as the P source)[49,59] and carboxylates, as mentioned above.[25,28,35,49,53,56,60,61]

Ligands have been shown to control the shape and size of TMP nanocrystals, consistent with what is seen for the more widely explored metal (e.g., Au, Ag, Cu, etc.) nanocrystal family. For example, nanorods of various TMPs were formed by Hyeon and coworkers[52] using a syringe pump to controllably deliver metal-TOP complexes into different solvent mixtures. Delivering a Mn-TOP complex solution into TOPO resulted in MnP nanorods; however, switching TOPO for octyl ether and oleylamine led to spherical MnO nanoparticles. Mixtures of Co_2P nanorods and spherical particles resulted from the use of Co-TOP and Co-oleylamine complexes in octyl ether and oleylamine, but switching to hexadecylamine resulted in purely nanorod-shaped particles with a higher aspect ratio.[52] An Fe-TOP complex solution added to octyl ether and oleylamine made Fe_2P nanorods,[39] while adding the complex to TOPO resulted in FeP nanorods, indicating that the more reducing conditions created by the amine solvent were able to promote the formation of iron in reduced oxidation states [e.g., Fe(II) and Fe(I)].[52] The authors hypothesized that more strongly binding ligands (e.g., TOP) were bound to the particles perpendicular to the growth plane, while more weakly binding ligands (e.g., oleylamine) were on the growth plane, allowing the anisotropic growth of the nanorods with the continuous injection of precursors (Figure 1.2a). These syntheses show the importance of the choice of surfactants for the phase, shape, and size of TMP colloidal nanoparticles, among other factors, such as temperature and speed of injection.

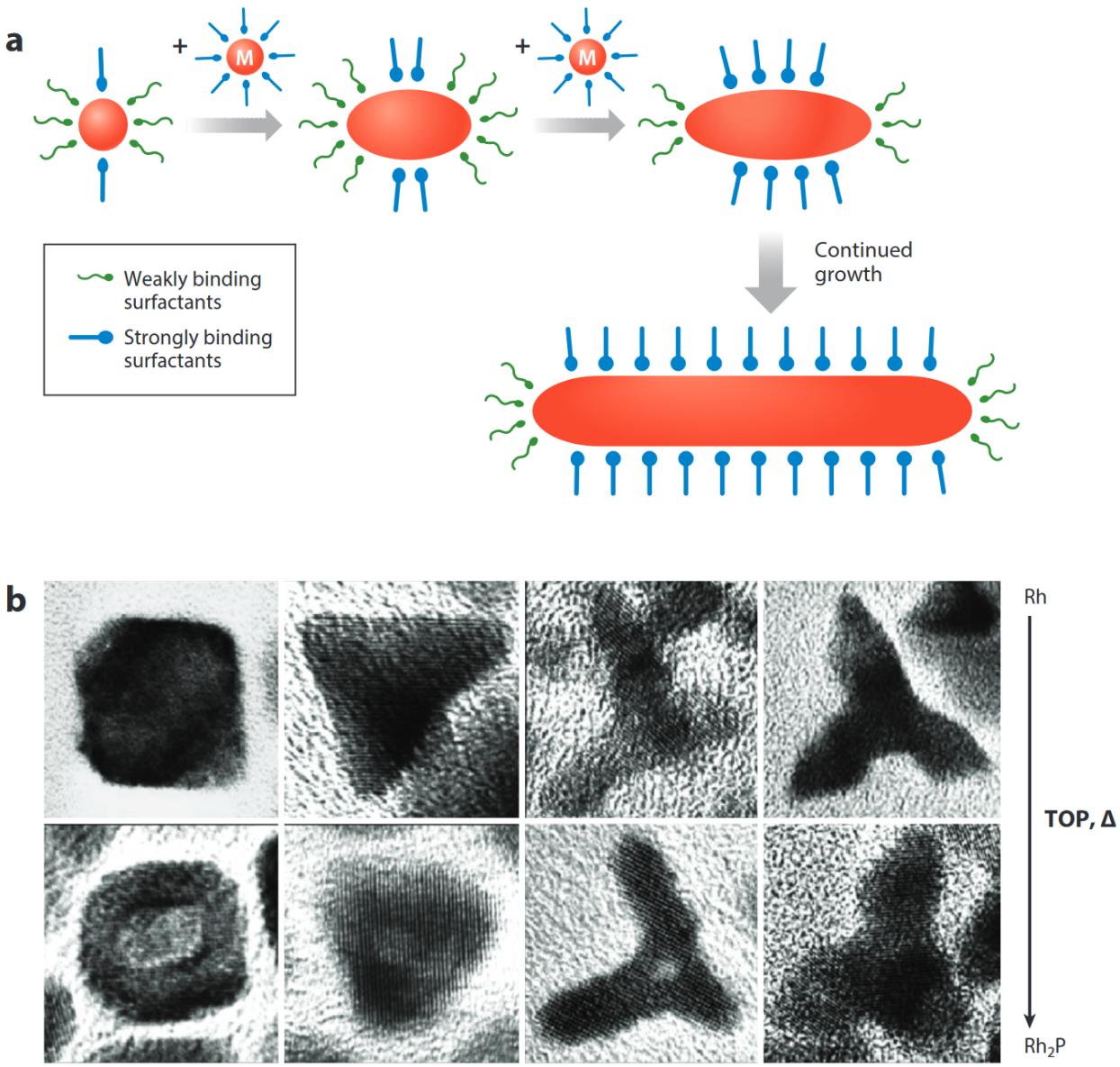

Figure 1.2. (a) The growth of transition metal phosphide nanorods based on the relative positions of strongly and weakly binding surfactants. Panel adapted with permission from Reference 52; copyright 2005 American Chemical Society. (b) Transmission electron microscopy images showing retention of the morphology of Rh nanoparticles upon thermally driven phosphidation using trioctylphosphine (TOP) to give Rh_2P. Panel adapted with permission from Reference 53; copyright 2008 American Chemical Society.

Research groups led by Chiang[56] and Schaak[62] independently found that varying the surfactants could lead to hollow TMP nanoparticles, especially when metal nanoparticle

intermediates were implicated. Oleylamine-capped Ni nanoparticles were treated with TOP to form hollow Ni_2P nanoparticles; oleylamine acted as a barrier for P diffusion into the particles, and Ni diffused out of the nanocrystal core via the Kirkendall mechanism.[60,63] Replacing oleylamine for hexadecylamine also resulted in hollow nanoparticles; however, using oleic acid led to Ni_2P nanorods, and the addition of TOPO resulted in solid spherical nanoparticles.[56]

Henkes & Schaak[53] also showed the importance of ligand coordination in the conversion of metal nanoparticles to metal phosphides while maintaining the original shape of the metal nanoparticle. Following literature procedures, they were able to make Rh nanoparticles of various shapes (cube, triangle, multipod with thin arms, and multipod with thick arms) (Figure 1.2b), followed by conversion to Rh_2P while maintaining the original morphology. The Rh nanoparticles were stabilized with poly(vinylpyrrolidone); however, they then did not dissolve in the TOP solution. Therefore, cosolvents were added to promote solubility in TOP. The choice of cosolvent was important for maintaining shape purity as some cosolvents resulted in differently shaped particles, e.g., oleic acid resulted in spherical Rh_2P nanoparticles. A mixture of oleylamine and TOP usually resulted in the best shape purity. The cosolvents and other stabilizing ligands made it so that the Rh and Rh_2P nanoparticles could kinetically stabilize different facets, promoting shape control relative to the thermodynamically preferred octahedron morphology.

1.1.2 *Transition Metal Phosphides: Postsynthetic Modification*

For catalytic applications, the conventional wisdom is that activity can be improved by increasing the number of active sites at the surface. For colloidal nanoparticles, that is usually accomplished by thermal annealing to remove the stabilizing ligands, thereby exposing active sites and preventing active site poisoning through competitive coordination.[7,28,30,35,64] A more systematic investigation of ligand effects on CoP nanoparticles for electrocatalytic hydrogen

evolution in aqueous media was conducted by Ung & Cossairt (Figure 1.3).[28] They found that common carboxylate and amine ligands did indeed impede catalysis; however, the effect was one of limited access to surface active sites and not poisoning. Carboxylates tended to bind more strongly to the nanoparticle surface, yielding high ligand densities. This led to a strong dependence of electrocatalytic activity on carboxylate chain length due to increased hydrophobicity. Additional evidence of the importance of the ligand environment is provided by Brutchey and coworkers,[58] who showed that carbene-ligated copper phosphide nanocrystals were more active for HER than as-synthesized oleylamine-ligated particles because the carbene surface ligands reduced unfavorable electrostatic interactions between the catalyst surface and the substrate. Ligand exchange and removal is also effective in other catalytic processes. For example, Fu and coworkers[42] exchanged the native TOP/oleylamine ligands for poly(vinylpyrrolidone) ligands to make Ni_2P nanoparticles soluble in aqueous media for the photocatalytic evolution of hydrogen. Similarly, Brock and coworkers[25] exchanged TOP/TOPO ligands with mercaptoundecanoic acid to improve HDS activity on Ni_2P nanocrystals. Both ligand-exchanged nanocrystals and those washed with $CHCl_3$ remained stable under reducing conditions and had improved HDS activity compared with as-synthesized Ni_2P. The wash with $CHCl_3$ doubled the surface area of the nanoparticles, while the ligand-exchanged particles had similar surface areas as the as-synthesized particles. Of special note is that the as-synthesized nanoparticles outperformed bulk Ni_2P and had six times the surface area, even with ligands still fully attached.[25] A later report by Brock and coworkers[26] removed ligands entirely through calcination to improve HDS catalytic activity and incorporated the nanoparticles into a silica network to prevent sintering.

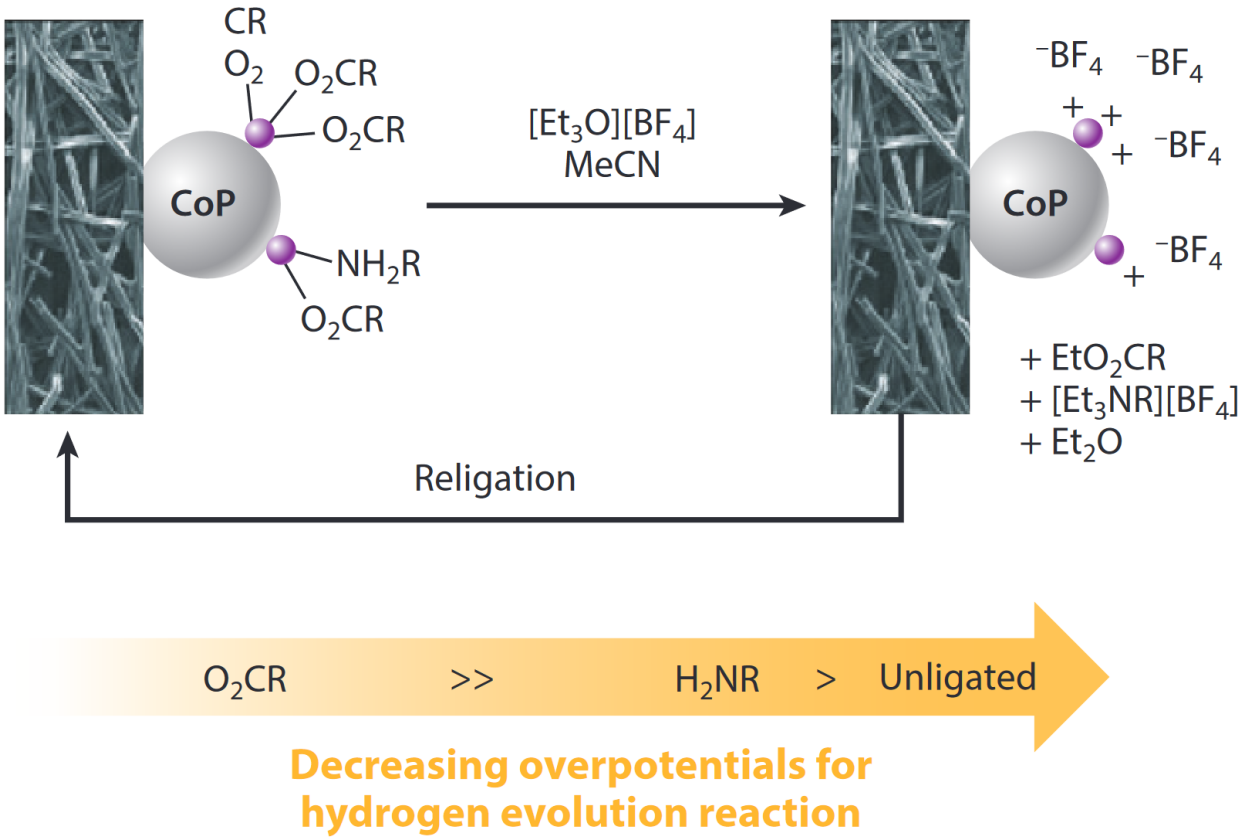

Figure 1.3. The removal of carboxylate and amine ligands from CoP nanocrystal surfaces following treatment with $[Et_3O][BF_4]$. Subsequent ligation studies demonstrate decreasing overpotentials for hydrogen evolution reaction in the order of $O_2CR \gg H_2NR >$ unligated. Abbreviations: Et, ethyl; Me, methyl. Figure adapted with permission from Reference 28; copyright 2019 American Chemical Society.

Modifying the surface to change what the substrate is exposed to can have a direct impact on catalytic and electrochemical activity and is the main reason that researchers remove or exchange surface ligands.[65] Other approaches to tune the environment in which the substrate interacts with the catalyst are creating three-dimensional structures of metal phosphide nanoparticles through gelation[61] and generating purposeful inorganic coatings[43]. Using the former, Brock and coworkers[61] exchanged TOP/oleylamine ligands for 11-mercaptoundecanoic acid, 4-fluorothiophenol, or 1-dodecanethiol. In the sol-gel route, particles were oxidized so that P–O–P bonds linked Ni_2P nanoparticles; in a second method, Ni^{2+} was added to the colloidal suspension

of mercaptoundecanoic acid–capped Ni_2P nanoparticles and bound to the pendant carboxylate tails. The preparation of gels generated a more easily usable material with the same surface area advantages found through nanoscaling. In another example, Sanchez and coworkers[43] decomposed surface ligands on 25-nm Ni_2P nanoparticles at 400°C to create a C-coating to make negative electrodes for lithium-ion batteries. This coating enabled the diffusion of Li^+ and good conductivity while preventing oxidation of the nanoparticle surface.

To better understand the thermodynamics and stoichiometry of hydrogen binding on metal phosphide surfaces, Mayer and coworkers[57] soaked CoP in an H_2 atmosphere and used this H_2-treated CoP to hydrogenate alkynes and phenoxy radicals. They were able to determine the quantity of hydrogen on the CoP surface by quantifying the yields of the hydrogenated products. Furthermore, an approximate range of bond dissociation free energies for the CoP–H intermediate could be determined by studying a series of well-defined H-atom donors and acceptors. Another attempt to better understand catalysis at metal phosphide surfaces was made by Zhang et al.,[66] who formed nanocrystalline Co_2P rods as seeds for the growth of a metal phosphide shell (Figure 1.4). This core-shell approach to metal phosphide synthesis enabled the formation of controlled multimetal phosphide nanorods with a consistent shape and size. Moreover, the Co_2P orthorhombic crystal structure could be retained upon annealing. Therefore, they were able to determine the impact of composition on the OER without the interference of many other factors. They saw that bimetallic phosphides outperformed Co_2P alone, with cobalt iron phosphide leading the pack in terms of OER activity.

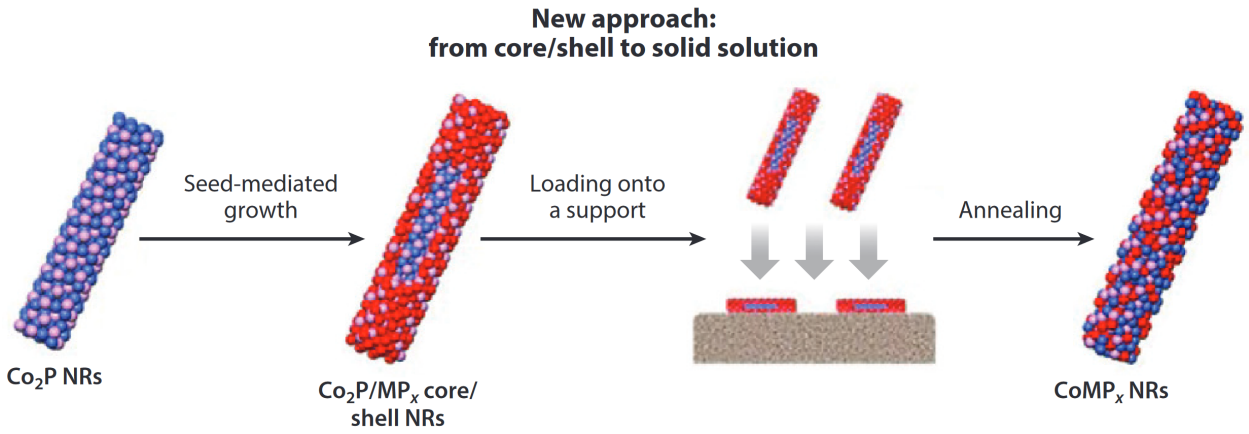

Figure 1.4. The programmable synthesis of multimetallic phosphide 1D nanorods (NRs) mediated by core/shell nanostructure formation. Figure adapted with permission from Reference 66; copyright 2020 American Chemical Society.

1.2 Catalysis on Transition Metal Phosphides: The Role of Hydrogen Adsorption Site Diversity

Hydrogen production via clean technologies such as water electrolysis and its use in the synthesis of value-added chemicals (e.g., ammonia production) plays a critical role in the pursuit of decarbonization.[67,68] This realization requires effective Earth-abundant catalysts that facilitate making and breaking H–H and H─X bonds. TMPs, such as nickel phosphide, cobalt phosphide, and molybdenum phosphide, have been historically used as hydroprocessing catalysts in the petroleum industry, enabling critical hydrodenitrogenation (HDN) and HDS reactions.[69–77] Over the past two decades, TMPs have been attracting extensive attention for applications in energy conversion,[78,79] because of their exceptional activity toward HER.[7,29,80,81]

In this section, we discuss the structural complexity of TMPs and the complexity's impact on the formation of adsorbed H (H_{ad}) and catalysis. In light of this, we discuss whether a single value of HBE is sufficient to describe TMP activity trends. Lastly, we propose that the presence

of diverse adsorption sites on TMP surfaces can be leveraged to design selective and efficient hydrogenation and electrochemical reduction reactions beyond HER.

1.2.1 *HBE Theory and the Role of H_{ad}*

The Sabatier principle dictates that the hydrogen binding of an ideal HER catalyst should be neither too strong nor too weak.[82] This empirical trend has led to the optimization of HBE as a primary design principle for HER catalysts. Beyond metal surfaces, this concept of finding an optimal HBE has been extended to the development of phosphide[80] and chalcogenide-based[83] catalysts.

The rationale for using the HBE to describe HER activity originates from its mechanism. As one of the simplest electrochemical reactions, extensive effort has been made toward understanding the mechanism of HER and its reverse reaction HOR, especially on Pt.[84,85]

- Volmer step $H^+ + e^- \rightleftharpoons H_{ad}$
- Tafel step $H_{ad} + H_{ad} \rightleftharpoons H_2$
- Heyrovsky step $H_{ad} + H^+ + e^- \rightleftharpoons H_2$

These three steps highlight the importance of H_{ad} as a key intermediate.[86] Within this framework, the HBE has been used as a quantity to rationalize activity trends for HER, where an effective catalyst surface should bind H neither too weakly, disfavoring adsorption (i.e., Volmer step), nor too strongly, hindering desorption (i.e., Tafel and Heyrovsky steps). The resulting relationship between the intrinsic activity of HER and HBE is known as the volcano plot.[87]

So far, HBE is believed to be the sole descriptor for HER in acidic media.[86] HBE theory has also been extended to explain pH-dependent HER activity on Pt and other noble metals.[88] However, the validity of using HBE in electrolytes other than aqueous acids is still disputed. It has

been shown that HBE theory cannot fully explain HER activity in alkaline media. This discrepancy has been attributed to the mechanistic difference in HER, where the H_{ad} is formed from the dissociation of water rather than from hydronium in alkaline media. This implies that water dissociation could be a rate-limiting step, and thus, the OH adsorption energy on the catalyst is thought to be crucial for HER in alkaline media.[89] In addition, the influence of interfacial electrical fields on the structure of water may be responsible for the slow kinetics of HER on Pt(111) in alkaline media, despite the fact that its HBE is comparable to the HBE in acid.[90] More discussion on this topic can be found in previous reviews.[86,91] Despite the ongoing debate, HBE is still the primary descriptor for rationalizing HER activity trends.

1.2.2 *H Adsorption Site Diversity Arises from Structural Complexity*

The structural complexity of TMP surfaces introduces several H adsorption sites with varying HBEs. The various stoichiometries and structures of TMPs range from metal-rich (e.g., Ni_3P),[92] equal amounts of metal and phosphorus (e.g., CoP),[93] to P-rich (e.g., NiP_3),[94] which are made possible by the highly covalent nature of metal–P bonds.[95] In addition, the crystal structures themselves vary significantly, often with multiple distinct metal and/or P sites within a unit cell.[96] These complex structures make analysis of TMP materials difficult and result in a large range of potential surfaces with a distribution of adsorption sites for substrates in catalysis. Figure 1.5 demonstrates the diversity of compositions, surfaces, and adsorption sites in the Ni–P system. Here, we see that at least three different binding motifs are available on a single surface of Ni_2P, which is also only one stoichiometry of Ni–P among a variety of different structures. This contrasts with transition metals whose structures have a tendency to be either body-centered cubic (BCC), hexagonal close-packed (HCP), or face-centered cubic (FCC) with predominantly low-index surfaces that are much simpler than those found on TMPs. These simpler surfaces typically have

single adsorption sites that dominate activity, allowing for structure-activity relationships to be readily drawn. Despite the diversity in H adsorption sites, a single value of HBE has been frequently used to rationalize the HER activity trend on TMPs.[80] Below, we list two reasons why we need to be cautious when applying HBE theory to understand TMP activity trends.

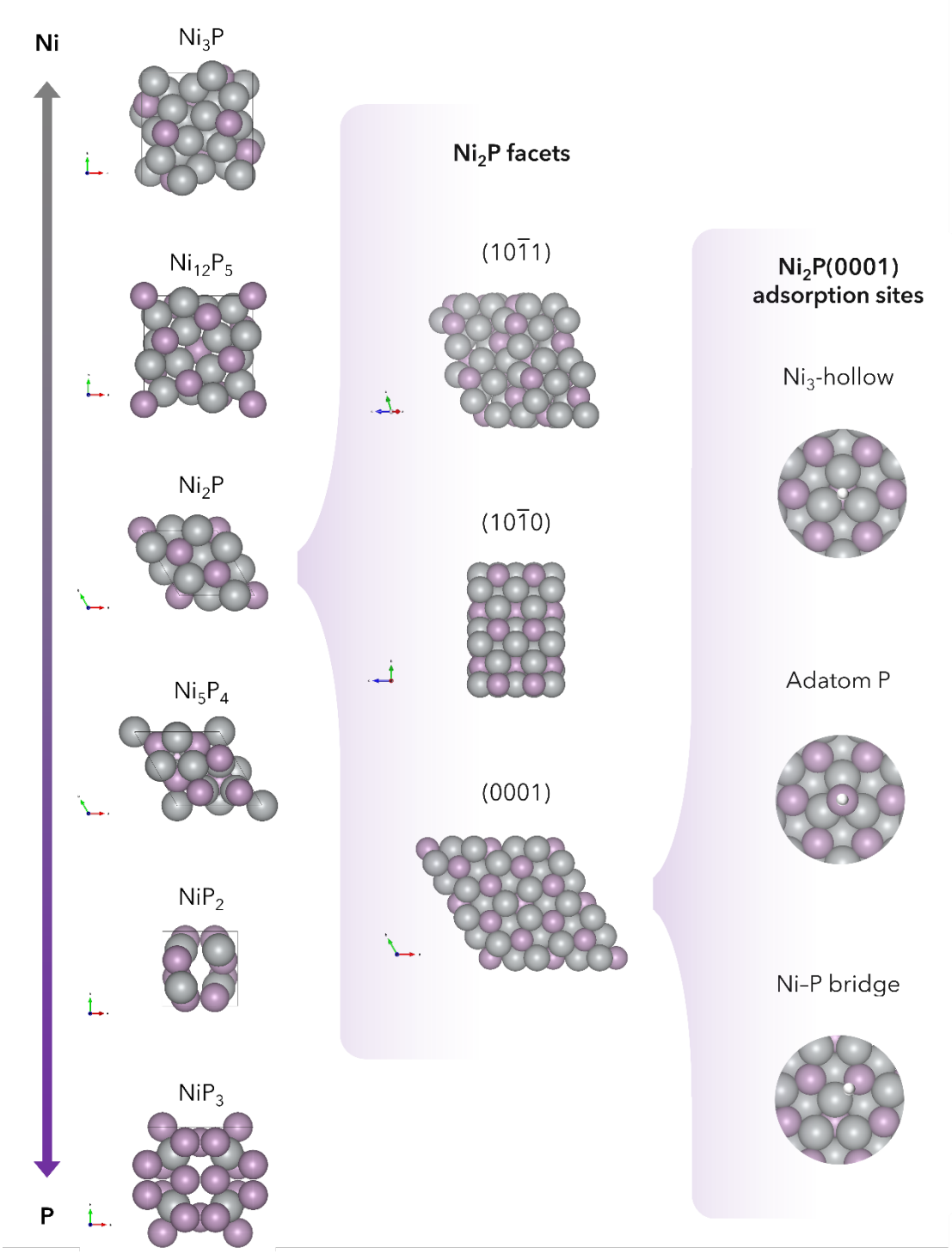

Figure 1.5. Complex structure of TMPs: the case of nickel phosphide. (Left panel) Structures of nickel phosphides with various Ni/P stoichiometries. (Middle panel) Representative low-index facets of Ni_2P. (Right panel) Representative H adsorption sites on the 0001 facet of Ni_2P.

1.2.2.1 Surface Site Heterogeneity

A key difference between metals and TMPs is in the heterogeneity of the individual surface sites. Li et al. showed that a metal surface such as Pt(111) only has a few types of adsorption sites that have similar computed HBEs.[97] This finding suggests that a single value of HBE can represent (or approximate) the formation energy of all H_{ad}, including the active intermediates in catalysis. In contrast, TMP surfaces have a more diverse array of H adsorption sites (metal–metal bridge sites, metal hollow sites, P atoms, etc.).[6,48,92,93,97] Therefore, unlike on metal surfaces, HER on TMPs usually involves H_{ad} with two distinct HBEs. For example, Liu et al. demonstrated that hydrogen is first adsorbed at the Ni_3-hollow site (HBE = −0.54 eV) and then is adsorbed at the Ni–P bridge site (HBE = 0.09 eV). Their computational result suggested that the incorporation of P weakens the adsorption energy of a second hydrogen and favors the desorption of an H_2 molecule on $Ni_2P(0001)$.[6] Similarly, Hansen et al. found that the favorable pathway of HER on multiple facets of Ni_2P involves a second H_{ad} with a weaker HBE.[48] Different stoichiometries of TMPs also have differing dominant H adsorption sites; e.g., Ni_3P mainly adsorbs H via P-sites while Ni_2P adsorbs H mainly on Ni_3-hollow sites. This demonstrates that determining the active site(s) for HER for a specific TMP is nontrivial and, overall, suggests that the energetics of HER on TMP surfaces cannot be described by a single value of HBE, in contrast to metal surfaces.[6,92]

1.2.2.2 Inconsistency in Computed HBEs

First-principles calculation has been the primary method to estimate the HBE and energetics of intermediates in the HER.[87,98] Briefly, the HBE at a specific adsorption site on a given surface (often the most stable facet) is calculated, and the value is used to represent the energy of the H_{ad} intermediate on the catalyst. However, it is not straightforward to access a single HBE on TMP surfaces that is representative for catalysis due to the structural complexity. For example, the

dominant facet of Ni_2P nanoparticles is size-dependent. Papawassiliou et al. found that (0001) surfaces dominate on Ni_2P ultrasmall nanoparticles (4 nm in diameter), but $(10\bar{1}0)$ surfaces dominate with larger nanoparticles (12 nm in diameter).[99] Even on the same facet (i.e., $Ni_2P(0001)$), there are multiple possible surface terminations (e.g., Ni_3P_2 and Ni_3P terminations).[99,100] In Figure 1.6, we summarize the computed HBE on $Ni_2P(0001)$[6,48,80,95,100–103] and $CoP(101)$[80,104–106] surfaces from reported values in the literature. The calculated HBE at the Ni_3 hollow site on the $Ni_2P(0001)$ surface ranges from 0.137 eV to −0.543 eV. The calculated HBE at the Co-bridge site ranges from 0.38 eV to −0.43 eV. This huge range may be due to the choice of functional, the slab structure, and the surface coverage used in the computation. Because of the large spread of the HBE, justification of the choice of computation slab structure and validation from experimental results are recommended. In addition, the variety of different adsorption sites on TMP surfaces can further complicate the determination of HBE. Figure 1.6 shows that Ni–P bridge sites and P top sites both show some distribution in HBE such that there is overlap among these different adsorption sites. Consequently, an approach embracing the often-overlooked complexity of TMP surfaces and the diversity of surface adsorption sites can help us to better understand key active sites and energies for the adsorption of H. Such approaches would be comparable to those used for high-entropy alloys, where a distribution of adsorption energy at various sites is commonly used to understand the surface active sites.[107]

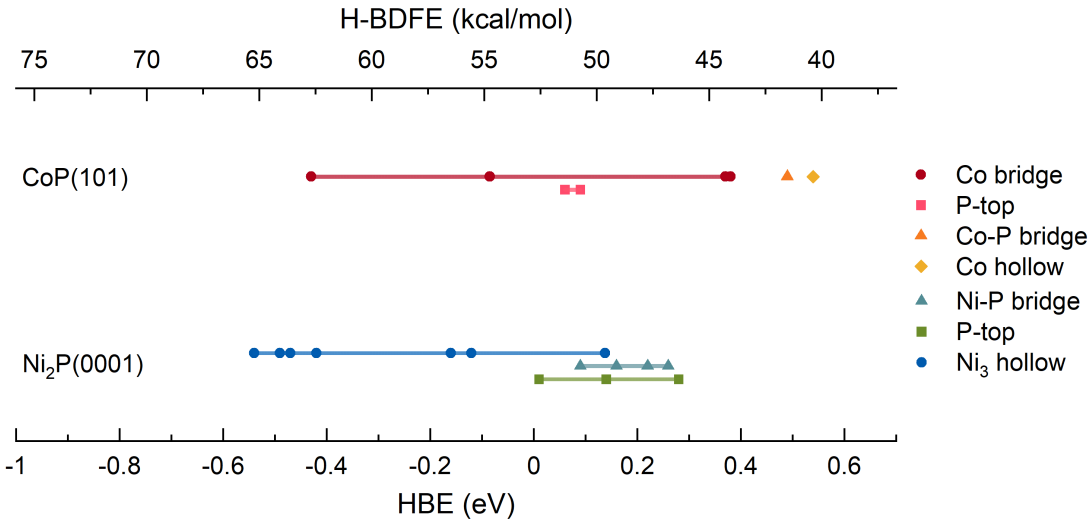

Figure 1.6. H binding energy on $Ni_2P(0001)$ and CoP(101) from DFT calculations.

1.2.3 *The Role of Adsorption Site Diversity in Reactions Beyond HER*

The diversity of H adsorption sites also affects the dissociation of H_2 on TMP surfaces, which is a key step in HOR and hydrogenation reactions. On a metal surface, the dissociation of H_2 is more likely to proceed via homolytic bond cleavage due to identical (or near identical) adsorption sites for the H atom. On a TMP surface, H_2 is more likely to be cleaved heterolytically, similar to what is observed on other binary materials.[108–110] A surface consisting of metal and phosphorus induces inhomogeneous surface electron density[111,112] that may favor heterolytic cleavage by polarizing the H_2 bond. A recent computational study further shows that the H_2 dissociation mechanism may be termination-dependent on metal-doped Ni_2P.[113] Regardless of the mechanism, the adsorption site diversity results in the presence of H_{ad} with various HBEs on TMP surfaces after exposure to H_2.

Strongly bound H on TMP surfaces can serve as a source of H in hydrogenation reactions (Figure 1.7). Wei et al. observed that Ni_2P can facilitate the hydrogenation of nitrate to ammonia under mild temperature conditions. Interestingly, they also found that Ni_2P annealed under H_2 can

still hydrogenate nitrate in an inert atmosphere, implying the presence of H_{ad} on the surface of Ni_2P after annealing.[114] This empirical evidence suggests that H_2 can dissociate and form H_{ad} on the Ni_2P surface, and the H-BDFE of H–Ni_2P is stronger than the H-BDFE of an H_2 molecule (52.8 kcal/mol).[115] We believe that this H is adsorbed at a stronger binding site (e.g., the Ni_3 hollow site). This hydrogen can be transferred to a substrate with a higher H-BDFE such as nitrate. The redox potential of nitrate to ammonia at pH 0 is 0.88 V vs. SHE, which suggests a strong tendency to accept H_{ad} from Ni_2P. The regenerated empty site can participate in H_2 dissociation, turning over the catalytic reaction. In contrast, without the H acceptor (e.g., nitrate), the stronger binding site will be "poisoned" by $H_{ad,}$ and the reaction will not turn over. While this strongly bound H_{ad} can be expelled by applying an oxidative potential, the surface of TMP could be oxidized under such conditions, fundamentally changing the nature of the catalyst.[104]

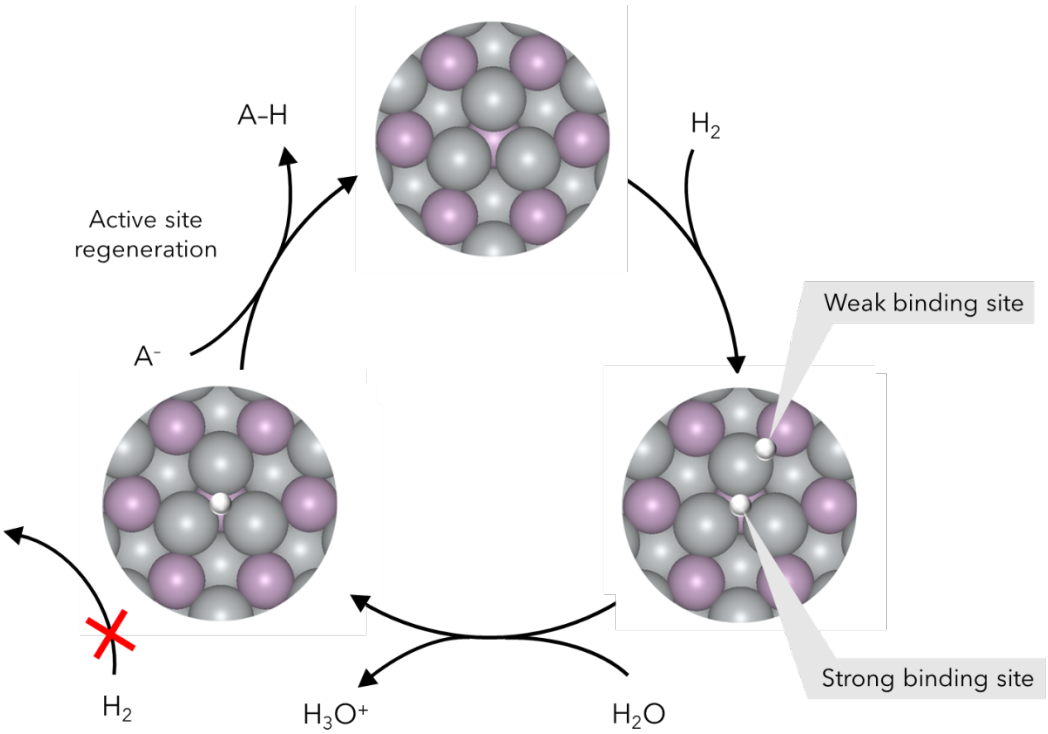

Figure 1.7. Schematic that shows the role of strongly bound H in hydrogenation reactions vs HOR. Gray, purple, and white spheres represent Ni, P, and H atoms, respectively. A^- is a strong H acceptor.

In addition to H adsorption, the presence of a diversity of surface sites on TMPs allows the adsorption of different intermediates. These surfaces can create local active site motifs that allow groups of adsorbed intermediates to readily react with each other. Understanding the impacts of these motifs is crucial for more complex chemical reactions whose mechanisms cannot solely be described by the binding of H. Specifically, we believe that the diversity in adsorption sites on TMPs is advantageous for 1) complex thermal,[36,114,116–124] 2) electrochemical (e.g., CO_2 reduction[9,10,125] and nitrate reduction,[126,127] and 3) photochemical reactions.[128–130] For example, in CO_2 reduction, a common theory is that a binary surface creates local hydride sources for facile CO_2 hydrogenation (Figure 1.8).[131] This concept has been used to rationalize electrochemical CO_2 reduction on nickel and iron phosphides, where experimental studies have shown that the

application of low overpotentials can mitigate HER and direct selectivity toward multicarbon and oxygenated products.[9,10] DFT studies on Ni_2P have claimed that, compared to bare metal surfaces, the binary surface of a TMP can facilitate CO_2 hydrogenation by promoting migration of H_{ad} to Ni sites with weaker HBEs. Additionally, the presence of a multitude of H adsorption sites results in exergonic C–C coupling via $*H_2CO$ self-condensation, which drives selectivity toward multicarbon and oxygenated products instead of H_2.[131] The complexity of TMP surfaces is a tuning knob for CO_2 reduction reaction selectivity that distinguishes them from monometallic materials. We note that other factors, such as the Ni:P ratio and the identity of the catalyst support, can also play a role in reaction kinetics, mainly by modulating surface energetics.[128,132] However, we believe that the role of local active site motifs present on TMP surfaces is crucial when considering their (electro)catalytic behavior.

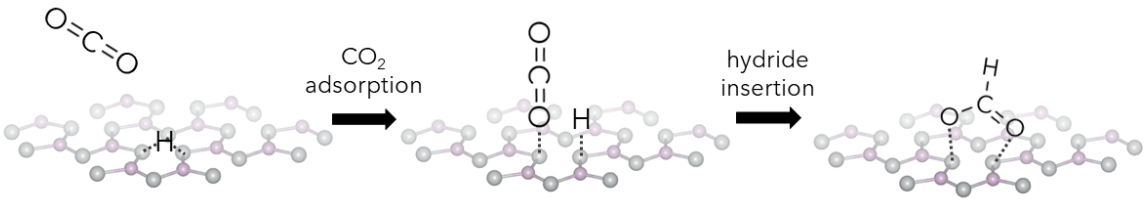

Figure 1.8. Schematic that demonstrates the proposed mechanism of CO_2 hydrogenation on Ni_2P. Gray and purple spheres represent Ni and P atoms, respectively.

1.3 Corrosion of Transition Metal Phosphides

Phosphorus has long been used as an additive for enhancing corrosion resistance in metals, especially for amorphous or nanocrystalline alloys.[133–136] Comparing Ni to an amorphous Ni-P alloy in 0.1 M H_2SO_4 through anodic polarization, Carbajal and White found Ni corroded faster

than Ni-P alloy near their corrosion potentials.[133] However, when they continued to apply more anodic potentials, the corrosion rate in Ni peaked and decreased due to the passivation of the surface. In contrast, the corrosion rate for Ni-P continually increased. In O_2-saturated neutral pH electrolyte solutions, Ni-P behaved similarly to how it behaved in N_2-saturated 0.1 M H_2SO_4, but in O_2-saturated 1 M NaOH, Ni-P was passivated. Also, although Ni-P did not demonstrate passivation behavior in sulfuric acid, the amorphous Ni-P alloy had better pitting resistance than Ni in the same electrolyte solution. Additionally, Carbajal and White found that Ni atoms dissolved more quickly than P during the anodic polarization of Ni-P, leaving behind a P-enriched surface layer. Later studies found that after polarizing for 1 h at -0.1 V and 0.1 V vs. SCE in 0.1 M Na_2SO_4, the surface of a Ni-P alloy consisted of a 1 nm thick nickel phosphate layer and a 1 nm P enrichment layer (up to 50 atom %) beneath the phosphate layer.[135,136] The authors attributed the corrosion resistance of Ni-P alloys to the phosphate and P-enriched layers, which protected the bulk of the alloy against corrosion. These results paint a positive picture of the corrosion resistance of Ni-P alloys without or with minimal polarization; however, results appear grim for the corrosion resistance of Ni-P alloys during the anodic polarization required for the electrocatalysis of various oxidation reactions such as OER.

Kucernak and Sundaram compared a Ni-P alloy to crystalline Ni_2P and $Ni_{12}P_5$, and they found that crystalline nickel phosphides had significantly lower corrosion rates during anodic polarization and achieved passivation in 0.5 M H_2SO_4.[137] Therefore, crystalline metal phosphides may have better stability than metal-phosphorus alloys. Parra-Puerto et al. conducted similar research with a range of phosphides in 0.1 M KOH and 0.1 M $HClO_4$ at 0.8 V and 1.2 V vs. RHE, which are catalytically relevant potentials for the oxygen reduction reaction (ORR) and OER/transient polarization in fuel cells, respectively.[12] They found that MoP, CrP, WP, and Ni_2P

did not corrode significantly in alkaline conditions. Similarly, Co_2P did not corrode significantly at 0.8 V in alkaline conditions; however, it did corrode significantly at 1.2 V. In acidic conditions, Co_2P and Ni_2P both corroded significantly at 0.8 V and 1.2 V. The P to metal ratio increase was linked to the greater stability of WP, CrP, and MoP compared to Co_2P and Ni_2P. Interestingly, Co_2P also performed the best out of the series of phosphides at catalyzing HER and ORR in both acidic and alkaline conditions. Additionally, Co_2P was second only to Ni_2P at catalyzing OER. So, although Co_2P experienced the most corrosion in both acidic and alkaline conditions, it was also arguably the best catalyst out of the group. When analyzing CoP nanoparticles for water splitting, Ha et al. found that P leached out of the CoP at potentials above 0.4 V vs. RHE in both acidic and alkaline conditions.[104] They proposed that the P leaching caused HER activity to decrease due to the essential role of P in catalyzing HER on metal phosphides. Ha et al. also found that higher P-to-Co ratios led to better HER activity. However, the trend of higher P-to-metal ratios improving corrosion resistance is not absolute. Laursen et al. predicted that NiP_2 would have a lower enthalpy of formation than other nickel phosphides with lower P-to-Ni ratios, replacing stronger Ni-P bonds for weaker P-P bonds and making NiP_2 less stable.[92] Laursen et al. see this prediction as additional support for their observation that NiP_2 is less corrosion resistant in air than other nickel phosphides.

Most of the corrosion studies of TMPs have been conducted in acidic and alkaline conditions. However, there is potential for TMPs to be more stable in neutral conditions and for neutral conditions to enable new kinds of catalysis.[138] An excellent example is nitrate reduction on Ni_2P electrocatalysts.[8] Nitrate reduction performs better in neutral conditions because neutral pH reduces competing HER activity. Despite the potential of neutral conditions, there is a lack of precedent for their use in electrocatalysis, and further studies on electrocatalytic mechanisms and structure-activity relationships in these conditions are necessary. Additionally, as catalysis studies

in neutral pH grow in popularity, it is important to expand our knowledge of TMP stability in neutral media.

1.4 Conclusions and Outlook

Transition metal phosphides are widely considered earth-abundant alternatives to precious metals in catalysis. Their nanoparticle form is particularly attractive owing to their high surface area to volume ratio, which maximizes the number of available active sites on a per mass basis. Surface chemistry is both the current and future frontier of metal phosphide nanoparticle design. Surface ligands not only control structure and morphology but are also essential in controlling nanocrystal function by altering activity for inner-sphere chemical transformations and controlling extra-particle solvent and substrate interactions, which are important in charge transfer and catalysis. The surface chemistry of metal phosphide nanocrystals is initially dictated by the synthesis conditions, with surfactants and coordinating ions present that both kinetically trap the growing particles and passivate undercoordinated surface atoms. The as-prepared surface chemistry of metal phosphide nanocrystals has been predominantly explored using a combination of infrared, nuclear magnetic resonance, and various X-ray spectroscopic methods in addition to theory. However, the complexity of the as-prepared surface is often difficult to fully capture using these methods. Postsynthetic modification of the native metal phosphide surface can be used not only as a strategy to probe the native surface but also to augment the function of the nanocrystals.

Interestingly, the surface chemistry of TMP surfaces, in which catalytic activity is dominated by inner-sphere reactivity, has been explored far less than that of II-P and III-P semiconductor materials. Surfaces are most commonly described as nearly stoichiometric, with passivation and stabilization largely met by L-type ligand coordination. X-ray photoelectron spectroscopy analysis and density functional theory calculations show metal-phosphorus bonding

that is quite covalent in nature, with electron density equally distributed across the metal and phosphorus atoms. The complex bonding nature of metal-phosphorus in TMPs leads to diverse adsorption sites on their surfaces. This array of adsorption sites with a wide range in HBE creates a more energetically favorable pathway for HER on TMP surfaces. Most importantly, the diversity of sites on TMP surfaces is crucial in understanding mechanisms of more complex reactions involving hydrogen, such as CO_2 or nitrate reduction. The number of literature reports that attribute catalytic activity to phosphorus, creating local active site motifs that simultaneously adsorb different intermediates, indicates the applicability of these concepts across a wide variety of TMP catalysts. Experimentally, we posit that the controlled synthetic design of TMP-based materials with desirable active site motifs can move us closer to designing and understanding the origin of activity for various electrocatalytic reactions. We believe that such efforts to develop a systematic understanding of the role that a diversity of sites plays in complex reactions is critical for advancing catalyst design.

Also key to advancing TMP catalyst design is a thorough understanding of their stability in catalytically relevant conditions. While oxidation must be an issue for these materials, systematic studies to control and understand its impacts are lacking. Knowledge of the corrosion of TMPs can improve theoretical studies of TMPs as electrocatalysts, inform conditions to avoid, or inspire approaches for protecting TMP surfaces from corrosion. Strategies to covalently modify these surfaces to tune their reactivity by changing their electronic structure and/or interfacial properties using radical or related atom transfer chemistries will likely be a productive line of inquiry. Much remains to be discovered regarding nanocrystal surfaces, and this is true for metal phosphides as much as for any other material. The interplay of bond covalency and elevated reactivity observed at metal phosphide surfaces creates a challenge but also a unique opportunity

to build new functionality. Only when we can make and manipulate metal phosphide surfaces with atom-level specificity will we be able to take full advantage of this exciting class of materials.

This thesis will expand our knowledge of TMP surface chemistry through the study of nickel phosphide nanoparticle corrosion. Nickel phosphide nanoparticles, a key member of the TMP materials family, have effectively catalyzed various reactions across a range of conditions but were also predicted to be unstable upwards of 0 V vs. RHE at any pH in aqueous conditions.[100] We will show how Ni_2P nanoparticles oxidize in air through P Kα and Kβ X-ray emission spectroscopy (Chapter 2). Additionally, we will demonstrate the electrochemical corrosion of Ni_2P nanoparticles in acidic, neutral, and basic pH conditions through potentiodynamic anodic polarization (Chapter 3). We will then use *operando* Ni K-edge X-ray absorption spectroscopy to elucidate the corrosion mechanism of Ni_2P nanoparticles in a neutral pH electrolyte solution (Chapter 3). Finally, we will give insight into the methods developed to enable these and future studies on the corrosion of nanomaterials (Chapter 4).

1.5 References

(1) Eagle, F. W.; Rivera-Maldonado, R. A.; Cossairt, B. M. Surface Chemistry of Metal Phosphide Nanocrystals. *Annu. Rev. Mater. Res.* **2021**, *51* (1), 541–564. https://doi.org/10.1146/annurev-matsci-080819-011036.

(2) Kuo, D.-Y.; Nishiwaki, E.; Rivera-Maldonado, R. A.; Cossairt, B. M. The Role of Hydrogen Adsorption Site Diversity in Catalysis on Transition-Metal Phosphide Surfaces. *ACS Catal.* **2022**, 287–295. https://doi.org/10.1021/acscatal.2c04936.

(3) *Tracking Clean Energy Progress 2023 – Analysis - IEA*. https://www.iea.org/reports/tracking-clean-energy-progress-2023 (accessed 2024-10-23).

(4) Schiffer, Z. J.; Manthiram, K. Electrification and Decarbonization of the Chemical Industry. *Joule* **2017**, *1* (1), 10–14. https://doi.org/10.1016/j.joule.2017.07.008.

(5) Seh, Z. W.; Kibsgaard, J.; Dickens, C. F.; Chorkendorff, I.; Nørskov, J. K.; Jaramillo, T. F. Combining Theory and Experiment in Electrocatalysis: Insights into Materials Design. *Science* **2017**, *355* (6321), eaad4998. https://doi.org/10.1126/science.aad4998.

(6) Liu, P.; Rodriguez, J. A. Catalysts for Hydrogen Evolution from the [NiFe] Hydrogenase to the Ni2P(001) Surface: The Importance of Ensemble Effect. *J. Am. Chem. Soc.* **2005**, *127* (42), 14871–14878. https://doi.org/10.1021/ja0540019.

(7) Popczun, E. J.; McKone, J. R.; Read, C. G.; Biacchi, A. J.; Wiltrout, A. M.; Lewis, N. S.; Schaak, R. E. Nanostructured Nickel Phosphide as an Electrocatalyst for the Hydrogen Evolution Reaction. *J. Am. Chem. Soc.* **2013**, *135* (25), 9267–9270. https://doi.org/10.1021/ja403440e.

(8) Nishiwaki, E.; Rice, P. S.; Kuo, D.-Y.; Dou, F. Y.; Pyka, A.; Reid, B.; Nguyen, H. A.; Stuve, E. M.; Raugei, S.; Cossairt, B. M. Ni2P Active Site Ensembles Tune Electrocatalytic Nitrate Reduction Selectivity. *Chem. Commun.* **2024**, *60* (54), 6941–6944. https://doi.org/10.1039/D4CC01834F.

(9) Calvinho, K. U. D.; Alherz, A. W.; Yap, K. M. K.; Laursen, A. B.; Hwang, S.; Bare, Z. J. L.; Clifford, Z.; Musgrave, C. B.; Dismukes, G. C. Surface Hydrides on Fe2P Electrocatalyst Reduce CO2 at Low Overpotential: Steering Selectivity to Ethylene Glycol. *J. Am. Chem. Soc.* **2021**, *143* (50), 21275–21285. https://doi.org/10.1021/jacs.1c03428.

(10) D. Calvinho, K. U.; B. Laursen, A.; K. Yap, K. M.; A. Goetjen, T.; Hwang, S.; Murali, N.; Mejia-Sosa, B.; Lubarski, A.; M. Teeluck, K.; S. Hall, E.; Garfunkel, E.; Greenblatt, M.; Charles Dismukes, G. Selective CO 2 Reduction to C 3 and C 4 Oxyhydrocarbons on Nickel Phosphides at Overpotentials as Low as 10 mV. *Energy Environ. Sci.* **2018**, *11* (9), 2550–2559. https://doi.org/10.1039/C8EE00936H.

(11) Man, H.-W.; Tsang, C.-S.; Li, M. M.-J.; Mo, J.; Huang, B.; Lee, L. Y. S.; Leung, Y.; Wong, K.-Y.; Tsang, S. C. E. Tailored Transition Metal-Doped Nickel Phosphide Nanoparticles for the Electrochemical Oxygen Evolution Reaction (OER). *Chem. Commun.* **2018**, *54* (62), 8630–8633. https://doi.org/10.1039/C8CC03870H.

(12) Parra-Puerto, A.; Ng, K. L.; Fahy, K.; Goode, A. E.; Ryan, M. P.; Kucernak, A. Supported Transition Metal Phosphides: Activity Survey for HER, ORR, OER, and Corrosion Resistance in Acid and Alkaline Electrolytes. *ACS Catal.* **2019**, 11515–11529. https://doi.org/10.1021/acscatal.9b03359.

(13) Carenco, S.; Portehault, D.; Boissière, C.; Mézailles, N.; Sanchez, C. Nanoscaled Metal Borides and Phosphides: Recent Developments and Perspectives. *Chem. Rev.* **2013**, *113* (10), 7981–8065. https://doi.org/10.1021/cr400020d.

(14) Greenwood, N. N.; Earnshaw, A. *Chemistry of the Elements*; Elsevier, 2012.

(15) Welker, H. J. Discovery and Development of III-V Compounds. *IEEE Trans. Electron Devices* **1976**, *23* (7), 664–674. https://doi.org/10.1109/T-ED.1976.18471.

(16) Heath, J. R. Covalency in Semiconductor Quantum Dots. *Chem. Soc. Rev.* **1998**, *27* (1), 65–71. https://doi.org/10.1039/A827065Z.

(17) Green, M. L. H. A New Approach to the Formal Classification of Covalent Compounds of the Elements. *J. Organomet. Chem.* **1995**, *500* (1), 127–148. https://doi.org/10.1016/0022-328X(95)00508-N.

(18) Green, M. L. H.; Parkin, G. Application of the Covalent Bond Classification Method for the Teaching of Inorganic Chemistry. *J. Chem. Educ.* **2014**, *91* (6), 807–816. https://doi.org/10.1021/ed400504f.

(19) Owen, J. The Coordination Chemistry of Nanocrystal Surfaces. *Science* **2015**, *347* (6222), 615–616. https://doi.org/10.1126/science.1259924.

(20) Anderson, N. C.; Hendricks, M. P.; Choi, J. J.; Owen, J. S. Ligand Exchange and the Stoichiometry of Metal Chalcogenide Nanocrystals: Spectroscopic Observation of Facile Metal-Carboxylate Displacement and Binding. *J. Am. Chem. Soc.* **2013**, *135* (49), 18536–18548. https://doi.org/10.1021/ja4086758.

(21) C. Gary, D.; Petrone, A.; Li, X.; M. Cossairt, B. Investigating the Role of Amine in InP Nanocrystal Synthesis: Destabilizing Cluster Intermediates by Z-Type Ligand Displacement. *Chem. Commun.* **2017**, *53* (1), 161–164. https://doi.org/10.1039/C6CC07952K.
(22) Stein, J. L.; Mader, E. A.; Cossairt, B. M. Luminescent InP Quantum Dots with Tunable Emission by Post-Synthetic Modification with Lewis Acids. *J. Phys. Chem. Lett.* **2016**, *7* (7), 1315–1320. https://doi.org/10.1021/acs.jpclett.6b00177.
(23) Hughes, K. E.; Stein, J. L.; Friedfeld, M. R.; Cossairt, B. M.; Gamelin, D. R. Effects of Surface Chemistry on the Photophysics of Colloidal InP Nanocrystals. *ACS Nano* **2019**, *13* (12), 14198–14207. https://doi.org/10.1021/acsnano.9b07027.
(24) Kirkwood, N.; Monchen, J. O. V.; Crisp, R. W.; Grimaldi, G.; Bergstein, H. A. C.; du Fossé, I.; van der Stam, W.; Infante, I.; Houtepen, A. J. Finding and Fixing Traps in II–VI and III–V Colloidal Quantum Dots: The Importance of Z-Type Ligand Passivation. *J. Am. Chem. Soc.* **2018**, *140* (46), 15712–15723. https://doi.org/10.1021/jacs.8b07783.
(25) Senevirathne, K.; Burns, A. W.; Bussell, M. E.; Brock, S. L. Synthesis and Characterization of Discrete Nickel Phosphide Nanoparticles: Effect of Surface Ligation Chemistry on Catalytic Hydrodesulfurization of Thiophene. *Adv. Funct. Mater.* **2007**, *17* (18), 3933–3939. https://doi.org/10.1002/adfm.200700758.
(26) Layan Savithra, G. H.; Muthuswamy, E.; Bowker, R. H.; Carrillo, B. A.; Bussell, M. E.; Brock, S. L. Rational Design of Nickel Phosphide Hydrodesulfurization Catalysts: Controlling Particle Size and Preventing Sintering. *Chem. Mater.* **2013**, *25* (6), 825–833. https://doi.org/10.1021/cm302680j.
(27) Mundy, M. E.; Ung, D.; Lai, N. L.; Jahrman, E. P.; Seidler, G. T.; Cossairt, B. M. Aminophosphines as Versatile Precursors for the Synthesis of Metal Phosphide Nanocrystals. *Chem. Mater.* **2018**, *30* (15), 5373–5379. https://doi.org/10.1021/acs.chemmater.8b02206.
(28) Ung, D.; Cossairt, B. M. Effect of Surface Ligands on CoP for the Hydrogen Evolution Reaction. *ACS Appl. Energy Mater.* **2019**, *2* (3), 1642–1645. https://doi.org/10.1021/acsaem.9b00240.
(29) Shi, Y.; Zhang, B. Recent Advances in Transition Metal Phosphide Nanomaterials: Synthesis and Applications in Hydrogen Evolution Reaction. *Chem. Soc. Rev.* **2016**, *45* (6), 1529–1541. https://doi.org/10.1039/C5CS00434A.
(30) Pan, Y.; Liu, Y.; Zhao, J.; Yang, K.; Liang, J.; Liu, D.; Hu, W.; Liu, D.; Liu, Y.; Liu, C. Monodispersed Nickel Phosphide Nanocrystals with Different Phases: Synthesis, Characterization and Electrocatalytic Properties for Hydrogen Evolution. *J. Mater. Chem. A* **2015**, *3* (4), 1656–1665. https://doi.org/10.1039/C4TA04867A.
(31) Liu, J.; Wang, Z.; David, J.; Llorca, J.; Li, J.; Yu, X.; Shavel, A.; Arbiol, J.; Meyns, M.; Cabot, A. Colloidal Ni2−xCoxP Nanocrystals for the Hydrogen Evolution Reaction. *J. Mater. Chem. A* **2018**, *6* (24), 11453–11462. https://doi.org/10.1039/C8TA03485K.
(32) Landers, A. T.; Fields, M.; Torelli, D. A.; Xiao, J.; Hellstern, T. R.; Francis, S. A.; Tsai, C.; Kibsgaard, J.; Lewis, N. S.; Chan, K.; Hahn, C.; Jaramillo, T. F. The Predominance of Hydrogen Evolution on Transition Metal Sulfides and Phosphides under CO2 Reduction Conditions: An Experimental and Theoretical Study. *ACS Energy Lett.* **2018**, *3* (6), 1450–1457. https://doi.org/10.1021/acsenergylett.8b00237.

(33) Greeley, J.; Jaramillo, T. F.; Bonde, J.; Chorkendorff, I.; Nørskov, J. K. Computational High-Throughput Screening of Electrocatalytic Materials for Hydrogen Evolution. *Nat. Mater.* **2006**, *5* (11), 909–913. https://doi.org/10.1038/nmat1752.

(34) Li, Z.; Dou, X.; Zhao, Y.; Wu, C. Enhanced Oxygen Evolution Reaction of Metallic Nickel Phosphide Nanosheets by Surface Modification. *Inorg. Chem. Front.* **2016**, *3* (8), 1021–1027. https://doi.org/10.1039/C6QI00078A.

(35) Stern, L.-A.; Feng, L.; Song, F.; Hu, X. Ni 2 P as a Janus Catalyst for Water Splitting: The Oxygen Evolution Activity of Ni 2 P Nanoparticles. *Energy Environ. Sci.* **2015**, *8* (8), 2347–2351. https://doi.org/10.1039/C5EE01155H.

(36) Mitsudome, T.; Sheng, M.; Nakata, A.; Yamasaki, J.; Mizugaki, T.; Jitsukawa, K. A Cobalt Phosphide Catalyst for the Hydrogenation of Nitriles. *Chem. Sci.* **2020**, *11* (26), 6682–6689. https://doi.org/10.1039/D0SC00247J.

(37) Brock, S. L.; Perera, S. C.; Stamm, K. L. Chemical Routes for Production of Transition-Metal Phosphides on the Nanoscale: Implications for Advanced Magnetic and Catalytic Materials. *Chem. – Eur. J.* **2004**, *10* (14), 3364–3371. https://doi.org/10.1002/chem.200305775.

(38) Chen, J.-H.; Tai, M.-F.; Chi, K.-M. Catalytic Synthesis, Characterization and Magnetic Properties of Iron Phosphide Nanowires. *J. Mater. Chem.* **2004**, *14* (3), 296–298. https://doi.org/10.1039/B311943B.

(39) Park, J.; Koo, B.; Hwang, Y.; Bae, C.; An, K.; Park, J.-G.; Park, H. M.; Hyeon, T. Novel Synthesis of Magnetic Fe2P Nanorods from Thermal Decomposition of Continuously Delivered Precursors Using a Syringe Pump. *Angew. Chem. Int. Ed.* **2004**, *43* (17), 2282–2285. https://doi.org/10.1002/anie.200353562.

(40) Roske, C. W.; Popczun, E. J.; Seger, B.; Read, C. G.; Pedersen, T.; Hansen, O.; Vesborg, P. C. K.; Brunschwig, B. S.; Schaak, R. E.; Chorkendorff, I.; Gray, H. B.; Lewis, N. S. Comparison of the Performance of CoP-Coated and Pt-Coated Radial Junction N+p-Silicon Microwire-Array Photocathodes for the Sunlight-Driven Reduction of Water to H2(g). *J. Phys. Chem. Lett.* **2015**, *6* (9), 1679–1683. https://doi.org/10.1021/acs.jpclett.5b00495.

(41) Callejas, J. F.; McEnaney, J. M.; Read, C. G.; Crompton, J. C.; Biacchi, A. J.; Popczun, E. J.; Gordon, T. R.; Lewis, N. S.; Schaak, R. E. Electrocatalytic and Photocatalytic Hydrogen Production from Acidic and Neutral-pH Aqueous Solutions Using Iron Phosphide Nanoparticles. *ACS Nano* **2014**, *8* (11), 11101–11107. https://doi.org/10.1021/nn5048553.

(42) Cao, S.; Chen, Y.; Wang, C.-J.; He, P.; Fu, W.-F. Highly Efficient Photocatalytic Hydrogen Evolution by Nickel Phosphide Nanoparticles from Aqueous Solution. *Chem. Commun.* **2014**, *50* (72), 10427–10429. https://doi.org/10.1039/C4CC05026F.

(43) Carenco, S.; Surcin, C.; Morcrette, M.; Larcher, D.; Mézailles, N.; Boissière, C.; Sanchez, C. Improving the Li-Electrochemical Properties of Monodisperse Ni2P Nanoparticles by Self-Generated Carbon Coating. *Chem. Mater.* **2012**, *24* (4), 688–697. https://doi.org/10.1021/cm203164a.

(44) Aso, K.; Hayashi, A.; Tatsumisago, M. Phase-Selective Synthesis of Nickel Phosphide in High-Boiling Solvent for All-Solid-State Lithium Secondary Batteries. *Inorg. Chem.* **2011**, *50* (21), 10820–10824. https://doi.org/10.1021/ic2013733.

(45) He, Y.; Laursen, S. The Surface and Catalytic Chemistry of the First Row Transition Metal Phosphides in Deoxygenation. *Catal. Sci. Technol.* **2018**, *8* (20), 5302–5314. https://doi.org/10.1039/C8CY01134F.

(46) He, Y.; Laursen, S. Trends in the Surface and Catalytic Chemistry of Transition-Metal Ceramics in the Deoxygenation of a Woody Biomass Pyrolysis Model Compound. *ACS Catal.* **2017**, *7* (5), 3169–3180. https://doi.org/10.1021/acscatal.6b02806.
(47) Scaranto, J.; Idriss, H. DFT Studies of Bulk and Surfaces of the Electrocatalyst Cobalt Phosphide CoP2. *Chem. Phys. Lett. X* **2019**, *2*, 100008. https://doi.org/10.1016/j.cpletx.2019.100008.
(48) Hansen, M. H.; Stern, L.-A.; Feng, L.; Rossmeisl, J.; Hu, X. Widely Available Active Sites on Ni2P for Electrochemical Hydrogen Evolution – Insights from First Principles Calculations. *Phys. Chem. Chem. Phys.* **2015**, *17* (16), 10823–10829. https://doi.org/10.1039/C5CP01065A.
(49) Perera, S. C.; Fodor, P. S.; Tsoi, G. M.; Wenger, L. E.; Brock, S. L. Application of De-Silylation Strategies to the Preparation of Transition Metal Pnictide Nanocrystals: The Case of FeP. *Chem. Mater.* **2003**, *15* (21), 4034–4038. https://doi.org/10.1021/cm034443o.
(50) Perera, S. C.; Tsoi, G.; Wenger, L. E.; Brock, S. L. Synthesis of MnP Nanocrystals by Treatment of Metal Carbonyl Complexes with Phosphines: A New, Versatile Route to Nanoscale Transition Metal Phosphides. *J. Am. Chem. Soc.* **2003**, *125* (46), 13960–13961. https://doi.org/10.1021/ja038037h.
(51) Qian, C.; Kim, F.; Ma, L.; Tsui, F.; Yang, P.; Liu, J. Solution-Phase Synthesis of Single-Crystalline Iron Phosphide Nanorods/Nanowires. *J. Am. Chem. Soc.* **2004**, *126* (4), 1195–1198. https://doi.org/10.1021/ja038401c.
(52) Park, J.; Koo, B.; Yoon, K. Y.; Hwang, Y.; Kang, M.; Park, J.-G.; Hyeon, T. Generalized Synthesis of Metal Phosphide Nanorods via Thermal Decomposition of Continuously Delivered Metal−Phosphine Complexes Using a Syringe Pump. *J. Am. Chem. Soc.* **2005**, *127* (23), 8433–8440. https://doi.org/10.1021/ja0427496.
(53) Henkes, A. E.; Schaak, R. E. Template-Assisted Synthesis of Shape-Controlled Rh2P Nanocrystals. *Inorg. Chem.* **2008**, *47* (2), 671–677. https://doi.org/10.1021/ic701783f.
(54) Carenco, S.; Liu, Z.; Salmeron, M. The Birth of Nickel Phosphide Catalysts: Monitoring Phosphorus Insertion into Nickel. *ChemCatChem* **2017**, *9* (12), 2318–2323. https://doi.org/10.1002/cctc.201601526.
(55) Muthuswamy, E.; Savithra, G. H. L.; Brock, S. L. Synthetic Levers Enabling Independent Control of Phase, Size, and Morphology in Nickel Phosphide Nanoparticles. *ACS Nano* **2011**, *5* (3), 2402–2411. https://doi.org/10.1021/nn1033357.
(56) Chiang, R.-K.; Chiang, R.-T. Formation of Hollow Ni2P Nanoparticles Based on the Nanoscale Kirkendall Effect. *Inorg. Chem.* **2007**, *46* (2), 369–371. https://doi.org/10.1021/ic061846s.
(57) Delley, M. F.; Wu, Z.; Mundy, M. E.; Ung, D.; Cossairt, B. M.; Wang, H.; Mayer, J. M. Hydrogen on Cobalt Phosphide. *J. Am. Chem. Soc.* **2019**, *141* (38), 15390–15402. https://doi.org/10.1021/jacs.9b07986.
(58) Tappan, B. A.; Chen, K.; Lu, H.; Sharada, S. M.; Brutchey, R. L. Synthesis and Electrocatalytic HER Studies of Carbene-Ligated Cu3–xP Nanocrystals. *ACS Appl. Mater. Interfaces* **2020**, *12* (14), 16394–16401. https://doi.org/10.1021/acsami.0c00025.
(59) Li, Y.; Malik, M. A.; O'Brien, P. Synthesis of Single-Crystalline CoP Nanowires by a One-Pot Metal−Organic Route. *J. Am. Chem. Soc.* **2005**, *127* (46), 16020–16021. https://doi.org/10.1021/ja055963i.
(60) Moreau, L. M.; Ha, D.-H.; Zhang, H.; Hovden, R.; Muller, D. A.; Robinson, R. D. Defining Crystalline/Amorphous Phases of Nanoparticles through X-Ray Absorption Spectroscopy

and X-Ray Diffraction: The Case of Nickel Phosphide. *Chem. Mater.* **2013**, *25* (12), 2394–2403. https://doi.org/10.1021/cm303490y.

(61) Hitihami-Mudiyanselage, A.; Senevirathne, K.; Brock, S. L. Bottom-Up Assembly of Ni2P Nanoparticles into Three-Dimensional Architectures: An Alternative Mechanism for Phosphide Gelation. *Chem. Mater.* **2014**, *26* (21), 6251–6256. https://doi.org/10.1021/cm5030958.

(62) Henkes, A. E.; Vasquez, Y.; Schaak, R. E. Converting Metals into Phosphides: A General Strategy for the Synthesis of Metal Phosphide Nanocrystals. *J. Am. Chem. Soc.* **2007**, *129* (7), 1896–1897. https://doi.org/10.1021/ja068502l.

(63) Ha, D.-H.; Moreau, L. M.; Bealing, C. R.; Zhang, H.; Hennig, R. G.; Robinson, R. D. The Structural Evolution and Diffusion during the Chemical Transformation from Cobalt to Cobalt Phosphide Nanoparticles. *J. Mater. Chem.* **2011**, *21* (31), 11498–11510. https://doi.org/10.1039/C1JM10337G.

(64) Callejas, J. F.; Read, C. G.; Roske, C. W.; Lewis, N. S.; Schaak, R. E. Synthesis, Characterization, and Properties of Metal Phosphide Catalysts for the Hydrogen-Evolution Reaction. *Chem. Mater.* **2016**, *28* (17), 6017–6044. https://doi.org/10.1021/acs.chemmater.6b02148.

(65) Ung, D.; Murphy, I. A.; Cossairt, B. M. Designing Nanoparticle Interfaces for Inner-Sphere Catalysis. *Dalton Trans.* **2020**, *49* (16), 4995–5005. https://doi.org/10.1039/D0DT00785D.

(66) Zhang, Y.; Li, N.; Zhang, Z.; Li, S.; Cui, M.; Ma, L.; Zhou, H.; Su, D.; Zhang, S. Programmable Synthesis of Multimetallic Phosphide Nanorods Mediated by Core/Shell Structure Formation and Conversion. *J. Am. Chem. Soc.* **2020**, *142* (18), 8490–8497. https://doi.org/10.1021/jacs.0c02584.

(67) Chu, S.; Cui, Y.; Liu, N. The Path towards Sustainable Energy. *Nat. Mater.* **2017**, *16* (1), 16–22. https://doi.org/10.1038/nmat4834.

(68) Staffell, I.; Scamman, D.; Abad, A. V.; Balcombe, P.; Dodds, P. E.; Ekins, P.; Shah, N.; Ward, K. R. The Role of Hydrogen and Fuel Cells in the Global Energy System. *Energy Environ. Sci.* **2019**, *12* (2), 463–491. https://doi.org/10.1039/C8EE01157E.

(69) Lu, M.; Wang, A.; Li, X.; Duan, X.; Teng, Y.; Wang, Y.; Song, C.; Hu, Y. Hydrodenitrogenation of Quinoline Catalyzed by MCM-41-Supported Nickel Phosphides. *Energy Fuels* **2007**, *21* (2), 554–560. https://doi.org/10.1021/ef060467g.

(70) Li, X.; Lu, M.; Wang, A.; Song, C.; Hu, Y. Promoting Effect of TiO2 on the Hydrodenitrogenation Performance of Nickel Phosphide. *J. Phys. Chem. C* **2008**, *112* (42), 16584–16592. https://doi.org/10.1021/jp803676v.

(71) Wagner, J. L.; Jones, E.; Sartbaeva, A.; Davis, S. A.; Torrente-Murciano, L.; Chuck, C. J.; Ting, V. P. Zeolite Y Supported Nickel Phosphide Catalysts for the Hydrodenitrogenation of Quinoline as a Proxy for Crude Bio-Oils from Hydrothermal Liquefaction of Microalgae. *Dalton Trans.* **2018**, *47* (4), 1189–1201. https://doi.org/10.1039/C7DT03318D.

(72) Bowker, R. H.; Ilic, B.; Carrillo, B. A.; Reynolds, M. A.; Murray, B. D.; Bussell, M. E. Carbazole Hydrodenitrogenation over Nickel Phosphide and Ni-Rich Bimetallic Phosphide Catalysts. *Appl. Catal. Gen.* **2014**, *482*, 221–230. https://doi.org/10.1016/j.apcata.2014.05.026.

(73) Oyama, S. T.; Lee, Y.-K. Mechanism of Hydrodenitrogenation on Phosphides and Sulfides. *J. Phys. Chem. B* **2005**, *109* (6), 2109–2119. https://doi.org/10.1021/jp049194l.

(74) Vidal, A. B.; Peña-Mena, J. L.; Hurtado-Aular, O.; Añez, R.; Sierraalta, A. Unraveling the Structure and Surface Chemistry of the Phosphosulfide Phase Formed on Ni2P under

Hydrodesulfurization Reaction Conditions: A DFT Study. *J. Phys. Chem. C* **2022**, *126* (33), 14187–14200. https://doi.org/10.1021/acs.jpcc.2c04700.
(75) Burns, A. W.; Gaudette, A. F.; Bussell, M. E. Hydrodesulfurization Properties of Cobalt–Nickel Phosphide Catalysts: Ni-Rich Materials Are Highly Active. *J. Catal.* **2008**, *260* (2), 262–269. https://doi.org/10.1016/j.jcat.2008.10.001.
(76) Burns, A. W.; Layman, K. A.; Bale, D. H.; Bussell, M. E. Understanding the Relationship between Composition and Hydrodesulfurization Properties for Cobalt Phosphide Catalysts. *Appl. Catal. Gen.* **2008**, *343* (1), 68–76. https://doi.org/10.1016/j.apcata.2008.03.022.
(77) Oyama, S. T.; Lee, Y.-K. The Active Site of Nickel Phosphide Catalysts for the Hydrodesulfurization of 4,6-DMDBT. *J. Catal.* **2008**, *258* (2), 393–400. https://doi.org/10.1016/j.jcat.2008.06.023.
(78) Pu, Z.; Liu, T.; Amiinu, I. S.; Cheng, R.; Wang, P.; Zhang, C.; Ji, P.; Hu, W.; Liu, J.; Mu, S. Transition-Metal Phosphides: Activity Origin, Energy-Related Electrocatalysis Applications, and Synthetic Strategies. *Adv. Funct. Mater.* **2020**, *30* (45), 2004009. https://doi.org/10.1002/adfm.202004009.
(79) Sun, M.; Liu, H.; Qu, J.; Li, J. Earth-Rich Transition Metal Phosphide for Energy Conversion and Storage. *Adv. Energy Mater.* **2016**, *6* (13), 1600087. https://doi.org/10.1002/aenm.201600087.
(80) Kibsgaard, J.; Tsai, C.; Chan, K.; Benck, J. D.; Nørskov, J. K.; Abild-Pedersen, F.; Jaramillo, T. F. Designing an Improved Transition Metal Phosphide Catalyst for Hydrogen Evolution Using Experimental and Theoretical Trends. *Energy Environ. Sci.* **2015**, *8* (10), 3022–3029. https://doi.org/10.1039/C5EE02179K.
(81) Weng, C.-C.; Ren, J.-T.; Yuan, Z.-Y. Transition Metal Phosphide-Based Materials for Efficient Electrochemical Hydrogen Evolution: A Critical Review. *ChemSusChem* **2020**, *13* (13), 3357–3375. https://doi.org/10.1002/cssc.202000416.
(82) Trasatti, S. Work Function, Electronegativity, and Electrochemical Behaviour of Metals: III. Electrolytic Hydrogen Evolution in Acid Solutions. *J. Electroanal. Chem. Interfacial Electrochem.* **1972**, *39* (1), 163–184. https://doi.org/10.1016/S0022-0728(72)80485-6.
(83) Xia, H.; Shi, Z.; Gong, C.; He, Y. Recent Strategies for Activating the Basal Planes of Transition Metal Dichalcogenides towards Hydrogen Production. *J. Mater. Chem. A* **2022**, *10* (37), 19067–19089. https://doi.org/10.1039/D2TA02458F.
(84) Kronberg, R.; Laasonen, K. Reconciling the Experimental and Computational Hydrogen Evolution Activities of Pt(111) through DFT-Based Constrained MD Simulations. *ACS Catal.* **2021**, *11* (13), 8062–8078. https://doi.org/10.1021/acscatal.1c00538.
(85) Skúlason, E.; Karlberg, G. S.; Rossmeisl, J.; Bligaard, T.; Greeley, J.; Jónsson, H.; Nørskov, J. K. Density Functional Theory Calculations for the Hydrogen Evolution Reaction in an Electrochemical Double Layer on the Pt(111) Electrode. *Phys. Chem. Chem. Phys.* **2007**, *9* (25), 3241–3250. https://doi.org/10.1039/B700099E.
(86) Dubouis, N.; Grimaud, A. The Hydrogen Evolution Reaction: From Material to Interfacial Descriptors. *Chem. Sci.* **2019**, *10* (40), 9165–9181. https://doi.org/10.1039/C9SC03831K.
(87) Nørskov, J. K.; Bligaard, T.; Logadottir, A.; Kitchin, J. R.; Chen, J. G.; Pandelov, S.; Stimming, U. Trends in the Exchange Current for Hydrogen Evolution. *J. Electrochem. Soc.* **2005**, *152* (3), J23. https://doi.org/10.1149/1.1856988.
(88) Sheng, W.; Zhuang, Z.; Gao, M.; Zheng, J.; Chen, J. G.; Yan, Y. Correlating Hydrogen Oxidation and Evolution Activity on Platinum at Different pH with Measured Hydrogen Binding Energy. *Nat. Commun.* **2015**, *6* (1), 5848. https://doi.org/10.1038/ncomms6848.

(89) McCrum, I. T.; Koper, M. T. M. The Role of Adsorbed Hydroxide in Hydrogen Evolution Reaction Kinetics on Modified Platinum. *Nat. Energy* **2020**, *5* (11), 891–899. https://doi.org/10.1038/s41560-020-00710-8.

(90) Ledezma-Yanez, I.; Wallace, W. D. Z.; Sebastián-Pascual, P.; Climent, V.; Feliu, J. M.; Koper, M. T. M. Interfacial Water Reorganization as a pH-Dependent Descriptor of the Hydrogen Evolution Rate on Platinum Electrodes. *Nat. Energy* **2017**, *2* (4), 1–7. https://doi.org/10.1038/nenergy.2017.31.

(91) Zheng, Y.; Jiao, Y.; Vasileff, A.; Qiao, S.-Z. The Hydrogen Evolution Reaction in Alkaline Solution: From Theory, Single Crystal Models, to Practical Electrocatalysts. *Angew. Chem. Int. Ed.* **2018**, *57* (26), 7568–7579. https://doi.org/10.1002/anie.201710556.

(92) Laursen, A. B.; Wexler, R. B.; Whitaker, M. J.; Izett, E. J.; Calvinho, K. U. D.; Hwang, S.; Rucker, R.; Wang, H.; Li, J.; Garfunkel, E.; Greenblatt, M.; Rappe, A. M.; Dismukes, G. C. Climbing the Volcano of Electrocatalytic Activity While Avoiding Catalyst Corrosion: Ni3P, a Hydrogen Evolution Electrocatalyst Stable in Both Acid and Alkali. *ACS Catal.* **2018**, *8* (5), 4408–4419. https://doi.org/10.1021/acscatal.7b04466.

(93) Hu, G.; Tang, Q.; Jiang, D. CoP for Hydrogen Evolution: Implications from Hydrogen Adsorption. *Phys. Chem. Chem. Phys.* **2016**, *18* (34), 23864–23871. https://doi.org/10.1039/C6CP04011J.

(94) Jeitschko, W.; Foecker, A. J.; Paschke, D.; Dewalsky, M. V.; Evers, Ch. B. H.; Künnen, B.; Lang, A.; Kotzyba, G.; Rodewald, U. Ch.; Möller, M. H. Crystal Structure and Properties of Some Filled and Unfilled Skutterudites: GdFe4P12, SmFe4P12, NdFe4As12, Eu0.54Co4Sb12, Fe0.5Ni0.5P3, CoP3, and NiP3. *Z. Für Anorg. Allg. Chem.* **2000**, *626* (5), 1112–1120. https://doi.org/10.1002/(SICI)1521-3749(200005)626:5<1112::AID-ZAAC1112>3.0.CO;2-E.

(95) Murphy, I. A.; Rice, P. S.; Monahan, M.; Zasada, L. B.; Miller, E. M.; Raugei, S.; Cossairt, B. M. Covalent Functionalization of Nickel Phosphide Nanocrystals with Aryl-Diazonium Salts. *Chem. Mater.* **2021**, *33* (24), 9652–9665. https://doi.org/10.1021/acs.chemmater.1c03255.

(96) Zhao, H.; Oyama, S. T.; Freund, H.-J.; Włodarczyk, R.; Sierka, M. Nature of Active Sites in Ni2P Hydrotreating Catalysts as Probed by Iron Substitution. *Appl. Catal. B Environ.* **2015**, *164*, 204–216. https://doi.org/10.1016/j.apcatb.2014.09.010.

(97) Li, C.; Gao, H.; Wan, W.; Mueller, T. Mechanisms for Hydrogen Evolution on Transition Metal Phosphide Catalysts and a Comparison to Pt(111). *Phys. Chem. Chem. Phys.* **2019**, *21* (44), 24489–24498. https://doi.org/10.1039/C9CP05094A.

(98) Hammer, B.; Hansen, L. B.; Nørskov, J. K. Improved Adsorption Energetics within Density-Functional Theory Using Revised Perdew-Burke-Ernzerhof Functionals. *Phys. Rev. B* **1999**, *59* (11), 7413–7421. https://doi.org/10.1103/PhysRevB.59.7413.

(99) Papawassiliou, W.; Carvalho, J. P.; Panopoulos, N.; Al Wahedi, Y.; Wadi, V. K. S.; Lu, X.; Polychronopoulou, K.; Lee, J. B.; Lee, S.; Kim, C. Y.; Kim, H. J.; Katsiotis, M.; Tzitzios, V.; Karagianni, M.; Fardis, M.; Papavassiliou, G.; Pell, A. J. Crystal and Electronic Facet Analysis of Ultrafine Ni2P Particles by Solid-State NMR Nanocrystallography. *Nat. Commun.* **2021**, *12* (1), 4334. https://doi.org/10.1038/s41467-021-24589-5.

(100) Wexler, R. B.; Martirez, J. M. P.; Rappe, A. M. Active Role of Phosphorus in the Hydrogen Evolving Activity of Nickel Phosphide (0001) Surfaces. *ACS Catal.* **2017**, *7* (11), 7718–7725. https://doi.org/10.1021/acscatal.7b02761.

(101) Cross, R. W.; Dzade, N. Y. First-Principles Mechanistic Insights into the Hydrogen Evolution Reaction on Ni2P Electrocatalyst in Alkaline Medium. *Catalysts* **2020**, *10* (3), 307. https://doi.org/10.3390/catal10030307.
(102) Hakala, M.; Laasonen, K. Hydrogen Adsorption Trends on Al-Doped Ni2P Surfaces for Optimal Catalyst Design. *Phys. Chem. Chem. Phys.* **2018**, *20* (20), 13785–13791. https://doi.org/10.1039/C8CP00927A.
(103) Moon, J.-S.; Jang, J.-H.; Kim, E.-G.; Chung, Y.-H.; Yoo, S. J.; Lee, Y.-K. The Nature of Active Sites of Ni2P Electrocatalyst for Hydrogen Evolution Reaction. *J. Catal.* **2015**, *326*, 92–99. https://doi.org/10.1016/j.jcat.2015.03.012.
(104) Ha, D.-H.; Han, B.; Risch, M.; Giordano, L.; Yao, K. P. C.; Karayaylali, P.; Shao-Horn, Y. Activity and Stability of Cobalt Phosphides for Hydrogen Evolution upon Water Splitting. *Nano Energy* **2016**, *29*, 37–45. https://doi.org/10.1016/j.nanoen.2016.04.034.
(105) Cao, X.; Tan, Y.; Zheng, H.; Hu, J.; Chen, X.; Chen, Z. Effect of Cobalt Phosphide (CoP) Vacancies on Its Hydrogen Evolution Activity via Water Splitting: A Theoretical Study. *Phys. Chem. Chem. Phys.* **2022**, *24* (7), 4644–4652. https://doi.org/10.1039/D1CP05739A.
(106) Cao, S.; Chen, Y.; Wang, H.; Chen, J.; Shi, X.; Li, H.; Cheng, P.; Liu, X.; Liu, M.; Piao, L. Ultrasmall CoP Nanoparticles as Efficient Cocatalysts for Photocatalytic Formic Acid Dehydrogenation. *Joule* **2018**, *2* (3), 549–557. https://doi.org/10.1016/j.joule.2018.01.007.
(107) Xin, Y.; Li, S.; Qian, Y.; Zhu, W.; Yuan, H.; Jiang, P.; Guo, R.; Wang, L. High-Entropy Alloys as a Platform for Catalysis: Progress, Challenges, and Opportunities. *ACS Catal.* **2020**, *10* (19), 11280–11306. https://doi.org/10.1021/acscatal.0c03617.
(108) Travert, A.; Nakamura, H.; van Santen, R. A.; Cristol, S.; Paul, J.-F.; Payen, E. Hydrogen Activation on Mo-Based Sulfide Catalysts, a Periodic DFT Study. *J. Am. Chem. Soc.* **2002**, *124* (24), 7084–7095. https://doi.org/10.1021/ja011634o.
(109) Lauritsen, J. V.; Kibsgaard, J.; Olesen, G. H.; Moses, P. G.; Hinnemann, B.; Helveg, S.; Nørskov, J. K.; Clausen, B. S.; Topsøe, H.; Lægsgaard, E.; Besenbacher, F. Location and Coordination of Promoter Atoms in Co- and Ni-Promoted MoS2-Based Hydrotreating Catalysts. *J. Catal.* **2007**, *249* (2), 220–233. https://doi.org/10.1016/j.jcat.2007.04.013.
(110) Aireddy, D. R.; Ding, K. Heterolytic Dissociation of H2 in Heterogeneous Catalysis. *ACS Catal.* **2022**, *12* (8), 4707–4723. https://doi.org/10.1021/acscatal.2c00584.
(111) Cai, J.; Song, Y.; Zang, Y.; Niu, S.; Wu, Y.; Xie, Y.; Zheng, X.; Liu, Y.; Lin, Y.; Liu, X.; Wang, G.; Qian, Y. N-Induced Lattice Contraction Generally Boosts the Hydrogen Evolution Catalysis of P-Rich Metal Phosphides. *Sci. Adv.* **2020**, *6* (1), eaaw8113. https://doi.org/10.1126/sciadv.aaw8113.
(112) Zhang, P.; Qiu, H.; Li, H.; He, J.; Xu, Y.; Wang, R. Nonmetallic Active Sites on Nickel Phosphide in Oxygen Evolution Reaction. *Nanomaterials* **2022**, *12* (7), 1130. https://doi.org/10.3390/nano12071130.
(113) Wang, G.; Shi, Y.; Mei, J.; Xiao, C.; Hu, D.; Chi, K.; Gao, S.; Duan, A.; Zheng, P. DFT Insights into Hydrogen Activation on the Doping Ni2P Surfaces under the Hydrodesulfurization Condition. *Appl. Surf. Sci.* **2021**, *538*, 148160. https://doi.org/10.1016/j.apsusc.2020.148160.
(114) Wei, L.; Liu, D.-J.; Rosales, B. A.; Evans, J. W.; Vela, J. Mild and Selective Hydrogenation of Nitrate to Ammonia in the Absence of Noble Metals. *ACS Catal.* **2020**, *10* (6), 3618–3628. https://doi.org/10.1021/acscatal.9b05338.
(115) Agarwal, R. G.; Coste, S. C.; Groff, B. D.; Heuer, A. M.; Noh, H.; Parada, G. A.; Wise, C. F.; Nichols, E. M.; Warren, J. J.; Mayer, J. M. Free Energies of Proton-Coupled Electron

Transfer Reagents and Their Applications. *Chem. Rev.* **2022**, *122* (1), 1–49. https://doi.org/10.1021/acs.chemrev.1c00521.

(116) Zhang, Q.; Bown, M.; Pastor-Pérez, L.; Duyar, M. S.; Reina, T. R. CO2 Conversion via Reverse Water Gas Shift Reaction Using Fully Selective Mo–P Multicomponent Catalysts. *Ind. Eng. Chem. Res.* **2022**, *61* (34), 12857–12865. https://doi.org/10.1021/acs.iecr.2c00305.

(117) Cui, S.; Wang, X.; Wang, L.; Zheng, X. Enhanced Selectivity of the CO2 Reverse Water–Gas Reaction over a Ni2P/CeO2 Catalyst. *Dalton Trans.* **2021**, *50* (17), 5978–5987. https://doi.org/10.1039/D1DT00424G.

(118) González-Castaño, M.; le Saché, E.; Berry, C.; Pastor-Pérez, L.; Arellano-García, H.; Wang, Q.; Reina, T. R. Nickel Phosphide Catalysts as Efficient Systems for CO2 Upgrading via Dry Reforming of Methane. *Catalysts* **2021**, *11* (4), 446. https://doi.org/10.3390/catal11040446.

(119) Yao, Z.; Luan, F.; Sun, Y.; Jiang, B.; Song, J.; Wang, H. Molybdenum Phosphide as a Novel and Stable Catalyst for Dry Reforming of Methane. *Catal. Sci. Technol.* **2016**, *6* (22), 7996–8004. https://doi.org/10.1039/C6CY00836D.

(120) Duyar, M. S.; Tsai, C.; Snider, J. L.; Singh, J. A.; Gallo, A.; Yoo, J. S.; Medford, A. J.; Abild-Pedersen, F.; Studt, F.; Kibsgaard, J.; Bent, S. F.; Nørskov, J. K.; Jaramillo, T. F. A Highly Active Molybdenum Phosphide Catalyst for Methanol Synthesis from CO and CO2. *Angew. Chem.* **2018**, *130* (46), 15265–15270. https://doi.org/10.1002/ange.201806583.

(121) Geng, F.; Bonita, Y.; Jain, V.; Magiera, M.; Rai, N.; Hicks, J. C. Bimetallic Ru–Mo Phosphide Catalysts for the Hydrogenation of CO2 to Methanol. *Ind. Eng. Chem. Res.* **2020**, *59* (15), 6931–6943. https://doi.org/10.1021/acs.iecr.9b06937.

(122) Ishikawa, H.; Sheng, M.; Nakata, A.; Nakajima, K.; Yamazoe, S.; Yamasaki, J.; Yamaguchi, S.; Mizugaki, T.; Mitsudome, T. Air-Stable and Reusable Cobalt Phosphide Nanoalloy Catalyst for Selective Hydrogenation of Furfural Derivatives. *ACS Catal.* **2021**, 750–757. https://doi.org/10.1021/acscatal.0c03300.

(123) Sheng, M.; Fujita, S.; Yamaguchi, S.; Yamasaki, J.; Nakajima, K.; Yamazoe, S.; Mizugaki, T.; Mitsudome, T. Single-Crystal Cobalt Phosphide Nanorods as a High-Performance Catalyst for Reductive Amination of Carbonyl Compounds. *JACS Au* **2021**, *1* (4), 501–507. https://doi.org/10.1021/jacsau.1c00125.

(124) Liu, P.; Rodriguez, J. A.; Asakura, T.; Gomes, J.; Nakamura, K. Desulfurization Reactions on Ni2P(001) and α-Mo2C(001) Surfaces: Complex Role of P and C Sites. *J. Phys. Chem. B* **2005**, *109* (10), 4575–4583. https://doi.org/10.1021/jp044301x.

(125) Ji, L.; Li, L.; Ji, X.; Zhang, Y.; Mou, S.; Wu, T.; Liu, Q.; Li, B.; Zhu, X.; Luo, Y.; Shi, X.; Asiri, A. M.; Sun, X. Highly Selective Electrochemical Reduction of CO2 to Alcohols on an FeP Nanoarray. *Angew. Chem. Int. Ed.* **2020**, *59* (2), 758–762. https://doi.org/10.1002/anie.201912836.

(126) Ye, S.; Chen, Z.; Zhang, G.; Chen, W.; Peng, C.; Yang, X.; Zheng, L.; Li, Y.; Ren, X.; Cao, H.; Xue, D.; Qiu, J.; Zhang, Q.; Liu, J. Elucidating the Activity, Mechanism and Application of Selective Electrosynthesis of Ammonia from Nitrate on Cobalt Phosphide. *Energy Environ. Sci.* **2022**, *15* (2), 760–770. https://doi.org/10.1039/D1EE03097C.

(127) Hong, Q.-L.; Zhou, J.; Zhai, Q.-G.; Jiang, Y.-C.; Hu, M.-C.; Xiao, X.; Li, S.-N.; Chen, Y. Cobalt Phosphide Nanorings towards Efficient Electrocatalytic Nitrate Reduction to Ammonia. *Chem. Commun.* **2021**, *57* (88), 11621–11624. https://doi.org/10.1039/D1CC04952F.

(128) Xu, Y.-F.; Duchesne, P. N.; Wang, L.; Tavasoli, A.; Ali, F. M.; Xia, M.; Liao, J.-F.; Kuang, D.-B.; Ozin, G. A. High-Performance Light-Driven Heterogeneous CO2 Catalysis with near-Unity Selectivity on Metal Phosphides. *Nat. Commun.* **2020**, *11* (1), 5149. https://doi.org/10.1038/s41467-020-18943-2.

(129) Zhang, X.; Yan, J.; Zheng, F.; Zhao, J.; Lee, L. Y. S. Designing Charge Transfer Route at the Interface between WP Nanoparticle and G-C3N4 for Highly Enhanced Photocatalytic CO2 Reduction Reaction. *Appl. Catal. B Environ.* **2021**, *286*, 119879. https://doi.org/10.1016/j.apcatb.2021.119879.

(130) Tang, J.; Yang, D.; Zhou, W.; Guo, R.; Pan, W.; Huang, C. Noble-Metal-Free Molybdenum Phosphide Co-Catalyst Loaded Graphitic Carbon Nitride for Efficient Photocatalysis under Simulated Irradiation. *J. Catal.* **2019**, *370*, 79–87. https://doi.org/10.1016/j.jcat.2018.12.009.

(131) Banerjee, S.; Kakekhani, A.; Wexler, R. B.; Rappe, A. M. Mechanistic Insights into CO2 Electroreduction on Ni2P: Understanding Its Selectivity toward Multicarbon Products. *ACS Catal.* **2021**, *11* (18), 11706–11715. https://doi.org/10.1021/acscatal.1c03639.

(132) Zhang, Q.; Pastor-Pérez, L.; Villora-Pico, J. J.; Joyce, M.; Sepúlveda-Escribano, A.; Duyar, M. S.; Reina, T. R. Ni-Phosphide Catalysts as Versatile Systems for Gas-Phase CO2 Conversion: Impact of the Support and Evidences of Structure-Sensitivity. *Fuel* **2022**, *323*, 124301. https://doi.org/10.1016/j.fuel.2022.124301.

(133) Carbajal, J. L.; White, R. E. Electrochemical Production and Corrosion Testing of Amorphous Ni-P. *J. Electrochem. Soc.* **1988**, *135* (12), 2952. https://doi.org/10.1149/1.2095468.

(134) Crobu, M.; Scorciapino, A.; Elsener, B.; Rossi, A. The Corrosion Resistance of Electroless Deposited Nano-Crystalline Ni–P Alloys. *Electrochimica Acta* **2008**, *53* (8), 3364–3370. https://doi.org/10.1016/j.electacta.2007.11.071.

(135) Elsener, B.; Crobu, M.; Scorciapino, M. A.; Rossi, A. Electroless Deposited Ni–P Alloys: Corrosion Resistance Mechanism. *J. Appl. Electrochem.* **2008**, *38* (7), 1053–1060. https://doi.org/10.1007/s10800-008-9573-8.

(136) Scorciapino, M. A.; Fantauzzi, M.; Crobu, M.; Navarra, G.; Elsener, B.; Rossi, A. Nanostructure of Surface Films on Ni18P Alloy in Sulfate Solutions by the Maximum Entropy Method. *ACS Omega* **2017**, *2* (11), 7790–7802. https://doi.org/10.1021/acsomega.7b00958.

(137) J. Kucernak, A. R.; Sundaram, V. N. N. Nickel Phosphide: The Effect of Phosphorus Content on Hydrogen Evolution Activity and Corrosion Resistance in Acidic Medium. *J. Mater. Chem. A* **2014**, *2* (41), 17435–17445. https://doi.org/10.1039/C4TA03468F.

(138) Kim, B.; Kim, T.; Lee, K.; Li, J. Recent Advances in Transition Metal Phosphide Electrocatalysts for Water Splitting under Neutral pH Conditions. *ChemElectroChem* **2020**, *7* (17), 3578–3589. https://doi.org/10.1002/celc.202000734.

Chapter 2. PROBING THE STABILITY OF NICKEL PHOSPHIDE NANOPARTICLES IN AIR

Significant portions of the following have previously been published.[1] X-ray spectroscopy experiments were conducted in collaboration with J. E. Abramson and G. T. Seidler.

2.1 ABSTRACT

Ni_2P is an effective catalyst for the hydrogen evolution reaction (HER), making it a promising replacement for Pt, the current state-of-the-art HER catalyst. However, Ni_2P and other TMPs are susceptible to oxidation, leading to catalyst degradation and loss in certain conditions. In the present work, *ex situ* P Kα and Kβ X-ray emission spectroscopy (XES) is used to investigate the degradation of Ni_2P nanoparticles in air. Upon exposure to air, as-synthesized Ni_2P nanoparticles were studied via P Kα and Kβ XES in an inert atmosphere glovebox. Results showed that the phosphide species converted to phosphate with analysis of intermediates well fit by a simple two-phase mixture. Additionally, the rate of oxidation agreed with a diffusion-limited model for oxidation.

2.2 INTRODUCTION

Ni_2P has been shown to be an effective catalyst for the hydrogen evolution reaction (HER), making it a promising replacement for Pt, which is the current state-of-the-art HER catalyst.[2,3] H_2 is a clean-energy critical fuel and chemical highlighted by the US Department of Energy's "Hydrogen Shot," which seeks to reduce "the cost of carbon-neutral hydrogen by 80% to $1 per 1 kg in 1 decade, highlighting the key role of hydrogen in implementing carbon-neutral solutions."[4] An early computational study proposed that Ni_2P would be an active catalyst for

HER due to what they coined as the "ensemble effect," where P helps modulate H binding to the metal surface so that H binds neither too strongly nor too weakly according to the Sabatier principle.[3,5] This "ensemble effect" helps metal phosphide catalysts behave more similarly to precious metals as opposed to the base metal component alone. Ni_2P is also a good or promising catalyst for other reactions, such as alcohol oxidation, hydrodesulfurization,[6,7] nitrate reduction, and oxygen evolution reaction.[8] However, although P alloying to metals improves metal stability,[9–12] Ni_2P and other transition metal phosphides (TMPs) are still susceptible to oxidation, which can lead to catalyst degradation and loss in certain conditions.[13,14] Stability is an important part of catalysis, especially for achieving the goals of the Hydrogen Shot. Therefore, it is important to understand complex degradation mechanisms in order to better understand structure-activity relationships in these materials. In the present work, *ex situ* P Kα and Kβ X-ray emission spectroscopy (XES) is used to understand the degradation of Ni_2P nanoparticles in air.

2.3 METHODS

2.3.1 *Reference sample preparation*

Nickel phosphide references were used to test the spectrometer and run the commissioning studies. A disodium hydrogen phosphate reference was used to set the energy scale by matching peaks to known energies,[15] see Figure 2.1. Pellets were made by pressing an approximately 1:1 mass ratio of commercial reference powders, Ni_2P (98%, Millipore-Sigma) or $Ni_3(PO_4)_2$ (98%, Alfa Aesar) or Na_2HPO_4 (98%, Millipore-Sigma), and BN powder (98%, Millipore-Sigma) into a 13 mm diameter die. These reference pellets were cut into approximately 10 mm × 5 mm × 1 mm sized pieces to fit in the spectrometer without collisions. Pellets were dried under vacuum at 80 °C overnight prior to use in the glovebox.

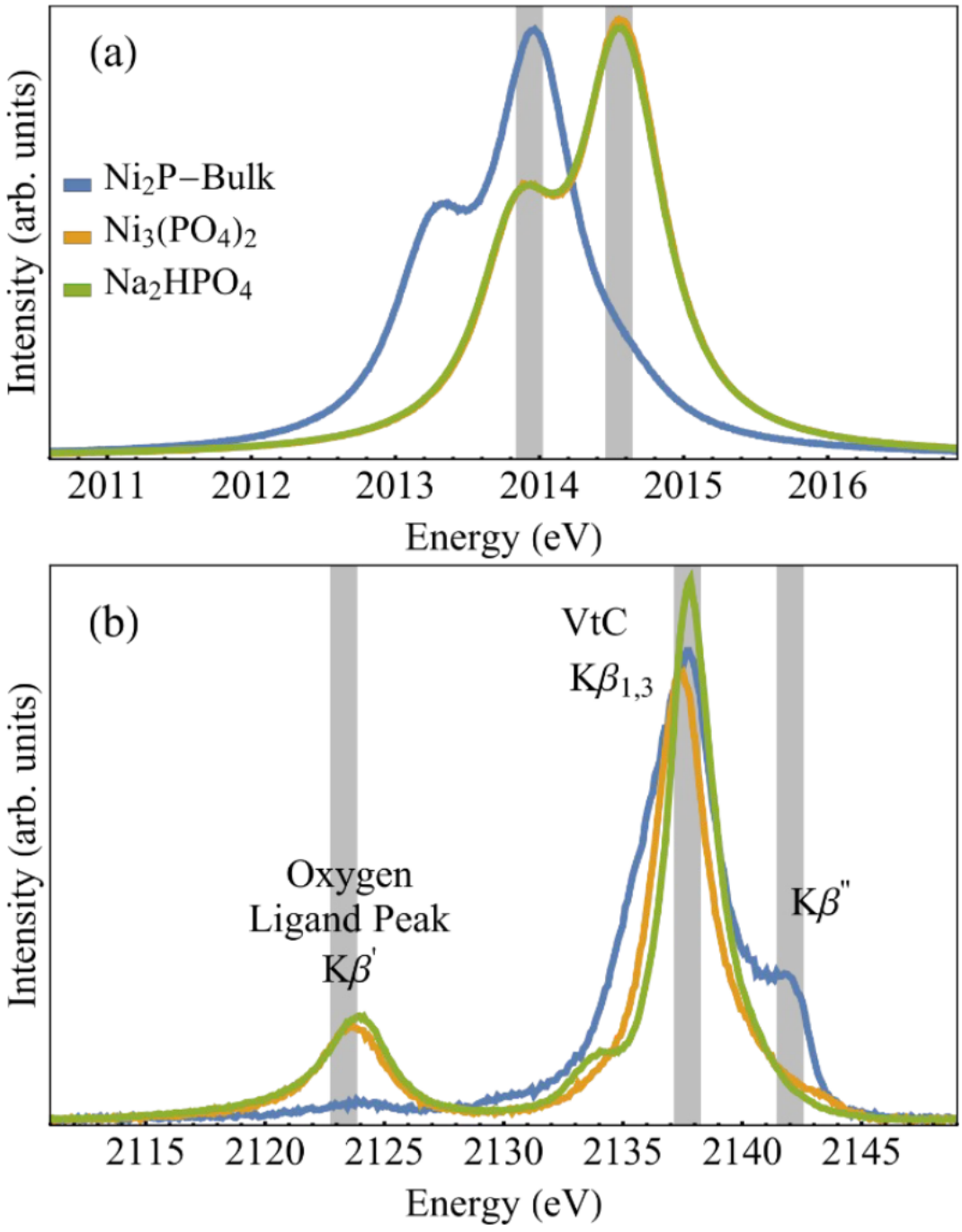

Figure 2.1. P Kα and Kβ reference spectra, Ni_2P-Bulk and $Ni_3(PO_4)_2$, with Na_2HPO_4 reference spectra. The Na_2HPO_4 spectra was used to set the energy scale.

2.3.2 *Ni_2P nanoparticle synthesis*

All glassware was dried at 160 °C overnight prior to use. All manipulations were performed using standard Schlenk techniques or inside a nitrogen atmosphere glovebox unless stated otherwise. Nickel(ii) chloride (98%, Millipore-Sigma) was dried at 100 °C under vacuum overnight before being stored in a nitrogen glovebox for use. Oleylamine (90% Technical Grade, Millipore-Sigma), pentane, and toluene were dried over CaH_2, distilled, and stored over 4 Å sieves in a nitrogen glovebox. Tris(diethylamino)phosphine (97%, Millipore-Sigma), 2-propanol (99.5% Anhydrous, Millipore-Sigma), and acetonitrile (99.8% Anhydrous, Millipore-Sigma) were stored in a nitrogen glovebox and used as received.

To synthesize Ni_2P nanoparticles, nickel(ii) chloride (472 mg, 3.6 mmol) was quickly transferred from the glovebox to a 3-neck round bottom flask connected to a Schlenk line before the reaction vessel was purged and refilled with dry N_2 three times. Then, oleylamine (24 mL) was quickly transferred from the glovebox to the reaction flask *via* a syringe. The solution was heated to 120 °C using a thermal probe inserted into a thermal well in contact with the solution and degassed for approximately one hour. Afterwards, the heat was turned off, and the solution was placed under an active N_2 flow and allowed to cool to approximately 70 °C.

Tris(diethylamino)phosphine (4.0 mL, 14 mmol) was then quickly transferred from the glovebox and injected into the reaction flask. The solution was heated to 250 °C and held for 1 hour prior to being cooled to near room temperature. Finally, the condenser columns and rubber septum were replaced with a glass stopper and t-adapter while flowing an overpressure of N_2 before being transferred into the glovebox through 15 fast cycles of evacuation and refill in the glovebox antechamber.

The nanoparticle solution was purified by centrifugation at 7830 rpm for 15 min with a 1:10 volume ratio of solution to 2-propanol. This was followed by three times decanting the supernatant, dissolving the solid pellet in minimal pentane, again adding a 10× volume ratio of 2-propanol, and centrifuging at 7830 rpm for 15 min. Finally, the supernatant was decanted, minimal toluene was used to dissolve the solid pellet, a 1:4 volume ratio for solvent : antisolvent was used with acetonitrile as the antisolvent, and the solution was centrifuged at 7830 rpm for 15 min. The supernatant was decanted, and the remaining solid was dissolved in pentane and dried under vacuum.

With the above synthesis completed, a concentrated solution of Ni_2P nanoparticles in toluene was drop cast on Si (100) wafers (Ted Pella). Seven replicate samples were made and mounted onto the sample wheel. The as-prepared samples are referred to as Ni_2P-0 h (meaning zero hours of air exposure) and are subsequently renamed based on air exposure time as Ni_2P-1 h, *etc.*

For the different air exposure times, nanoparticle samples were unmounted from the sample wheel and removed from the glovebox for the needed incremental air exposures to achieve the desired cumulative air exposure. Then, they were reloaded into the glovebox and remounted in the spectrometer.

2.3.3 *Measurement protocols*

All measurements were performed at ~100W X-ray tube power, *i.e.*, at 2.8 mA tube current and 35 kV accelerating potential. The instrument is allowed to thermalize for at least half an hour at the desired power before data collection – no spectral drift is observed between chronologically early and late scans. Prior to data acquisition, the spectrometer enclosure is flushed with helium gas for about 15 minutes until the counts for a reference sample plateau.

To minimize potential errors from finite sample size, sample homogeneity, or analyzer irregularities, we follow the methods of Abramson, *et al.*[16] This is performed by taking short two-minute camera exposures at each position while stepping individual samples by ~0.44 mm through the illumination region and summing the resulting spectra. This gives equal weight at all detected energies to all positions on the face of the sample regardless of size or concentration. Using this protocol, P Kα and Kβ spectra were collected as X-ray camera images for nanoparticle samples exposed to air for various amounts of time and reference compounds. Data was taken twice at each position on seven replicate samples for a total collection time of ~80 minutes per replicate sample, during which Kα and Kβ were collected simultaneously. This was repeated for each air exposure time.

Control software for the instrument is written in Python, and the user interface is presented in Jupyter. Users specify a sample map with each entry containing a name, sample wheel position, and integration time. Then, using the names given in the sample map, a list of scans is set up to run automatically with X-ray camera images saved for each scan.

The camera images for one sample are summed over the sample wheel movement to form a single image, and Figure 2.2 shows summed representative X-ray camera images for the dispersed fluorescence from a Ni_2P-0 h nanoparticle. In this image, the energy dispersive direction is horizontal, and the vertical direction shows the out-of-plane divergence. The curvature of the fluorescence on the camera face is due to the cylindrical analyzer geometry and is parameterized using a second-order polynomial fit to the center-of-masses calculated for each row after Gaussian filtering. The coefficients for this polynomial are used to assign each pixel of the detector to an energy bin, and the intensities associated with each such label are summed to produce the spectrum (processing software courtesy of easy XAFS LLC[17]). The energy scale is then set by measurement

of Na_2HPO_4, having $K\alpha_1$ and $K\beta_{1,3}$ energies of 2014.55 eV and 2137.80 eV, respectively, based on Petric *et al.*[15]

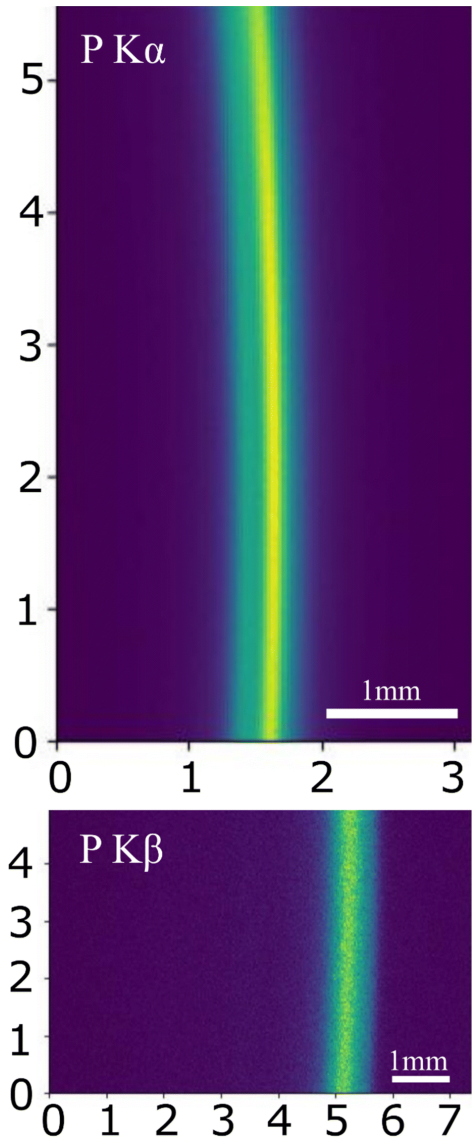

Figure 2.2. X-ray camera images of the dispersed fluorescence from a Ni_2P-0h nanoparticle sample: P Kα (above) and Kβ (below). The dispersive direction is horizontal, with lower to higher energy moving left to right. The vertical direction shows the out-of-plane dimensions, where minor curvature is observed from geometric effects, causing photons to be bent towards lower energy. The pixel intensity shown is from a CMOS sensor's analog to digital converter and is different from photon count because of sensor gain.

The spectra of all seven replicate samples at each time point were summed. Kα spectra were background subtracted using a linear background calculated using the first and last 2 eV of the spectra and then integral normalized. Kβ spectra were background subtracted using a linear background calculated using the first and last 5 eV of the measurement and then normalized using the associated Kα integral to place them on an approximate mole-weighted scale.

2.3.4 *Analysis techniques*

Linear superposition fitting was performed using Mathematica for the Ni_2P nanoparticle Kα spectra, using the Ni_2P-bulk and $Ni_3(PO_4)_2$ reference spectra as endpoints. The energy of the endpoint spectra was allowed to shift in order to accommodate the small differences in Kα energies known to occur within one nominal oxidation state.[15] These shifts averaged 0.013 eV for the phosphide reference and 0.10 eV for the phosphate reference.

2.3.5 *Electronic structure calculation*

The FEFF10 real-space multiple-scattering code[18,19] was used to calculate the XES using self-consistent potentials (SCPs), full-multiple-scattering (FMS), and Hedin-Lundqvist self-energy corrections. The use of FEFF10 for valence-to-core XES calculation has been discussed previously, such as by Mortensen, *et al.*[20] The cluster sizes used in the calculations were 6 Å for both the SCP and FMS calculations. For the bulk calculation, the structure was taken as the hexagonal crystal structure[21] with space group $P\bar{6}2m$. The Kβ XES was then calculated for each of the two inequivalent sites in the unit cell and stoichiometrically averaged to obtain the total Kβ XES spectrum. To approximate the surface Kβ XES spectrum of the nanoparticle, a 9 Å cluster was cut from the bulk, and the spectra of all surface P atoms were averaged.

2.4 Results and Discussion

2.4.1 *Synthesis and characterization of as-synthesized and annealed Ni_2P nanoparticles*

Nanoparticles were synthesized by degassing $NiCl_2$ in oleylamine at 120 °C for 1 h. The solution was then allowed to cool to ~50 °C prior to injecting tris(diethylamino)phosphine and heating to 250 °C for 1 h. Starting from 50 °C allows for the full diffusion of P precursor throughout the solution prior to reaching the nucleation temperature. A uniform distribution of P precursors in the solution encourages uniform nanoparticle growth and leads to low polydispersity nanoparticles. The final solution was then purified through centrifugation in pentane (solvent) and isopropanol (antisolvent), followed by centrifugation in toluene (solvent) and acetonitrile (antisolvent). The resulting Ni_2P nanoparticles, after purification, are from now on referred to as as-synthesized nanoparticles. Nanoparticles were analyzed via powder X-ray diffraction (XRD) and compared to a Ni_2P reference pattern (PDF 04-003-1863). Figure 2.3A shows that as-synthesized nanoparticles match the Ni_2P reference. Additionally, Scherrer analysis performed on the samples indicates that as-synthesized nanoparticles have an average crystallite domain size of 5 nm (Figure 2.3A). Figure 2.3B shows transmission electron microscopy (TEM) imaging of as-synthesized nanoparticles, showing an average nanoparticle diameter of 5 nm.

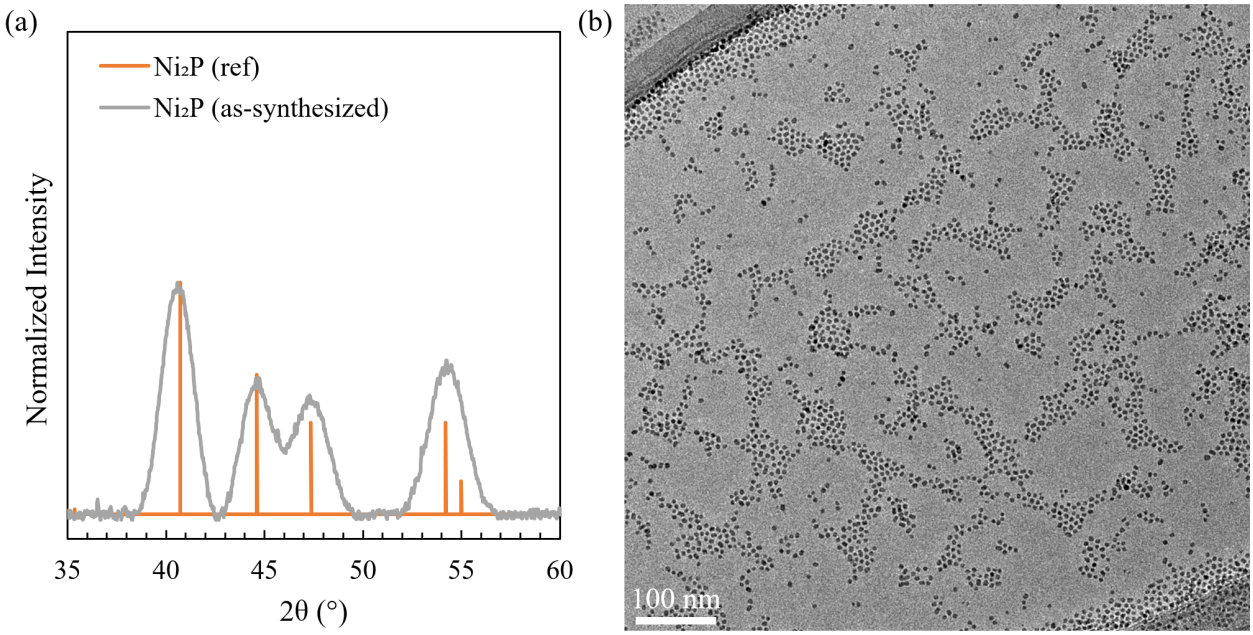

Figure 2.3. (a) XRD of as-synthesized Ni_2P nanoparticles compared to a Ni_2P reference pattern (PDF 04-003-1863). (b) TEM of as-synthesized Ni_2P nanoparticles.

2.4.2 *Air oxidation of as-synthesized Ni_2P nanoparticles over time*

Beginning with P Kα, which probes the P core-to-core transition and informs on the P oxidation state, we show in Figure 2.4 a representative averaged sample fit of Ni2P-24 h, using a linear superposition fitting to phosphide (Ni2P-bulk) and phosphate (Ni3(PO4)2) reference compound endpoints. In the top panel, the fit is performed with no broadening of the two endpoint reference spectra, and the residual shows clear discrepancies, indicating a weakness of the model. This isn't unexpected, as the nanophase materials have inhomogeneity from both their surface truncation (even if there are no surface adsorbates or other complications) and from the presence of an amorphous layer at the surface.[22] These effects are discussed further in the following paragraphs. Because of this inhomogeneity, we include 0.2 eV broadening of the reference spectra to allow for small differences in the Kα energies from slightly different local environments. The resulting fit, shown in the bottom panel of Figure 2.4, is much improved. Throughout all of the fits in the

aging sequence, we find a statistical error in the fraction phosphide of 0.01 or less from the standard error determined from the seven replicate samples at each time point for replicate fraction phosphide, standard deviation, and standard error. We also estimate a systematic error of the fitting of ±0.02 due to uncertainties in the use of the broadened-fit model.

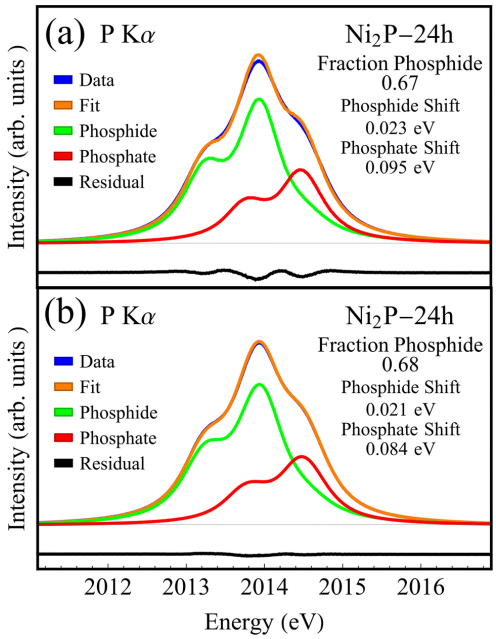

Figure 2.4. Linear superposition fit of the P Kα spectrum for an aged Ni_2P nanophase sample to phosphide (Ni_2P-bulk) and phosphate ($Ni_3(PO_4)_2$) references. (a) Fits using the reference spectra as directly measured. (b) Fits after the reference spectra have been broadened by 0.2 eV to compensate for a range of local environments; see the text for discussion.

Next, in Figure 2.5, we show P Kα data for as-synthesized Ni_2P nanoparticles that have been exposed to air for differing lengths of time, the phosphide reference, Ni_2P-bulk, and the phosphate reference, $Ni_3(PO_4)_2$. The reference spectra show the typical Kα line shape, i.e., two peaks ($K\alpha_1$ and $K\alpha_2$) with a roughly 2:1 peak intensity ratio and a small trough in between. Additionally, the reference spectra show the expected trend in energy shift with the oxidation state.

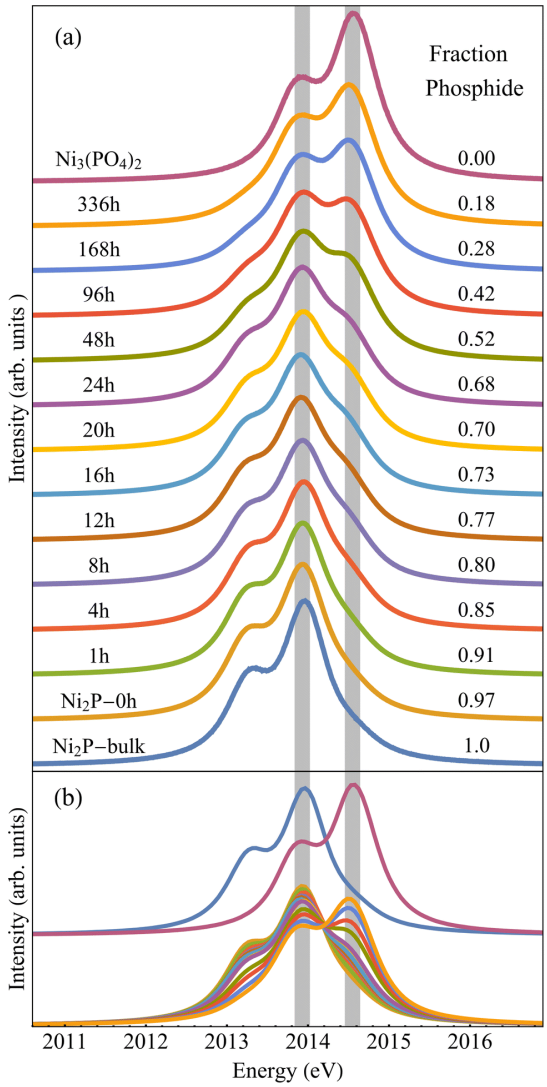

Figure 2.5. P Kα data for the Ni_2P-0h nanoparticles exposed to air for differing lengths of time and two reference samples, Ni_2P-bulk and $Ni_3(PO_4)_2$. Typical total measurement times for an ensemble of seven nanophase samples (averaged to give the results shown) is 9 hours, ~80 minutes per sample. Panel (a) shows the spectra offset with vertical guides, shaded bands, for the $K\alpha_1$ peaks of the phosphide and phosphate reference compounds. Panel (b) shows the same spectrum overlaid. Note that the apparent isosbestic point is ~2014.25 eV, supporting the use of a simple two-phase decomposition onto reference compounds.

The air-exposed, replicate-averaged Ni_2P nanoparticle spectra, to varying degrees, no longer show just two distinct $K\alpha_1/K\alpha_2$ peaks, indicating a mixed P oxidation state. The increase in intensity at 2014.55 eV paired with the decrease in intensity at 2013.80 eV (the two gray energy bands in Figure 2.5) indicates a shift to a larger percentage of highly oxidized P upon increased air exposure. Figure 2.5B shows that the Ni_2P nanoparticle spectra have an approximate isosbestic point, suggesting that the transition in P oxidation is a simple two-phase mixture. Given this, linear combination fitting of the Ni_2P nanoparticle spectra was performed to obtain a value for the P fraction that has not been oxidized, listed in Figure 2.5A as fraction phosphide.

In Figure 2.6, we show Kβ spectra for the as-synthesized Ni_2P nanoparticles and references; again, this was collected simultaneously with the Kα results shown in Figure 2.5. P Kβ probes the valence-to-core transition, which informs on P's chemical environment and electronic structure. The Kβ reference spectra show all the expected features with high energy resolution: the main $K\beta_{1,3}$ peak, oxygen ligand Kβ′ peak for $Ni_3(PO_4)_2$, and Kβ″ side peak for Ni_2P-bulk. The lack of features with known lifetimes makes it difficult to estimate the energy resolution of the Kβ spectrometer, but the good performance certainly indicates an energy resolution safely better than 0.8 eV. These reference Kβ spectra agree with previous phosphate and phosphide results.[15,23,24] The Ni_2P nanophase Kβ spectra, interestingly, show both similarities and differences with respect to the reference compounds. This is particularly notable when comparing the Ni_2P-bulk reference to the Ni_2P-0h nanoparticle sample – the Ni_2P-0h nanoparticle sample contains only about 4% phosphate from the P Kα fitting; therefore, our initial expectation was that the Kβ spectra of the nanophase would agree well with that of bulk Ni_2P.

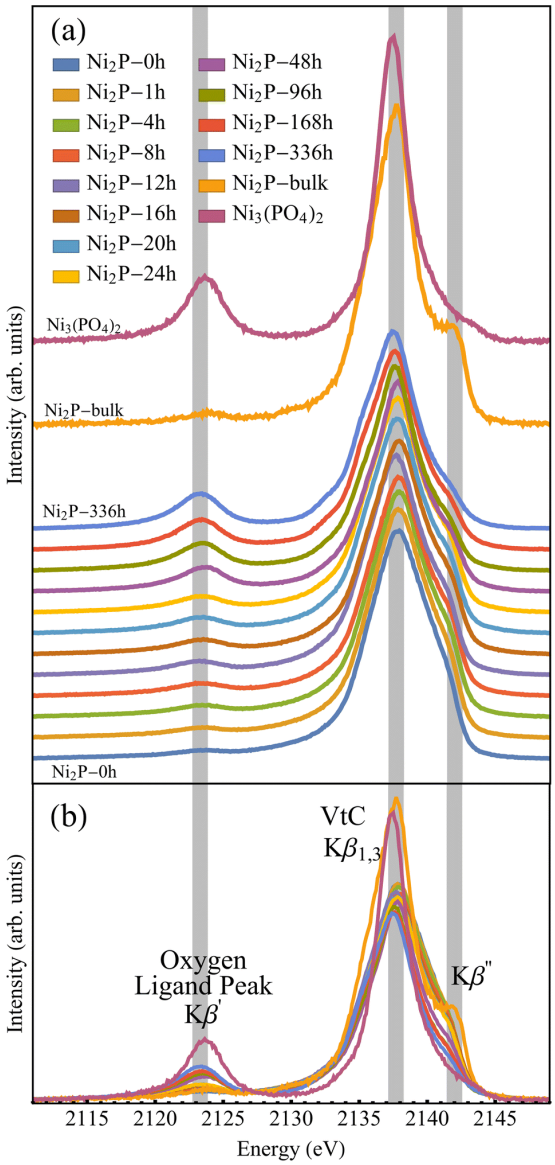

Figure 2.6. (a) P Kβ spectra, offset for clarity of presentation, for the aging sequence of Ni_2P nanoparticles and the two reference samples, Ni_2P-bulk and $Ni_3(PO_4)_2$. (b) The same spectra are shown on a single intensity scale. Note that as the air exposure time of the samples increases, there is a subtle shift in the main $K\beta_{1,3}$ peak and satellite $K\beta''$ peak, in addition to a steady increase in the intensity of the oxygen ligand peak.

The main difference is the spectral line shape of the main $K\beta_{1,3}$ peak (~2137.80 eV), both in terms of its greater width and the decreased prominence of the $K\beta''$ side peak (~2142.00 eV). It is important to remember, however, that the nanoparticles have a mean diameter of only 5 nm

and, further, that TEM typically shows a disordered Ni- and P-containing layer at the surface. Comparing the average sizes of nanoparticles obtained by analyzing TEM images (~5 nm in diameter) and average crystallite domain sizes obtained by applying the Scherrer equation to peaks in the diffractogram (~4 nm in diameter, batch 1) demonstrates that the surface layer is approximately 0.5 nm. Surface amorphization is seen in other studies as well,[25–28] including one which estimated the disordered surface layer thickness of Ni_2P nanoparticles to be between 0.55 nm and 0.75 nm depending on surface facet terminations.[22] While it is not possible to model this disordered phase without additional information about its composition, the general effect of the nanoparticle surface, compared to the bulk, on the electronic structure can be modeled. In Figure 2.7, we show the predicted bulk and near-surface contributions of an idealized crystalline Ni_2P nanoparticle. The general character of the deviation between bulk Ni_2P and the native nanophase Ni_2P-0h is in reasonable agreement with theory – the Kβ″ side peak shifts to lower energy, and the main $K\beta_{1,3}$ peak broadens.

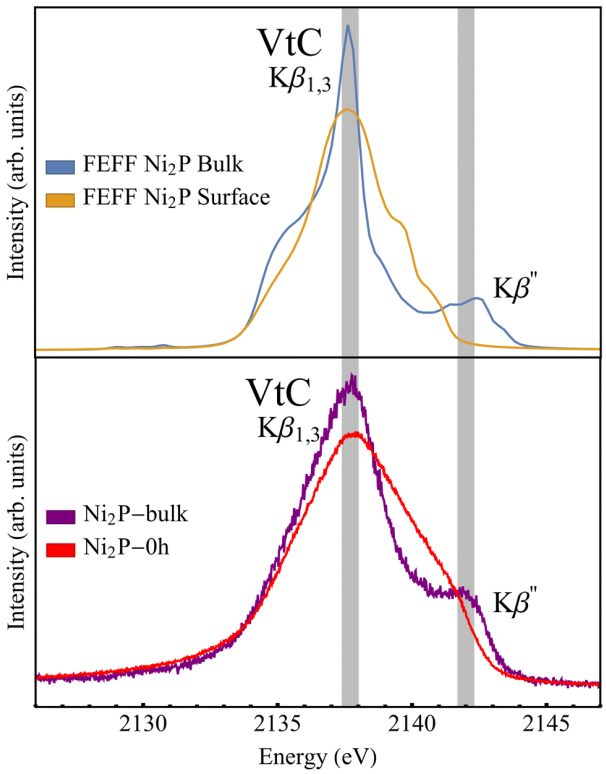

Figure 2.7. FEFF calculations for Ni_2P bulk and Ni_2P surface materials are shown with data for Ni_2P-bulk and Ni_2P nanoparticles, Ni_2P-0h. The differences between the bulk and surface theoretical spectra are in qualitative agreement with the deviations between the (macroscopic) crystalline Ni_2P-bulk reference and the Ni_2P-0h spectra.

Hence, while we can perform a simple linear superposition analysis of the Kα spectra to extract an estimate of P oxidation, no similar analysis is possible with the Kβ spectra, apparently due to electronic and structural differences near the surface of the nanoparticles. This being said, the Kβ data show an increased presence of P–O bonds (i.e., higher oxidation state P) with longer air exposure via the increasing strength of the oxygen ligand peak, Kβ′ at ~2124 eV.

The increased air exposure of the Ni_2P nanoparticle samples shows a consistent increase in phosphate character across both Kα and Kβ spectra. In Figure 2.8, we show the phosphide fraction derived from fitting the Kα spectra to the references (as above) and a scaled representation of the integral of the oxygen ligand peak in the Kβ spectra, both plotted against

the square root of air exposure time. Although the intensity of the ligand integral should be roughly proportional to the occurrence of P–O bonding, the absence of a valid fully-oxidized reference compound because of the nanoscale effects discussed above, along with the effects of extreme sensitivity to oxygen ligand 2s energy and bond length,[29] makes it impossible to assign a phosphide fraction metric to the ligand peak integral intensity on its own basis. Hence, the ligand integral results are scaled using the Kα-derived phosphide fractions at the 0 h and 336 h extrema – the resulting general agreement is clear. The roughly linear trend as a function of the square root of air exposure time hints at a diffusion-limited model of P oxidation in the as-synthesized Ni_2P nanoparticles.

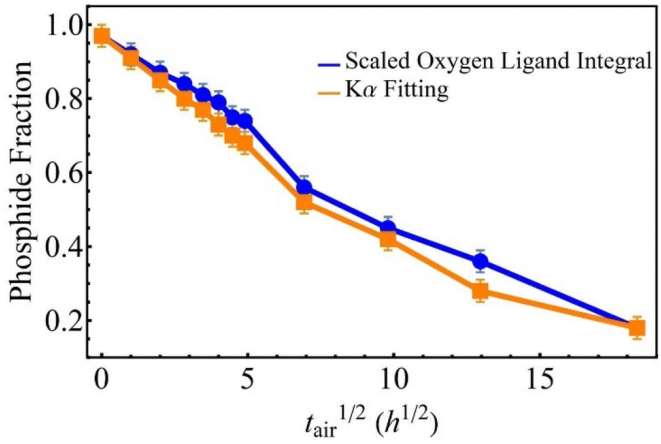

Figure 2.8. The phosphide fraction extracted from fits to Kα and from the scaling of the oxygen ligand integral in Kβ (see the text), as a function of the square root of air exposure time, $t_{air}^{1/2}$. Both plots show a negative trend with increasing air exposure in rough agreement with a diffusion-limited model of oxidation.

2.5 Conclusions

In conclusion, we studied the air oxidation of Ni_2P nanoparticles using P Kα and Kβ XES in a controlled atmosphere glovebox with excellent energy resolution and short acquisition times. As-synthesized Ni_2P nanoparticles oxidize in air, consistent with a diffusion-limited model. The corrosion of the Ni_2P nanoparticles was well fit by a simple two-component mixture of phosphide

and phosphate. Finally, we saw that nanoparticle surface amorphization significantly impacts the P Kβ lineshape. Air is the most ubiquitous environment that Ni_2P nanoparticles could encounter. This study will help scientists and engineers better account for and better understand the oxidation mechanism of Ni_2P nanoparticles in air. Future studies should compare the air oxidation response of Ni_2P nanoparticles with different surface environments, e.g., covalently functionalized surface ligands and an annealed bare surface.

2.6 REFERENCES

(1) Abramson, J. E.; Holden, W. M.; Rivera-Maldonado, R. A.; Velian, A.; Cossairt, B. M.; Seidler, G. T. A Laboratory X-Ray Emission Spectrometer for Phosphorus Kα and Kβ Study of Air-Sensitive Samples. *J. Anal. At. Spectrom.* **2023**. https://doi.org/10.1039/D3JA00053B.

(2) Popczun, E. J.; McKone, J. R.; Read, C. G.; Biacchi, A. J.; Wiltrout, A. M.; Lewis, N. S.; Schaak, R. E. Nanostructured Nickel Phosphide as an Electrocatalyst for the Hydrogen Evolution Reaction. *J. Am. Chem. Soc.* **2013**, *135* (25), 9267–9270. https://doi.org/10.1021/ja403440e.

(3) Liu, P.; Rodriguez, J. A. Catalysts for Hydrogen Evolution from the [NiFe] Hydrogenase to the Ni2P(001) Surface: The Importance of Ensemble Effect. *J. Am. Chem. Soc.* **2005**, *127* (42), 14871–14878. https://doi.org/10.1021/ja0540019.

(4) Bullock, M.; More, K. *Basic Energy Sciences Roundtable: Foundational Science for Carbon-Neutral Hydrogen Technologies (Report)*; DOESC Office of Basic Energy Sciences, 2022. https://doi.org/10.2172/1834317.

(5) Kibsgaard, J.; Tsai, C.; Chan, K.; Benck, J. D.; Nørskov, J. K.; Abild-Pedersen, F.; Jaramillo, T. F. Designing an Improved Transition Metal Phosphide Catalyst for Hydrogen Evolution Using Experimental and Theoretical Trends. *Energy Environ. Sci.* **2015**, *8* (10), 3022–3029. https://doi.org/10.1039/C5EE02179K.

(6) Layan Savithra, G. H.; Muthuswamy, E.; Bowker, R. H.; Carrillo, B. A.; Bussell, M. E.; Brock, S. L. Rational Design of Nickel Phosphide Hydrodesulfurization Catalysts: Controlling Particle Size and Preventing Sintering. *Chem. Mater.* **2013**, *25* (6), 825–833. https://doi.org/10.1021/cm302680j.

(7) Rodriguez, J. A.; Kim, J.-Y.; Hanson, J. C.; Sawhill, S. J.; Bussell, M. E. Physical and Chemical Properties of MoP, Ni2P, and MoNiP Hydrodesulfurization Catalysts: Time-Resolved X-Ray Diffraction, Density Functional, and Hydrodesulfurization Activity Studies. *J. Phys. Chem. B* **2003**, *107* (26), 6276–6285. https://doi.org/10.1021/jp022639q.

(8) Menezes, P. W.; Indra, A.; Das, C.; Walter, C.; Göbel, C.; Gutkin, V.; Schmeiβer, D.; Driess, M. Uncovering the Nature of Active Species of Nickel Phosphide Catalysts in High-Performance Electrochemical Overall Water Splitting. *ACS Catal.* **2017**, *7* (1), 103–109. https://doi.org/10.1021/acscatal.6b02666.

(9) Carbajal, J. L.; White, R. E. Electrochemical Production and Corrosion Testing of Amorphous Ni-P. *J. Electrochem. Soc.* **1988**, *135* (12), 2952. https://doi.org/10.1149/1.2095468.
(10) Elsener, B.; Crobu, M.; Scorciapino, M. A.; Rossi, A. Electroless Deposited Ni–P Alloys: Corrosion Resistance Mechanism. *J. Appl. Electrochem.* **2008**, *38* (7), 1053–1060. https://doi.org/10.1007/s10800-008-9573-8.
(11) Elsener, B.; Atzei, D.; Krolikowski, A.; Rossi Albertini, V.; Sadun, C.; Caminiti, R.; Rossi, A. From Chemical to Structural Order of Electrodeposited Ni22P Alloy: An XPS and EDXD Study. *Chem. Mater.* **2004**, *16* (22), 4216–4225. https://doi.org/10.1021/cm030606x.
(12) J. Kucernak, A. R.; Sundaram, V. N. N. Nickel Phosphide: The Effect of Phosphorus Content on Hydrogen Evolution Activity and Corrosion Resistance in Acidic Medium. *J. Mater. Chem. A* **2014**, *2* (41), 17435–17445. https://doi.org/10.1039/C4TA03468F.
(13) Ha, D.-H.; Han, B.; Risch, M.; Giordano, L.; Yao, K. P. C.; Karayaylali, P.; Shao-Horn, Y. Activity and Stability of Cobalt Phosphides for Hydrogen Evolution upon Water Splitting. *Nano Energy* **2016**, *29*, 37–45. https://doi.org/10.1016/j.nanoen.2016.04.034.
(14) Parra-Puerto, A.; Ng, K. L.; Fahy, K.; Goode, A. E.; Ryan, M. P.; Kucernak, A. Supported Transition Metal Phosphides: Activity Survey for HER, ORR, OER, and Corrosion Resistance in Acid and Alkaline Electrolytes. *ACS Catal.* **2019**, 11515–11529. https://doi.org/10.1021/acscatal.9b03359.
(15) Petric, M.; Bohinc, R.; Bučar, K.; Žitnik, M.; Szlachetko, J.; Kavčič, M. Chemical State Analysis of Phosphorus Performed by X-Ray Emission Spectroscopy. *Anal. Chem.* **2015**, *87* (11), 5632–5639. https://doi.org/10.1021/acs.analchem.5b00782.
(16) Abramson, J. E.; Avalos, N. M.; Bourchy, A. L. M.; Saslow, S. A.; Seidler, G. T. An Exploration of Benchtop X-Ray Emission Spectroscopy for Precise Characterization of the Sulfur Redox State in Cementitious Materials. *X-Ray Spectrom.* **2022**, *51* (2), 151–162. https://doi.org/10.1002/xrs.3276.
(17) Holden, W. M.; Hoidn, O. R.; Seidler, G. T.; DiChiara, A. D. A Color X-Ray Camera for 2–6 keV Using a Mass Produced Back Illuminated Complementary Metal Oxide Semiconductor Sensor. *Rev. Sci. Instrum.* **2018**, *89* (9), 093111. https://doi.org/10.1063/1.5047934.
(18) Kas, J. J.; Vila, F. D.; Pemmaraju, C. D.; Tan, T. S.; Rehr, J. J. Advanced Calculations of X-Ray Spectroscopies with FEFF10 and Corvus. *J. Synchrotron Radiat.* **2021**, *28* (6), 1801–1810. https://doi.org/10.1107/S1600577521008614.
(19) Rehr, J. J.; Albers, R. C. Theoretical Approaches to X-Ray Absorption Fine Structure. *Rev. Mod. Phys.* **2000**, *72* (3), 621–654. https://doi.org/10.1103/RevModPhys.72.621.
(20) Mortensen, D. R.; Seidler, G. T.; Kas, J. J.; Govind, N.; Schwartz, C. P.; Pemmaraju, S.; Prendergast, D. G. Benchmark Results and Theoretical Treatments for Valence-to-Core x-Ray Emission Spectroscopy in Transition Metal Compounds. *Phys. Rev. B* **2017**, *96* (12), 125136. https://doi.org/10.1103/PhysRevB.96.125136.
(21) Larsson, Egon. X-Ray Investigation of the Ni-P System and the Crystal Structures of NiP and NiP2. *Ark. Foer Kemi* **1965**, *23* (32), 335–65.
(22) Papawassiliou, W.; Carvalho, J. P.; Panopoulos, N.; Al Wahedi, Y.; Wadi, V. K. S.; Lu, X.; Polychronopoulou, K.; Lee, J. B.; Lee, S.; Kim, C. Y.; Kim, H. J.; Katsiotis, M.; Tzitzios, V.; Karagianni, M.; Fardis, M.; Papavassiliou, G.; Pell, A. J. Crystal and Electronic Facet

Analysis of Ultrafine Ni2P Particles by Solid-State NMR Nanocrystallography. *Nat. Commun.* **2021**, *12* (1), 4334. https://doi.org/10.1038/s41467-021-24589-5.

(23) Stein, J. L.; Holden, W. M.; Venkatesh, A.; Mundy, M. E.; Rossini, A. J.; Seidler, G. T.; Cossairt, B. M. Probing Surface Defects of InP Quantum Dots Using Phosphorus Kα and Kβ X-Ray Emission Spectroscopy. *Chem. Mater.* **2018**, *30* (18), 6377–6388. https://doi.org/10.1021/acs.chemmater.8b02590.

(24) Sugiura, C. X-Ray Emission Spectra and Electronic Structures of Red Phosphorus, 3d Transition-Metal Phosphides and III–V Compounds. *J. Phys. Soc. Jpn.* **1995**, *64* (7), 2510–2523. https://doi.org/10.1143/JPSJ.64.2510.

(25) Murphy, I. A.; Rice, P. S.; Monahan, M.; Zasada, L. B.; Miller, E. M.; Raugei, S.; Cossairt, B. M. Covalent Functionalization of Nickel Phosphide Nanocrystals with Aryl-Diazonium Salts. *Chem. Mater.* **2021**, *33* (24), 9652–9665. https://doi.org/10.1021/acs.chemmater.1c03255.

(26) Wang, J.; Johnston-Peck, A. C.; Tracy, J. B. Nickel Phosphide Nanoparticles with Hollow, Solid, and Amorphous Structures. *Chem. Mater.* **2009**, *21* (19), 4462–4467. https://doi.org/10.1021/cm901073k.

(27) Moreau, L. M.; Ha, D.-H.; Zhang, H.; Hovden, R.; Muller, D. A.; Robinson, R. D. Defining Crystalline/Amorphous Phases of Nanoparticles through X-Ray Absorption Spectroscopy and X-Ray Diffraction: The Case of Nickel Phosphide. *Chem. Mater.* **2013**, *25* (12), 2394–2403. https://doi.org/10.1021/cm303490y.

(28) Mundy, M. E.; Ung, D.; Lai, N. L.; Jahrman, E. P.; Seidler, G. T.; Cossairt, B. M. Aminophosphines as Versatile Precursors for the Synthesis of Metal Phosphide Nanocrystals. *Chem. Mater.* **2018**, *30* (15), 5373–5379. https://doi.org/10.1021/acs.chemmater.8b02206.

(29) MacMillan, S. N.; Walroth, R. C.; Perry, D. M.; Morsing, T. J.; Lancaster, K. M. Ligand-Sensitive But Not Ligand-Diagnostic: Evaluating Cr Valence-to-Core X-Ray Emission Spectroscopy as a Probe of Inner-Sphere Coordination. *Inorg. Chem.* **2015**, *54* (1), 205–214. https://doi.org/10.1021/ic502152r.

Chapter 3. PROBING THE STABILITY OF NICKEL PHOSPHIDE NANOPARTICLE ELECTROCATALYSTS IN AQUEOUS ELECTROLYTES VIA *OPERANDO* X-RAY ABSORPTION SPECTROSCOPY

Significant portions of the following have previously been published.[1] X-ray spectroscopy experiments were conducted in collaboration with A. Gironda, D. Dean-Hill, J. E. Abramson, G. T. Seidler, and easyXAFS LLC. Electrochemistry experiments were carried out in collaboration with A. Varughese and D.-Y. Kuo. Transmission electron microscopy by H. Nguyen.

3.1 ABSTRACT

Earth-abundant catalysts are necessary for the global electrification of the petrochemical industry. Ni_2P is an earth-abundant electrocatalyst that has already been shown to catalyze various reactions, including hydrogen evolution and nitrate reduction. However, Ni_2P is susceptible to corrosion. In this study, we investigate the electrochemical corrosion of Ni_2P nanoparticles through anodic polarization experiments in acidic, neutral, and basic pH electrolytes and dive deeper into the corrosion mechanism of Ni_2P nanoparticles in neutral phosphate-buffered electrolyte solution via laboratory-based *operando* Ni K-edge X-ray absorption spectroscopy. Our results demonstrate that Ni_2P nanoparticles corrode significantly before achieving a passive surface. The corrosion follows a phosphate-first pathway, followed by the rapid oxidation of excess Ni to form a passive surface. Approximately 80-90% of Ni dissolves before passivation is achieved. Future work with Ni_2P should consider the chemical structure of its surface in aqueous conditions and take advantage of its anodic passivation.

3.2 INTRODUCTION

Electrification of the petrochemical industry has the potential to significantly reduce greenhouse gas emissions in the manufacturing of commodity chemicals; however, electrification on a global scale is only achievable using earth-abundant materials for electrocatalysis in place of state-of-the-art catalysts made from precious metals. Nickel phosphide (Ni_2P) is a promising earth-abundant catalyst that has been used for industrial hydrodesulfurization,[2,3] as well as electrocatalytic hydrogen evolution,[4,5] nitrate reduction,[6] carbon dioxide reduction,[7] and oxygen evolution.[8,9] Ni_2P and other transition metal phosphides benefit from active site ensembles that moderate the binding of reaction intermediates compared to their pure metal counterparts.[4,10] This makes metal phosphides promising electrocatalysts for reactions beyond those listed, especially for other hydrogenation reactions. The ensemble effect seen in Ni_2P, for example, causes the Ni_2P surface to bind H appropriately for efficient turnover of H_2, unlike Ni alone, which binds H too strongly and thus inhibits catalytic activity.[4,11]

However, Ni_2P is susceptible to oxidation, leading to catalyst corrosion in acidic and basic conditions, including 0.5 M H_2SO_4, 0.1 M $HClO_4$, and 0.1 M KOH.[12,13] Stability is essential for scalable catalysis; therefore, it is crucial to understand the degradation mechanism of Ni_2P to mitigate corrosion, accurately predict surface reactivity, and prepare Ni_2P for industrial electrocatalysis. Previous reports on Ni-P alloys found passivation regimes through anodic polarization in near-neutral pH electrolytes below 0.2 V vs. SCE but saw further corrosion after polarizing towards more anodic potentials.[14,15] Bulk nickel phosphides, however, have been shown to have a passivated surface, and characterization, often limited to ex-situ spectroscopy after catalysis, has shown that the surface is composed of nickel hydroxides, phosphates, and oxyhydroxides.[14,16,17] In the present work, *operando* Ni K-edge X-ray absorption spectroscopy and

electrochemical polarization are applied to understand the degradation of Ni_2P nanoparticles. This work leverages the use of benchtop X-ray spectrometers, which provide accessibility and the possibility of routine investigations of corrosion for various materials containing elements across the periodic table. They can be readily used to probe corrosion, including oxidation and material loss, through the use of *in situ* or *operando* cells. Laboratory X-ray measurements were made possible by implementing a low-absorption electrolytic cell optimized for transmission-mode XAS measurements. The cell enabled *operando* measurements with a clear line of sight for x-ray beam transmittance through a sufficiently thin glassy carbon sample window and was constructed with low-z materials to reduce unwanted absorption outside the sample material.

3.3 METHODS

3.3.1 *Materials*

Tris(diethylamino)phosphine (Sigma-Aldrich, 97%), isopropanol (Sigma-Aldrich, 99.5%, anhydrous), and acetonitrile (Sigma-Aldrich, 99.8%, anhydrous) were stored in an N_2-atmosphere glovebox and used without further purification. $NiCl_2 \cdot 6H_2O$ (Sigma-Aldrich, ReagentPlus) was dried under vacuum at approximately 80 °C and stored in an N_2-atmosphere glovebox. Toluene and pentane were transferred from solvent stills into an N_2-atmosphere glovebox. Oleylamine [SAFC, ≥98% (primary amine)] was distilled on a Schlenk line and vacuum filtered through Celite in an N_2-atmosphere glovebox. Carbon fiber paper (Fuel Cell Store) was cut into 2×2 cm^2 squares and then washed in 0.5 M H_2SO_4 by sonicating for 15 min and decanting; next, the carbon fiber squares were washed in 18 MΩ water by sonicating for 5 min and decanting 3 times; finally, the carbon fiber squares were dried in an oven before storage in an N_2-atmosphere glovebox. Electrolyte solutions were made as follows: 1 M phosphate

buffer was made by mixing 0.5 mol K_2HPO_4 (Fisher Scientific, 99.3%) and 0.5 mol KH_2PO_4 (Fisher Scientific, 99.7%) with 18 MΩ water per L of solution, 0.5 M H_2SO_4 was made by mixing 0.5 mol H_2SO_4 (Aldrich, 99.999%) and 18 MΩ water per L of solution, and 0.1 M KOH (Sigma-Aldrich, 99.99%) was made by mixing 0.1 mol KOH with 18 MΩ water per L of solution. Bulk Ni_2P (Sigma-Aldrich, ~100 mesh, 98%), $Ni_3(PO_4)_2 \cdot 8(H_2O)$ (Alfa Aesar, 98+%), and NiO (Strem, 99%, green) references for X-ray absorption spectroscopy were each made by mixing with xanthan gum in cellulose.

3.3.2 *Nanoparticle synthesis*

Nanoparticles of Ni_2P were synthesized following the procedure outlined by Murphy et al..[18] $NiCl_2$ (311 mg, 2.4 mmol) and oleylamine (17 mL) were degassed on a Schlenk line at 120 °C for 1 h. Next, the temperature was allowed to cool to approximately 50 °C, and tris(diethylamino)phosphine (2.63 mL, 9.6 mmol) was injected into the solution while the reaction apparatus was under active N_2 flow. The reaction mixture was then heated to 250 °C and held at 250 °C for 1 h. Afterward, the mixture was allowed to cool and then cycled into an N_2-atmosphere glovebox for workup. Inside the glovebox, the mixture was transferred to centrifuge tubes and mixed with isopropanol (10x the volume of the reaction mixture). The centrifuge tubes were spun down at 7800 rpm for 13 min and then decanted. Minimal pentane (solvent) was added to redissolve the nanoparticle pellets remaining at the bottom of the centrifuge tubes, and isopropanol (antisolvent) was then added to the mixture (1:10 solvent: antisolvent volume ratio). The mixture was then centrifuged for 13 min at 7800 rpm. This procedure was repeated twice as described, and a third time, with toluene as the solvent and acetonitrile as the antisolvent (1:4 solvent: antisolvent volume ratio). After decanting, nanoparticles were redispersed in toluene or pentane and dried under vacuum. After drying, nanoparticles were redispersed in toluene (10 or

15 mg/mL). Working electrodes were made by depositing 4 mg of Ni_2P (0.4 mL or 0.267 mL) from stock solution onto the previously described 2×2 cm^2 carbon fiber squares via drop casting from a syringe pump at a rate of 5 μL/min. Finally, Ni_2P-loaded carbon fiber squares were thermally annealed in a tube furnace (ThermoScientific Lindberg Blue M) at 450 °C for 2 h under a flow of 5% H_2/95% N_2 (Linde, HydroStar H5N K).

Transmission electron microscopy (FEI Tecnai G2 F20 Supertwin) images of the nanoparticles after workup were obtained by depositing 10 μL of dilute solution in toluene onto holey carbon TEM grids (Ted Pella Lacey carbon on 400 mesh Cu) and allowing the solution to air dry. Before imaging, samples were further dried under vacuum overnight. Scanning electron microscopy (ThermoFisher Scientific Apreo) images were taken of Ni_2P films on carbon fiber. Powder X-ray diffraction (Bruker D8 Discover with Pilatus 100K 2D detector) was performed on as-synthesized Ni_2P nanoparticles on silicon wafers and the annealed Ni_2P-loaded 2×2 cm^2 carbon fiber squares.

3.3.3 *Electrochemical characterization*

For anodic polarization experiments, the working electrode was made in a standard N_2-atmosphere glovebox by cutting a 1×2 cm^2 strip from the center of the annealed Ni_2P-loaded carbon fiber squares. Then, copper wire was connected to one end of the strip using copper tape and covered with epoxy so that only a 1×1 cm^2 area of the carbon fiber remained exposed. Finally, a 0.5×1 cm^2 strip was cut from the end of the electrode so that all remaining exposed electrode was densely loaded with Ni_2P (Figure 3.1). Anodic polarization experiments were conducted inside an active N_2-purge glovebox. The electrolyte solution was sparged with Ar to remove dissolved O_2 for at least 1 h before being brought into the active purge glovebox. Then, the working electrode, in an enclosed container from the standard N_2-atmosphere glovebox, and

the sparged electrolyte solution were cycled into the active N_2-purge glovebox by purging the antechamber with N_2 for 1 h. Afterward, the working electrode, Ag/AgCl reference electrode calibrated to the H_2 redox couple (Bioanalytical Sys Inc.), and graphite rod counter electrode were immersed in the electrolyte solution. Open circuit potential was measured until stable to within 1 mV/h. Then, the working electrode was anodically polarized, beginning at the open circuit potential through 2 V vs. RHE at a rate of 0.1 mV/s and with a 90% ohmic drop correction. After each experiment, the cell was cleaned thoroughly with 18 MΩ water. Anodic polarization experiments were conducted using a potentiostat (Biologic SP-150).

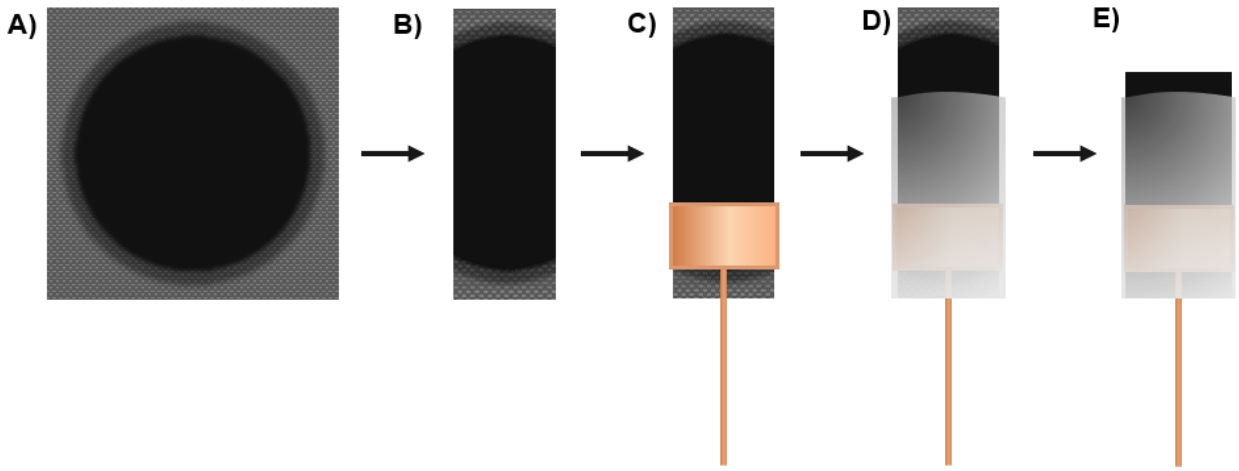

Figure 3.1. Schematic demonstrating the construction of electrodes beginning with (A) a 2×2 cm^2 square of carbon fiber with Ni_2P deposited on it. Next, (B) 0.5×2 cm^2 strips were cut from both sides. (C) We then connected a copper wire to the end of the center 1×2 cm^2 strip using copper tape. (D) Finally, we covered half the electrode in epoxy and (E) cut off a 0.5×1 cm^2 strip from the end to expose only a 0.5×1 cm^2 strip of saturated Ni_2P.

For *operando* X-ray absorption studies, inside an active N_2-purge glovebox to prevent O_2 exposure, a custom three-electrode *operando* cell (Figure 3.2) was filled with 1 M phosphate buffer, and then ports were plugged shut. This cell was 3-D printed and is a modification of the

general design of Singh et al.,[19] that moves the counter electrode and its associated electrolyte out of the beam path to decrease background absorption for transmission measurements; the low flux of laboratory XAS spectrometers greatly benefits from this consideration. The cell windows are 0.5-mm thick glassy carbon plates that are in mechanical contact with the working electrode and thus provide electrical feedthrough to it. The total electrolyte volume in the cell is ~ 3 ml.

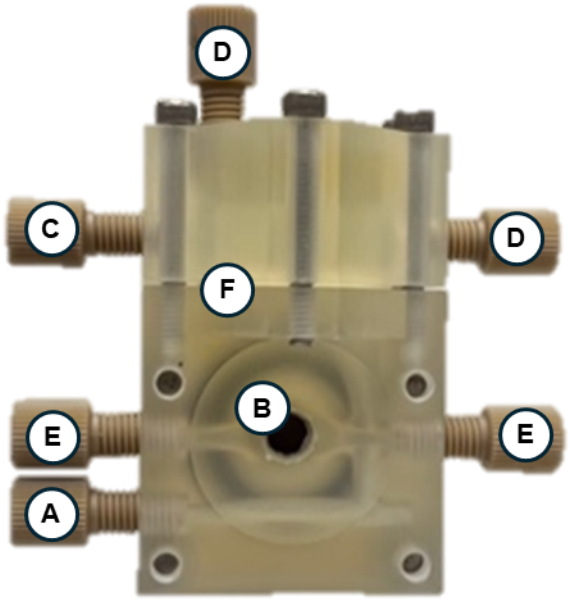

Figure 3.2. Image of the custom *operando* electrochemical cell used in Ni K-edge X-ray absorption spectroscopy experiments. (A) A leakless miniature Ag/AgCl reference electrode was inserted into the bottom of the cell with its end near the (B) glassy carbon window working electrode area. (C) Additionally, a graphite rod was used as the counter electrode on top of the cell. (D,E) Electrolyte solution could flow through the cell, and (F) a membrane can be placed between the working electrode/reference electrode and the counter electrode spaces; however, neither flow nor a membrane was used in this study.

The working electrode was made by cutting an approximately 1×1 cm^2 square from the center of the annealed Ni_2P-loaded 2×2 cm^2 carbon fiber squares. Electrochemical experiments were conducted using the resulting Ni_2P-loaded carbon fiber squares sandwiched between glassy

carbon windows (Sigradur). This sandwich served as the working electrode while leakless Ag/AgCl (eDAQ), which was calibrated to the H_2 redox couple, served as the reference electrode, and a graphite rod served as the counter electrode. Carbon fiber electrodes were dipped in electrolyte solution before placement inside the *operando* cell and stacked four layers thick to ensure good electrical contact through the glassy carbon windows. Chronoamperometry experiments were performed with this cell inside a benchtop spectrometer (easyXAFS 300). First, open circuit potential was measured using a potentiostat (Gamry Interface1000), then 0 V vs. RHE followed by 0.4 V vs. RHE were applied for 15 min and 30 min, respectively. Afterwards, 0.8 V vs. RHE was applied for 6 h, followed by 1.2 V for 6 h and 1.4 V for 6 h.

3.3.4 *X-ray absorption spectroscopy*

Operando transmission-mode Ni K-edge XAS was conducted using a commercial benchtop spectrometer (easyXAFS300+, from easyXAFS LLC), and all references were measured on the same instrument using an automated sample wheel. Additional XAS measurements of Ni_2P nanoparticles were measured *ex situ* in an air-free cell with the instrument of Gironda et al. (Figure 3.3C).[20]

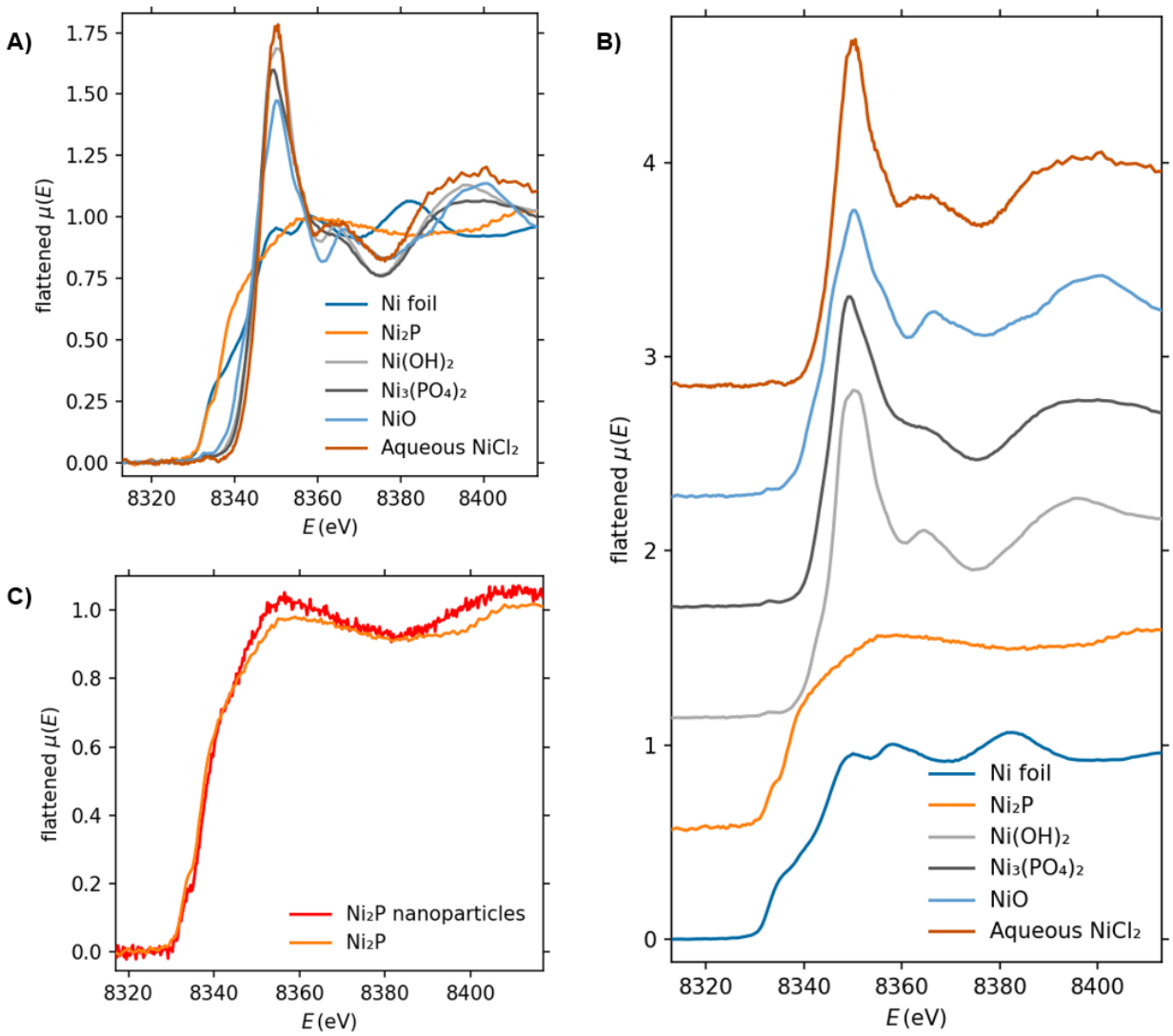

Figure 3.3. Ni K-edge X-ray absorption near-edge structure (XANES) in the easyXAFS 300 spectrometer of (A,B) Ni foil, bulk Ni_2P, $Ni(OH)_2$, $Ni_3(PO_4)_2$, NiO, and aqueous $NiCl_2$ which were used as components for linear combination analysis with the exception of Ni foil. (C) *Ex situ* Ni K-edge XANES of Ni_2P nanoparticles after annealing with the instrument of Gironda et al.[209] compared to bulk Ni_2P scans taken in the easyXAFS 300 spectrometer.

All analyses were performed using Larix inside the Larch program package. The spectrometer energy scales were calibrated to Ni foil at 8333 eV. Ni oxidation was estimated by linear combination fitting to Ni_2P, NiO, and $Ni_3(PO_4)_2$. A change in the exit slit location in the electrocatalysis experiment compared to the reference sample measurement was corrected with a

single energy shift across all electrocatalyst results. The energy shift was determined by first floating E_0 for the linear combination fit for the average of all scans at 0.8 V vs. RHE. After the energy shift was determined, we stopped floating E_0 to minimize degrees of freedom in the linear combination analysis. Linear combination fits were not forced to sum to unity. All sample scans were normalized before linear combination analysis.

3.4 Results and Discussion

3.4.1 *Nanoparticle synthesis and characterization*

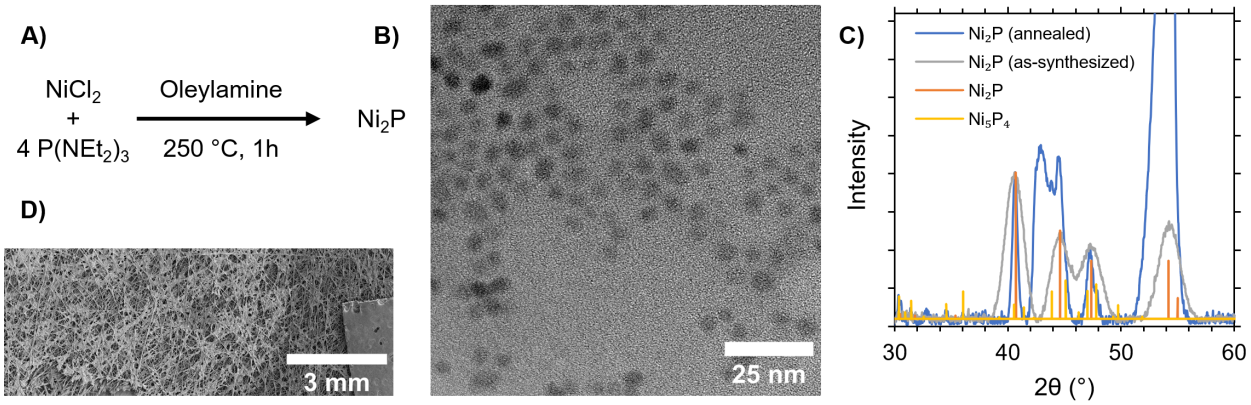

Figure 3.4. (A) Scheme of Ni_2P synthesis where 1 eq $NiCl_2$ and 4 eq tris(diethylamino)phosphine react in oleylamine at 250 °C to form Ni_2P nanoparticles. (B) TEM of Ni_2P nanoparticles after purification showing 4.3 +/- 0.8 nm spherical nanoparticles. (C) XRD of as-synthesized Ni_2P nanoparticles (gray) and annealed Ni_2P nanoparticles (blue) compared to Ni_2P (PDF 04-003-1863, orange) and Ni_5P_4 (PDF 04-014-7901, yellow). Peaks at 43° and 54° are due to the carbon fiber. (D) SEM of Ni_2P nanoparticles dispersed on carbon fiber.

We synthesized Ni_2P nanoparticles by degassing $NiCl_2$ in oleylamine at 120 °C for 1 h. We then allowed the solution to cool to 50 °C before injecting tris(diethylamino)phosphine and heating to 250 °C for 1 h (Figure 3.4A). Starting from 50 °C allows for the complete diffusion of P precursor throughout the solution before the Ni_2P nanoparticle nucleation temperature is reached, which promotes uniform nanoparticle growth and leads to low polydispersity. We then

purified the final solution through precipitation, centrifugation, and redissolution cycles in pentane (solvent) and isopropanol (antisolvent), followed by toluene (solvent) and acetonitrile (antisolvent). We will refer to the resulting purified Ni_2P nanoparticles as as-synthesized nanoparticles. We also annealed the Ni_2P nanoparticles at 450 °C for 2 h under a flow of 5% H_2/95% N_2 to remove ligands, reduce surface oxidation, and crystallize amorphous domains. Across two batches of nanoparticles, TEM images showed monodisperse spherical nanoparticles (Figure 3.4B, Figure 3.5A) with average diameters of 4.3 nm ± 0.8 nm (batch 1) and 3.2 nm ± 0.5 nm (batch 2).

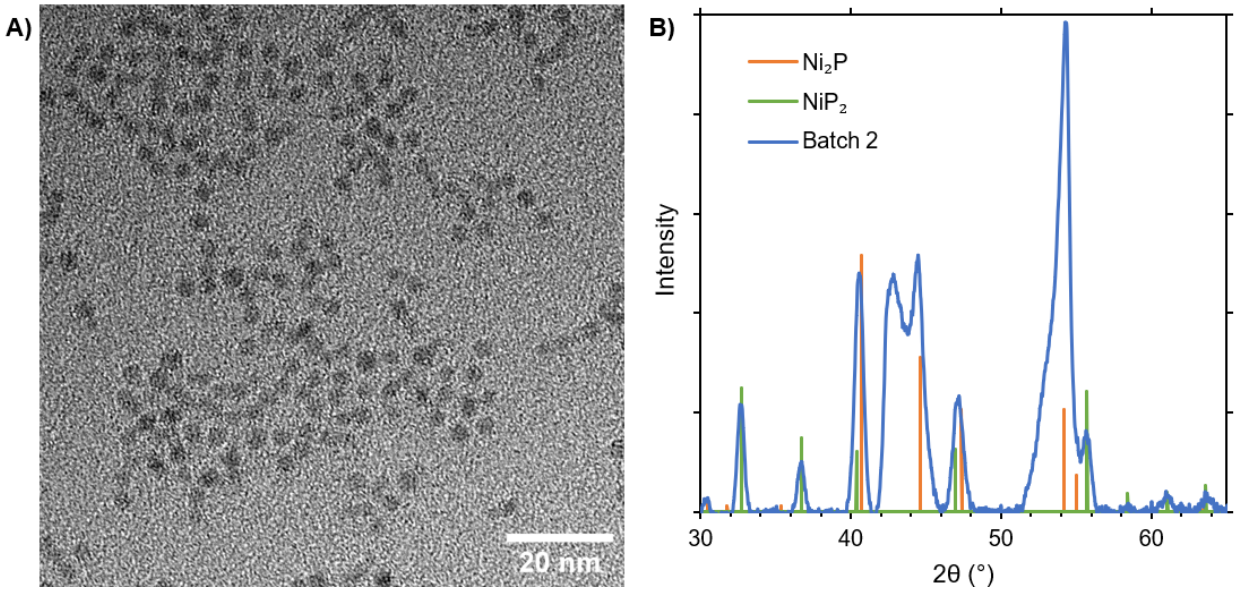

Figure 3.5. (A) After purification, TEM of the second batch of Ni_2P nanoparticles showed 3.2 nm ± 0.5 nm spherical nanoparticles. (B) XRD of the second batch of Ni_2P nanoparticles after annealing (blue) compared to Ni_2P (PDF 04-003-1863, orange) and NiP_2 (PDF 01-088-7141 with lattice constant shifted to a = 5.4671 Å, green). Peaks at 43° and 54° are due to the carbon fiber.

We also analyzed nanoparticles via powder X-ray diffraction (XRD) before and after annealing (Figure 3.4C, Figure 3.5B), and the resulting nanoparticle patterns matched well with indexed Ni_2P diffraction patterns (PDF 04-003-1863). However, after annealing, we saw minor

diffraction from NiP_2 (PDF 01-088-7141 with lattice constant shifted to a = 5.4671 Å) and Ni_5P_4 (PDF 04-014-7901). This result is likely due to excess P byproducts on the surface of the nanoparticles, leading to small amounts of P-rich nickel phosphide phases after annealing. Additionally, the diffraction peaks narrowed after annealing, indicating a growth in the nanoparticle size. Scherrer analysis performed on the diffraction peak at 40.6° indicated that the annealed nanoparticles had average crystallite domain sizes of 15 nm (batch 1) and 11 nm (batch 2). The crystallite domain size of the annealed nanoparticles was larger than the as-synthesized nanoparticle size determined by TEM due to the high loading of nanoparticles on carbon fiber. Specifically, we deposited approximately 2 mg/cm^2 of as-synthesized Ni_2P on carbon fiber (Figure 3.4D) to maximize signal-to-noise in the *operando* Ni K-edge X-ray absorption near edge structure (XANES) experiments.

3.4.2 *Anodic polarization of Ni_2P nanoparticles*

Using anodic polarization, wherein current is measured while slowly increasing the oxidation potential applied at the electrode, we can probe the corrosion kinetics of materials. We conducted experiments in a range of electrolyte pH environments (acidic, neutral, and basic) to investigate the corrosion of Ni_2P nanoparticles across the pH scale. In addition, a sufficiently slow scan rate was necessary to approximate the steady state of the material at each potential; therefore, we conducted all experiments at a scan rate of 0.1 mV/s. Polarization began at open circuit potential (OCP, otherwise referred to as corrosion potential, E_{corr}, i.e., where corrosion begins) and ended beyond the onset of oxygen evolution to cover the practical corrosion range of the material. To understand corrosion and passivation behavior, we can look at the OCP, peak potential(s), peak current density, and the following plateau in current. A lower peak potential generally shows that a material passivates at a lower potential, which is desirable because it minimizes the range of

potentials where the material actively corrodes. A lower peak current density is also desirable because it indicates a lower corrosion rate is necessary for passivation. When accounting for pH by calibrating the Ag/AgCl reference electrode to the H_2 redox couple, the OCP of Ni_2P nanoparticles landed at nearly identical potentials in acidic and neutral pH; however, OCP was higher in basic pH, which indicates that Ni_2P was more stable in basic pH than in lower pH electrolytes (Figure 3.6). The potentials at which peaks in current density occurred increased with pH: 0.7 V vs. RHE in acidic pH, 0.9 V and 1.2 V in neutral pH, and 1.1 V and 1.4 V in basic pH. Interestingly, only one peak appeared in the acidic pH trace, while two peaks appeared in the neutral and basic pH curves. We observed a plateau in current density indicative of passivation in the acidic and neutral pH curves but not in the basic pH curve. This result is likely due to the quick onset of OER after the second corrosion peak at basic pH. Acidic and neutral pH also resulted in similar maximum peak current densities (4.9 mA/cm^2 and 4.7 mA/cm^2, respectively). However, basic pH resulted in a significantly higher peak current density of 28 mA/cm^2. This result is attributable to NiOOH formation.[9,16] The final feature of interest in each anodic polarization scan is the onset of OER, otherwise called the transpassive regime, where the increase in current density is not due to corrosion but rather to water oxidation. OER began at a significantly lower potential in basic pH (1.6 V vs. RHE) than in the acidic (1.8 V) and neutral pHs (1.9 V), where OER occurred at similar potentials.

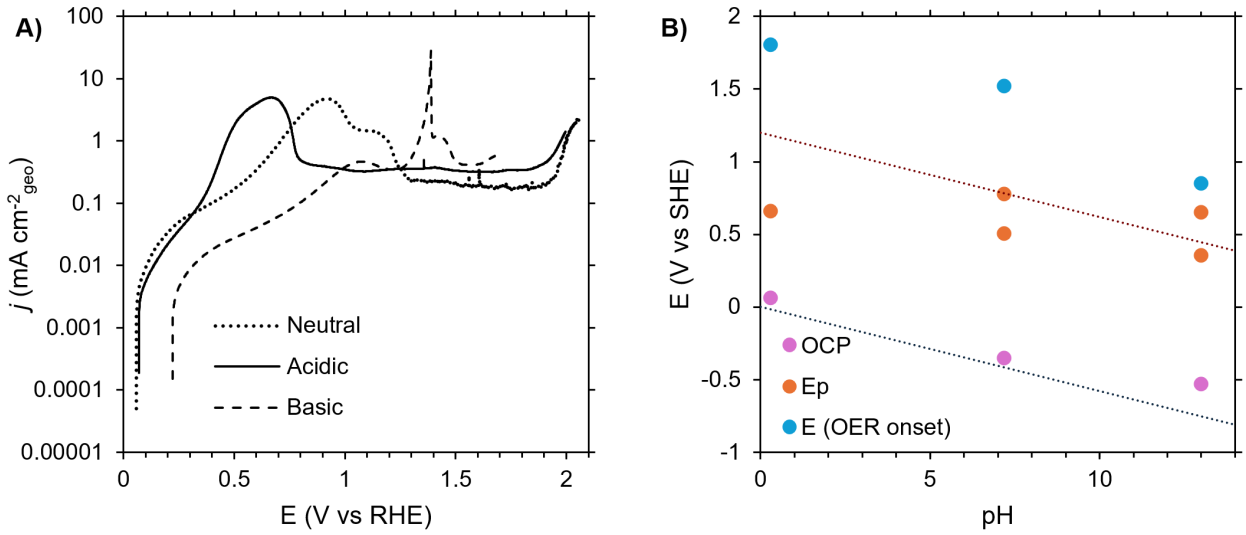

Figure 3.6. (A) Anodic polarization scans at 0.1 mV/s of Ni_2P nanoparticles in 0.5 M H_2SO_4, 1 M neutral K_2HPO_4:KH_2PO_4, and 0.1 M KOH. Current densities are normalized to the geometric surface area of the electrode with approximately 1 mg of Ni_2P on each electrode. (B) Comparison of Ni_2P anodic polarization results across pH and potentials vs SHE. Thermodynamic water reduction (blue dashed) and oxidation (red dashed) lines are shown as guides. OCP/E_{corr} was plotted for each electrode, along with peak potentials (E_p) and OER onset potential.

In comparing our anodic polarization results to prior literature reports, we note that Kucernak and Sundaram[13] used a 1 mV/s scan rate in their anodic polarization curves of Ni_2P as opposed to the 0.1 mV/s in our study. Due to its structural complexity and covalency,[4,18,21] it makes sense that Ni_2P reaches a steady state more slowly than conventional metals. Therefore, it is important to use slower scan rates to better understand the steady-state corrosion properties of Ni_2P and similarly complex materials. Our study showed a clear peak in current density at 0.4 V vs. RHE in 0.5 M H_2SO_4 (Figure 3.6A). Similarly, a very broad peak appears in multiple Ni_2P samples run by Kucernak and Sundaram; however, its broadness makes it difficult to distinguish without slower scan rates. Ni_2P particle size is another important distinction between our results and those of Kucernak and Sundaram. In their prior report, Kucernak and Sundaram used Ni_2P

particles that were multiple microns in diameter, but we used nanoparticles two orders of magnitude smaller. We chose to use smaller nanoparticles to get a stronger electrochemical response. As the size of a particle decreases, the surface-area-to-volume ratio increases; therefore, since surface atoms are more reactive and susceptible to oxidation than bulk atoms, it is easier to tell when distinct corrosion events occur in anodic polarization experiments.

Anodic polarization curves can also be related to Pourbaix diagrams (i.e., plots of electrochemical equilibria across pH and potential) to predict the stable products formed. Within the pH and potential scales used in our experiments, Muylder and Pourbaix predicted that aqueous phosphates are the most stable P species.[22] Deltombe, Zoubov, and Pourbaix predicted aqueous Ni^{2+} would be the most stable in acidic pH, while different Ni oxides would be most stable in neutral and basic pHs.[22] Huang et al. improved and simplified the Ni Pourbaix diagram; they predicted that NiO would be the dominant species between pH 5 to 16 and 0 V vs. RHE to 1.8 V vs. RHE.[23] In neutral and basic pH, they predicted the formation of NiOOH between 1.8 and 2.2 V vs RHE. Moreover, Wexler et al. predicted Ni_2P would have a narrow stability window below 0 V vs RHE.[24] They also predicted Ni_5P_4 would have a smaller stability window than Ni_2P. Therefore, we expected our samples to readily oxidize to $Ni^{2+/3+}$ and aqueous phosphates in most aqueous environments. With that in mind, we extrapolated the results from Figure 3.6A to make a quasi-Pourbaix diagram (Figure 3.6B) using the corrosion potentials (OCP), peak potentials, and OER onset potentials in acidic, neutral, and basic pH so that we can see the corrosion potentials and passivation potentials in each condition and compare to published Pourbaix diagrams. In one sense, E_{corr} was pinned near 0 V vs. RHE in all three of our pH conditions, indicating that Ni_2P is never stable in an aqueous environment. However, in our experiment, corrosion rates varied significantly across different applied potentials, meaning that

significant corrosion can occur rapidly or not at all, depending on the application. In acidic pH, the corrosion rates were higher and required less driving force than in neutral and basic pH (Figure 3.6). This was likely because, in acidic pH, Ni oxidation to Ni^{2+} occurs at a lower potential than at higher pH,[23] thereby increasing the driving force for oxidation at the lower applied potential. In our experiment, OCP and the first peak potential differed by 0.9 V vs. RHE in neutral and basic pH, similar to the difference between the predicted Ni^0/Ni^{2+} equilibrium potential at near 0 pH and the peak potential in our acidic pH curve.[23] If water reduction had not been a limiting factor, we would have expected the OCP of Ni_2P to be approximately -0.2 V vs RHE.

By comparing our anodic polarization curves to Pourbaix diagrams, we can predict the corrosion mechanisms of Ni_2P; however, Ni_2P differs from pure Ni and pure P just as Ni and P differ in bonding and structure. Therefore, we sought to use Ni K-edge X-ray absorption spectroscopy to better understand the corrosion mechanism of Ni_2P in neutral pH. The electrochemical response of Ni_2P in neutral pH has been far less studied than in acidic and basic pH, but the anodic polarization curve in neutral pH shares similarities with curves in both acidic and basic pH such that we can attempt to extrapolate the speciation information gleaned from neutral pH to other pH conditions.

3.4.3 *Operando XANES of Ni_2P nanoparticle corrosion in neutral phosphate buffer*

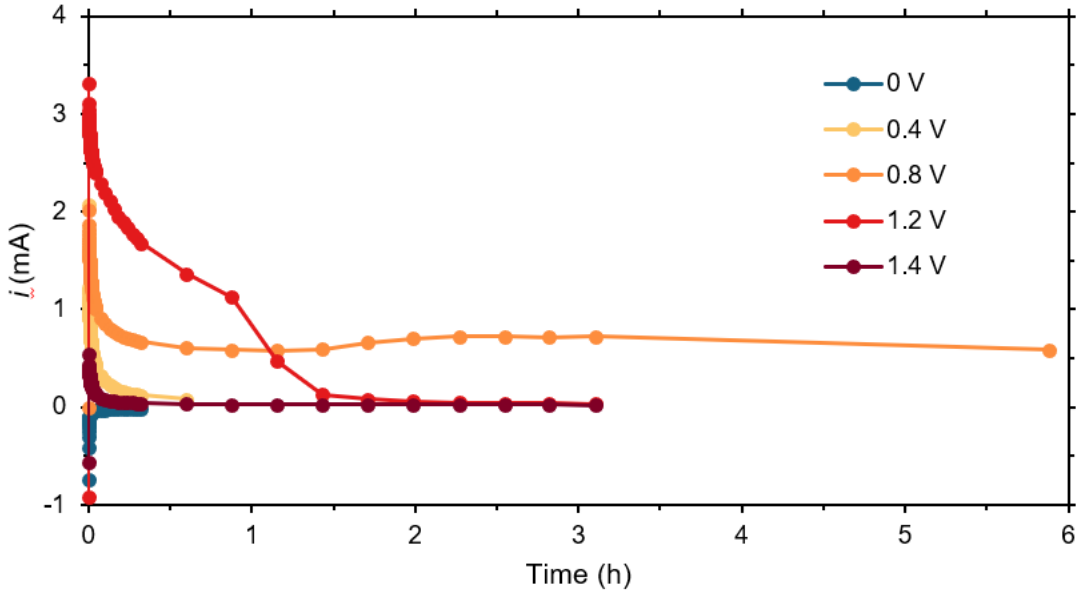

Figure 3.7. Chronoamperometry scans were conducted *in operando* at 0 V, 0.4 V, 0.8 V, 1.2 V, and 1.4 V vs. RHE with a 90% ohmic drop correction.

We explored the speciation of Ni_2P at various applied potentials to understand its corrosion at neutral pH. Operando experiments were enabled using a custom-designed electrochemical cell modeled after Singh et al..[19] To overcome the photon flux limitations from benchtop instruments, we moved the reference and counter electrodes out of the X-ray beam path and minimized the space between glassy carbon windows to optimize our experiments for transmission-mode measurements. After we loaded Ni_2P electrodes into the operando electrochemical cell in an inert atmosphere, we left the sample to soak overnight before conducting electrochemical and X-ray absorption experiments to allow the Ni_2P nanoparticles to reach a steady state. After soaking, OCP was 63 mV vs. RHE. After a 15 min scan at OCP, we applied 0 V vs. RHE for 15 min; however, we observed little current, indicating little to no reduction in the Ni oxidation state. Similarly, we observed little oxidation current after 30 min at 0.4 V vs. RHE, indicating slow and small amounts of oxidation (Figure 3.7). Next, we increased the applied potential to 0.8 V vs.

RHE for 6 h. Significant oxidation current appeared in conjunction with a growing white line (i.e., peak at the absorption edge) (Figure 3.8) and increasing E_0 (Figure 3.9A). After 6 h at 0.8 V, we increased the applied potential to 1.2 V vs. RHE and saw complete oxidation to Ni^{2+}. Ni^{2+} remained the exclusive species for an additional 6 h at 1.4 V vs. RHE (Figure 3.9).

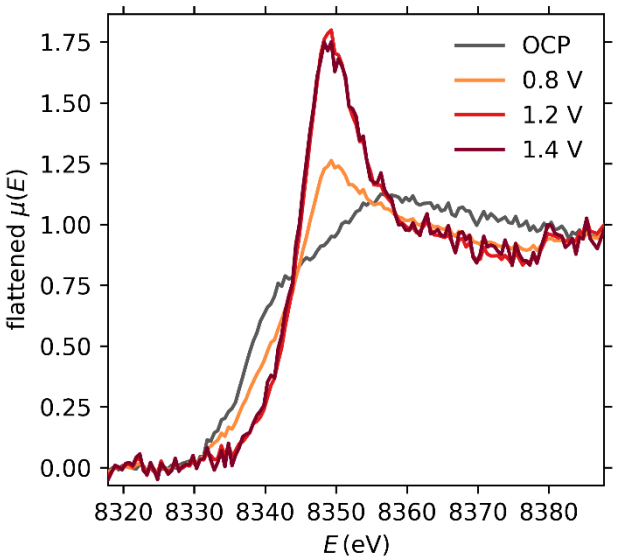

Figure 3.8. Normalized Ni K-edge X-ray absorption spectra of Ni_2P nanoparticles in 1 M neutral phosphate buffer at OCP, 0.8 V, 1.2 V, and 1.4 V vs. RHE averaged over 15 min, 6 h, 6 h, and 6 h, respectively.

Additionally, throughout the experiment, the edge step (the jump in absorption at the Ni K-edge, which is proportional to the thickness of material in the path of the X-ray beam) decreased by 80% (Figure 3.9A). This decrease indicates Ni_2P dissolution and diffusion out of the X-ray beam path. After the first 6 h of applied potential, the edge step had dropped by approximately 40%, leaving a maximum of 60% of the electrocatalyst remaining on the electrode. Once we applied 1.2 V to the sample, the edge step dropped at approximately 21% per h (compared to a rate of 7% per h at 0.8 V) before reaching a plateau of 0.6% per h. Recalling the anodic polarization curves (Figure 3.6A), we can consider increasing the applied potential as

increasing the driving force for corrosion and the increased driving force as causing the formation of a passive barrier film through rapid surface oxidation. The barrier film's formation is indicated by the plateaus of the edge step and current density. In other words, the corrosion rate was significantly reduced after the barrier film formed. Unsurprisingly, increasing the driving force to 1.4 V did not change the edge step significantly. This result supports the passivation hypothesis.

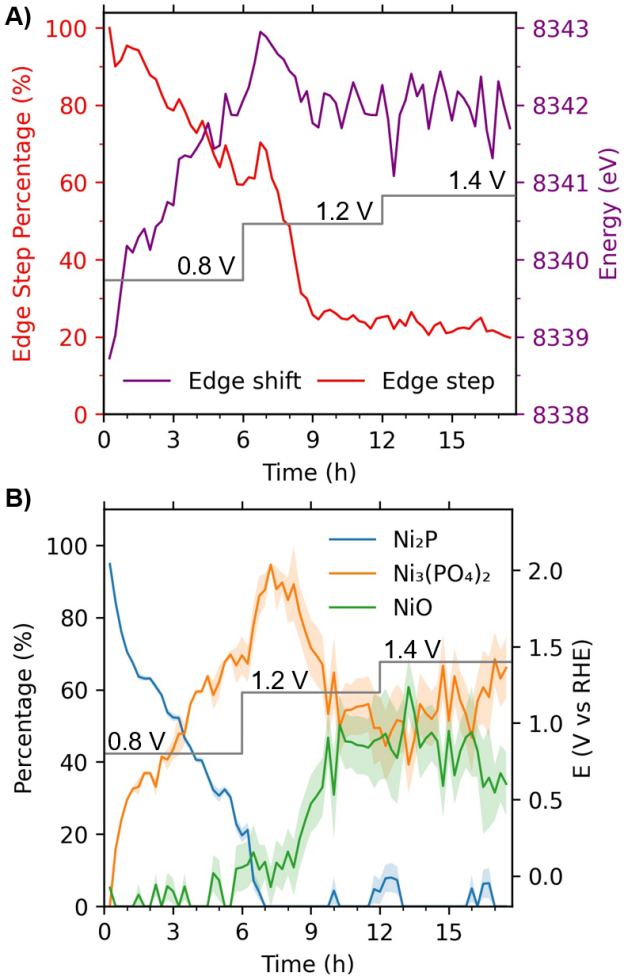

Figure 3.9. (A) Time evolution of the edge step and E_0 (E at the halfway point of the edge) with an overlay indicating applied potential (V vs. RHE). (B) Ni speciation over time was determined through linear combination analysis for each scan (15 min) with an overlay indicating applied potential (V vs. RHE). The shaded bands indicate standard error for each fit component.

This understanding of passivation as resulting from rapid corrosion is also consistent with differences between how Ni_2P responds to polarization in sulfuric acid vs a neutral phosphate buffer. Ni_2P reacts more quickly (given the same amount of applied potential, i.e., driving force) in sulfuric acid than in a neutral phosphate buffer. Counterintuitively, faster corrosion rates at a lower applied potential are more optimal than slower corrosion rates at a higher applied potential when considering our overall goal of reducing the time Ni_2P is vulnerable to corrosion.

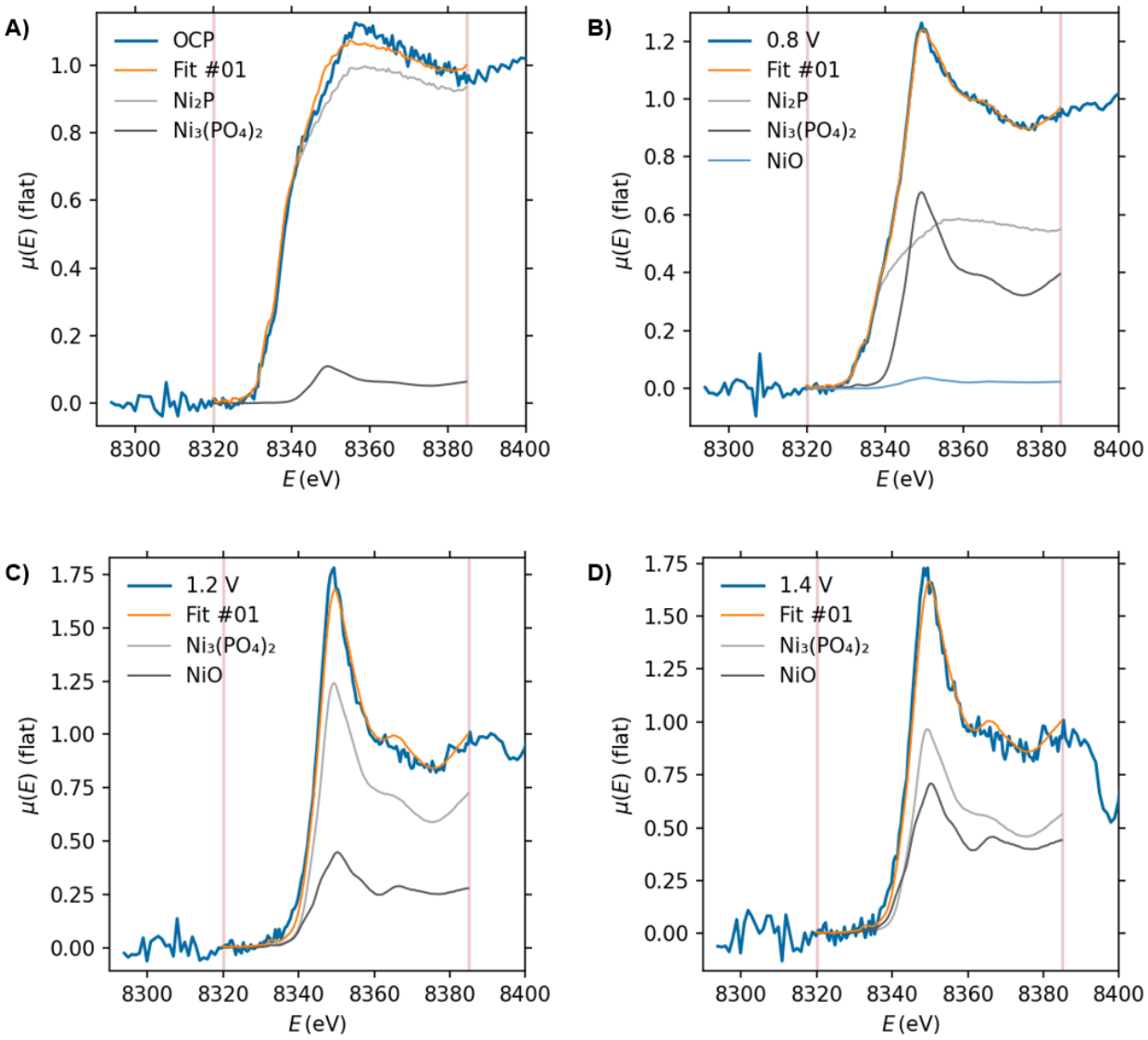

Figure 3.10. Linear combination analysis fits of Ni K-edge XANES averaged from all scans at (A) open circuit potential, (B) 0.8 V, (C) 1.2 V, and (D) 1.4 V vs. RHE. Bulk Ni_2P, $Ni(OH)_2$, $Ni_3(PO_4)_2$, NiO, and aqueous $NiCl_2$ were all used as components in the analysis; however, only Ni_2P, $Ni_3(PO_4)_2$, and NiO were found to be significant components in the spectra.

To see the evolution of the oxidation state over time, we performed linear combination fitting for each scan (Figure 3.9B, Figure 3.10). We used bulk Ni_2P, $Ni_3(PO_4)_2$, and NiO reference spectra as components in the linear combination analysis (Figure 3.3). Over the time that 0.8 V vs. RHE was applied, Ni_2P converted to $Ni_3(PO_4)_2$. As we applied 1.2 V vs. RHE, Ni_2P reached 0%, NiO grew, and $Ni_3(PO_4)_2$ decreased. Both $Ni_3(PO_4)_2$ and NiO stabilized at

approximately 50% through hours 9 to 15 of the experiment, then NiO began to decrease while $Ni_3(PO_4)_2$ increased. Additionally, more noise appeared in the linear combination analysis at 1.2 and 1.4 V due to dissolution into the electrolyte reservoir outside the beam path, based on the smaller edge step indicating less Ni was present in the beam, which decreased the signal-to-noise ratio. We note that applying 1.2 V vs. RHE coincides with a decrease in current in the anodic polarization curves; the decrease in current is associated with the onset of passivation (Figure 3.6A). These results indicate that P-containing Ni species 1) oxidize first and 2) mostly dissolve away as excess Ni is oxidized to NiO. Further, NiO coats the surface of the nanoparticle film to passivate against corrosion. One might wonder whether the material further oxidized to $Ni^{3+/4+}$; however, E_0 remained consistent after complete oxidation and matched closely with the E_0 of $Ni_3(PO_4)_2$ and NiO. Therefore, it is unlikely that oxidation from Ni^{2+} to higher oxidation states occurred.

3.4.4 *Impact on the use of Ni_2P electrocatalysts*

This study showed that Ni_2P was susceptible to corrosion close to 0 V vs. RHE; therefore, oxidation is likely any time the catalyst sits at or is polarized to potentials beyond this point. Yet, the catalyst can still be protected from further corrosion by passivating the surface. Importantly, however, the new passivated surface is distinct from the pristine Ni_2P surface and is now the catalytically relevant interface for reactions beyond 0 V vs. RHE. Ni_2P itself, therefore, is not an ideal candidate for catalyzing oxidation reactions at positive potentials vs. RHE. However, Ni_2P is a promising precatalyst or catalyst support for various oxidation reactions, e.g., OER, urea oxidation, ammonia oxidation, and benzyl alcohol oxidation.[8,9,25–28]

Additionally, it is important to understand how Ni_2P reacts in different pH conditions. We saw a smaller window for active corrosion (i.e., the difference between OCP and passivation

potential) in acidic pH than in higher pH electrolytes. Additionally, OER occurred at a lower applied potential in basic pH than in lower pH electrolytes. These findings inform the conditions ideal for avoiding significant corrosion in electrocatalytic reactions involving Ni_2P. Additionally, these findings help define techniques for intentionally oxidizing and passivating the surface of Ni_2P. Previous work demonstrated the oxidation mechanism of Ni_2P in air (where Ni_2P also oxidizes through a phosphate pathway).[29] Combined with the current work, this research illuminates the stability of Ni_2P and helps scientists mitigate corrosion, accurately predict surface reactivity, and prepare Ni_2P for industrial electrocatalysis.

3.5 Conclusions

In conclusion, Ni_2P nanoparticles are susceptible to corrosion in aqueous environments at any pH; however, passivation enables Ni_2P nanoparticles to be used as precatalysts for a variety of oxidation reactions. In a neutral phosphate-buffered electrolyte solution, Ni_2P nanoparticles are oxidized via a phosphate pathway. Then, when these particles are pushed beyond the passivation potential, excess Ni oxidizes rapidly to form an oxidized Ni passivation layer. By understanding the degradation mechanism of Ni_2P, we can rationally design techniques for preventing significant oxidation and leveraging intentional anodization. For example, selectively ligating P on the surface of Ni_2P nanoparticles has the potential to protect against corrosion while leaving Ni sites available for reaction.[18] Additionally, this study highlights the importance of measuring the corrosion of nanoparticles over measuring bulk materials when possible due to the increased susceptibility of nanoparticles to corrosion owing to the significantly greater surface-to-bulk atom ratio. This vulnerability in nanoparticles is also what makes them ideal candidates for catalysis while also making them better subjects for study through bulk-sensitive techniques such as XAS. Finally, through the degradation mechanism of Ni_2P nanoparticles, we get a clearer

picture of what actual surface active sites will look like at different applied potentials, enabling more robust predictions of catalytic activity. The availability of laboratory-based XAFS and the optimization of electrochemical cells for their lower flux were critical enablers of the present work and can impact future studies of catalyst corrosion.

3.6 REFERENCES

(1) Rivera-Maldonado, R.; Gironda, A.; Varughese, A.; Kuo, D.-Y.; Nguyen, H.; Dean-Hill, D.; Abramson, J.; Seidler, G.; Cossairt, B. Probing the Stability of Ni2P Nanoparticle Electrocatalysts via Operando Benchtop X-Ray Absorption Spectroscopy. ChemRxiv October 21, 2024. https://doi.org/10.26434/chemrxiv-2024-j05h7.

(2) Bando, K. K.; Wada, T.; Miyamoto, T.; Miyazaki, K.; Takakusagi, S.; Koike, Y.; Inada, Y.; Nomura, M.; Yamaguchi, A.; Gott, T.; Ted Oyama, S.; Asakura, K. Combined in Situ QXAFS and FTIR Analysis of a Ni Phosphide Catalyst under Hydrodesulfurization Conditions. *J. Catal.* **2012**, *286*, 165–171. https://doi.org/10.1016/j.jcat.2011.10.025.

(3) Layan Savithra, G. H.; Muthuswamy, E.; Bowker, R. H.; Carrillo, B. A.; Bussell, M. E.; Brock, S. L. Rational Design of Nickel Phosphide Hydrodesulfurization Catalysts: Controlling Particle Size and Preventing Sintering. *Chem. Mater.* **2013**, *25* (6), 825–833. https://doi.org/10.1021/cm302680j.

(4) Liu, P.; Rodriguez, J. A. Catalysts for Hydrogen Evolution from the [NiFe] Hydrogenase to the Ni2P(001) Surface: The Importance of Ensemble Effect. *J. Am. Chem. Soc.* **2005**, *127* (42), 14871–14878. https://doi.org/10.1021/ja0540019.

(5) Popczun, E. J.; McKone, J. R.; Read, C. G.; Biacchi, A. J.; Wiltrout, A. M.; Lewis, N. S.; Schaak, R. E. Nanostructured Nickel Phosphide as an Electrocatalyst for the Hydrogen Evolution Reaction. *J. Am. Chem. Soc.* **2013**, *135* (25), 9267–9270. https://doi.org/10.1021/ja403440e.

(6) Nishiwaki, E.; Rice, P. S.; Kuo, D.-Y.; Dou, F. Y.; Pyka, A.; Reid, B.; Nguyen, H. A.; Stuve, E. M.; Raugei, S.; Cossairt, B. M. Ni2P Active Site Ensembles Tune Electrocatalytic Nitrate Reduction Selectivity. *Chem. Commun.* **2024**. https://doi.org/10.1039/D4CC01834F.

(7) D. Calvinho, K. U.; B. Laursen, A.; K. Yap, K. M.; A. Goetjen, T.; Hwang, S.; Murali, N.; Mejia-Sosa, B.; Lubarski, A.; M. Teeluck, K.; S. Hall, E.; Garfunkel, E.; Greenblatt, M.; Charles Dismukes, G. Selective CO 2 Reduction to C 3 and C 4 Oxyhydrocarbons on Nickel Phosphides at Overpotentials as Low as 10 mV. *Energy Environ. Sci.* **2018**, *11* (9), 2550–2559. https://doi.org/10.1039/C8EE00936H.

(8) Dutta, A.; Pradhan, N. Developments of Metal Phosphides as Efficient OER Precatalysts. *J. Phys. Chem. Lett.* **2017**, *8* (1), 144–152. https://doi.org/10.1021/acs.jpclett.6b02249.

(9) Liu, P. F.; Li, X.; Yang, S.; Zu, M. Y.; Liu, P.; Zhang, B.; Zheng, L. R.; Zhao, H.; Yang, H. G. Ni2P(O)/Fe2P(O) Interface Can Boost Oxygen Evolution Electrocatalysis. *ACS Energy Lett.* **2017**, *2* (10), 2257–2263. https://doi.org/10.1021/acsenergylett.7b00638.

(10) Kuo, D.-Y.; Nishiwaki, E.; Rivera-Maldonado, R. A.; Cossairt, B. M. The Role of Hydrogen Adsorption Site Diversity in Catalysis on Transition-Metal Phosphide Surfaces. *ACS Catal.* **2022**, 287–295. https://doi.org/10.1021/acscatal.2c04936.
(11) Seh, Z. W.; Kibsgaard, J.; Dickens, C. F.; Chorkendorff, I.; Nørskov, J. K.; Jaramillo, T. F. Combining Theory and Experiment in Electrocatalysis: Insights into Materials Design. *Science* **2017**, *355* (6321), eaad4998. https://doi.org/10.1126/science.aad4998.
(12) Parra-Puerto, A.; Ng, K. L.; Fahy, K.; Goode, A. E.; Ryan, M. P.; Kucernak, A. Supported Transition Metal Phosphides: Activity Survey for HER, ORR, OER, and Corrosion Resistance in Acid and Alkaline Electrolytes. *ACS Catal.* **2019**, 11515–11529. https://doi.org/10.1021/acscatal.9b03359.
(13) J. Kucernak, A. R.; Sundaram, V. N. N. Nickel Phosphide: The Effect of Phosphorus Content on Hydrogen Evolution Activity and Corrosion Resistance in Acidic Medium. *J. Mater. Chem. A* **2014**, *2* (41), 17435–17445. https://doi.org/10.1039/C4TA03468F.
(14) Elsener, B.; Crobu, M.; Scorciapino, M. A.; Rossi, A. Electroless Deposited Ni–P Alloys: Corrosion Resistance Mechanism. *J. Appl. Electrochem.* **2008**, *38* (7), 1053–1060. https://doi.org/10.1007/s10800-008-9573-8.
(15) Crobu, M.; Scorciapino, A.; Elsener, B.; Rossi, A. The Corrosion Resistance of Electroless Deposited Nano-Crystalline Ni–P Alloys. *Electrochimica Acta* **2008**, *53* (8), 3364–3370. https://doi.org/10.1016/j.electacta.2007.11.071.
(16) Menezes, P. W.; Indra, A.; Das, C.; Walter, C.; Göbel, C.; Gutkin, V.; Schmeiβer, D.; Driess, M. Uncovering the Nature of Active Species of Nickel Phosphide Catalysts in High-Performance Electrochemical Overall Water Splitting. *ACS Catal.* **2017**, *7* (1), 103–109. https://doi.org/10.1021/acscatal.6b02666.
(17) Madadkhani, S.; Nandy, S.; Chae, K. H.; Aleshkevych, P.; Najafpour, M. M. Unveiling the Changes of Dinickel Phosphide (Ni2P) in Hydrogen Evolution Reaction: Toward a Deeper Mechanistic Understanding. *ACS Appl. Energy Mater.* **2024**. https://doi.org/10.1021/acsaem.3c03145.
(18) Murphy, I. A.; Rice, P. S.; Monahan, M.; Zasada, L. B.; Miller, E. M.; Raugei, S.; Cossairt, B. M. Covalent Functionalization of Nickel Phosphide Nanocrystals with Aryl-Diazonium Salts. *Chem. Mater.* **2021**, *33* (24), 9652–9665. https://doi.org/10.1021/acs.chemmater.1c03255.
(19) Singh, N.; Nguyen, M.-T.; Cantu, D. C.; Mehdi, B. L.; Browning, N. D.; Fulton, J. L.; Zheng, J.; Balasubramanian, M.; Gutiérrez, O. Y.; Glezakou, V.-A.; Rousseau, R.; Govind, N.; Camaioni, D. M.; Campbell, C. T.; Lercher, J. A. Carbon-Supported Pt during Aqueous Phenol Hydrogenation with and without Applied Electrical Potential: X-Ray Absorption and Theoretical Studies of Structure and Adsorbates. *J. Catal.* **2018**, *368*, 8–19. https://doi.org/10.1016/j.jcat.2018.09.021.
(20) Gironda, A. J.; Abramson, J. E.; Chen, Y.; Solovyev, M.; Sterbinsky, G. E.; Seidler, G. T. Asymmetric Rowland Circle Geometries for Spherically Bent Crystal Analyzers in Laboratory and Synchrotron Applications. *J. Anal. At. Spectrom.* **2024**, *39* (5), 1375–1387. https://doi.org/10.1039/D3JA00437F.
(21) Carenco, S.; Liu, Z.; Salmeron, M. The Birth of Nickel Phosphide Catalysts: Monitoring Phosphorus Insertion into Nickel. *ChemCatChem* **2017**, *9* (12), 2318–2323. https://doi.org/10.1002/cctc.201601526.
(22) Pourbaix, M. *Atlas of Electrochemical Equilibria in Aqueous Solutions*, 2d English ed.; National Association of Corrosion Engineers: Houston, Tex, 1974.

(23) Huang, L.-F.; Hutchison, M. J.; Santucci, R. J. Jr.; Scully, J. R.; Rondinelli, J. M. Improved Electrochemical Phase Diagrams from Theory and Experiment: The Ni–Water System and Its Complex Compounds. *J. Phys. Chem. C* **2017**, *121* (18), 9782–9789. https://doi.org/10.1021/acs.jpcc.7b02771.

(24) Wexler, R. B.; Martirez, J. M. P.; Rappe, A. M. Active Role of Phosphorus in the Hydrogen Evolving Activity of Nickel Phosphide (0001) Surfaces. *ACS Catal.* **2017**, *7* (11), 7718–7725. https://doi.org/10.1021/acscatal.7b02761.

(25) Xu, K.; Cheng, H.; Liu, L.; Lv, H.; Wu, X.; Wu, C.; Xie, Y. Promoting Active Species Generation by Electrochemical Activation in Alkaline Media for Efficient Electrocatalytic Oxygen Evolution in Neutral Media. *Nano Lett.* **2017**, *17* (1), 578–583. https://doi.org/10.1021/acs.nanolett.6b04732.

(26) Liu, H.; Zhu, S.; Cui, Z.; Li, Z.; Wu, S.; Liang, Y. Ni 2 P Nanoflakes for the High-Performing Urea Oxidation Reaction: Linking Active Sites to a UOR Mechanism. *Nanoscale* **2021**, *13* (3), 1759–1769. https://doi.org/10.1039/D0NR08025J.

(27) Li, F.; Liu, C.; Lin, H.; Sun, Y.; Yu, H.; Xue, S.; Cao, J.; Jia, X.; Chen, S. High Activity of Bifunctional Ni2P Electrocatalyst for Benzyl Alcohol Oxidation Coupled with Hydrogen Evolution. *J. Colloid Interface Sci.* **2023**, *640*, 329–337. https://doi.org/10.1016/j.jcis.2023.02.121.

(28) Jo, C.; Surendran, S.; Kim, M.-C.; An, T.-Y.; Lim, Y.; Choi, H.; Janani, G.; Cyril Jesudass, S.; Jun Moon, D.; Kim, J.; Young Kim, J.; Hyuck Choi, C.; Kim, M.; Kyu Kim, J.; Sim, U. Meticulous Integration of N and C Active Sites in Ni2P Electrocatalyst for Sustainable Ammonia Oxidation and Efficient Hydrogen Production. *Chem. Eng. J.* **2023**, *463*, 142314. https://doi.org/10.1016/j.cej.2023.142314.

(29) Abramson, J. E.; Holden, W. M.; Rivera-Maldonado, R. A.; Velian, A.; Cossairt, B. M.; Seidler, G. T. A Laboratory X-Ray Emission Spectrometer for Phosphorus Kα and Kβ Study of Air-Sensitive Samples. *J. Anal. At. Spectrom.* **2023**. https://doi.org/10.1039/D3JA00053B.

Chapter 4. METHODS DEVELOPMENT

Operando cell designed and optimized in collaboration with D.-Y. Kuo, D. Dean-Hill, J. E. Abramson, and G. T. Seidler. X-ray spectroscopy experiments were conducted in collaboration with J. E. Abramson, A. Gironda, S. Tetef, D. Dhakal, and G. T. Seidler. Electrochemistry experiments were carried out in collaboration with D.-Y. Kuo. Scanning electron microscopy was carried out in collaboration with S. Braswell. Air-free sample holders designed in collaboration with J. E. Abramson.

4.1 Three-electrode Cell for Benchtop *Operando* Transmission-mode X-ray Absorption Spectroscopy

Through *operando* measurements of catalysts, we can better understand structure-activity relationships, improve existing catalysts, and identify novel, high-performing catalysts. To better understand Ni-based catalysts and incorporate *operando* spectroscopy more routinely, we sought to create an electrochemical cell for *operando* X-ray absorption spectroscopy (XAS) using benchtop spectrometers, which are more readily accessible than synchrotron beamlines. Because benchtop spectrometers are photon flux-limited, *operando* XAS requires high catalyst loading, minimal bubbles on the catalyst's surface, and minimal attenuation from non-sample materials. High catalyst loading is necessary for optimal signal-to-noise in transmission-mode X-ray absorption spectra. Uniform absorption of X-rays is also required, but bubbles disrupt that uniformity. We modified the cell design in Singh et al.[1] to minimize attenuation from non-sample materials by moving the reference and counter electrodes out of the path of the X-ray beam and minimizing the space between the glassy carbon windows.

Next, we worked to identify optimal preparational and operational parameters that would allow for high catalyst loading and minimize bubble effects. We decided to use carbon fiber paper as the working electrode substrate to get thick, uniform films of catalysts while minimizing X-ray absorption from electrode materials, as demonstrated in previous *in situ* XAS studies.[2–5] Carbon

fiber is an optimal choice due to its low density and high porosity and because of carbon's inherently low X-ray absorption at the Ni K-edge. To maximize signal-to-noise for transmission-mode XAS, we calculated how much Ni_2P catalyst was necessary for absorbing approximately 1/3 of X-ray photons. An amount of 16 mg of Ni_2P was calculated using the photoelectric cross-sections, atomic weights, and atomic ratios of Ni and P around the Ni K-edge (8333 eV) and empirical factors from ex-situ experiments.

We developed an optimized procedure for depositing a uniform film of Ni_2P on the carbon fiber substrate. We compared Ni_2P solutions in a high boiling point solvent (toluene, Figure 4.1A) and a low boiling point solvent (dichloromethane, Figure 4.1B). From scanning electron microscopy (SEM) images, it became evident that the toluene solution deposited a film, while the dichloromethane solution left behind an uneven powder. When drop casting, others saw that slower evaporation rates led to more uniform, ordered film deposits.[6–8] This phenomenon occurs because solute particles have time to redisperse in the solvent droplet and order themselves more evenly in lower vapor pressure solvents. Therefore, we determined that high boiling point solvents like toluene are better for uniform deposition. However, when drop casting on 1×1 cm^2 carbon fiber squares, the solution was visibly wicked to the edges of the square, leaving little Ni_2P in the center where the X-ray beam is directed (Figure 4.1C). To confirm this wicking effect, we took *ex situ* XAS measurements with the X-ray beam focused through both the edges of the square and the center and confirmed there was higher signal-to-noise with the X-ray beam going through the edges of the square (Figure 4.1D). To circumvent the wicking effect, we increased the size of the carbon fiber substrates to 2×2 cm^2 squares and adjusted the drop volume during drop casting. This procedure resulted in films in the center of the square with diameters of 24 mm for 20 μL drops and 19 mm for 10 μL drops (Figure 4.1E,F). Drop casting 20 μL at a time resulted in films that

still reached the edges of the substrate; therefore, a maximum of 10 μL drops of toluene solution should be used for drop casting on 2×2 cm^2 squares of carbon fiber substrate. A final change to the procedure was to use a syringe pump to deposit a solution at a rate of 5 μL/min (Figure 4.1G). This final change in the procedure resulted in increased consistency between films and increased efficiency of drop casting. After drop casting, we cut out a 1×1 cm^2 square from the center of the substrate for use in the *operando* cell.

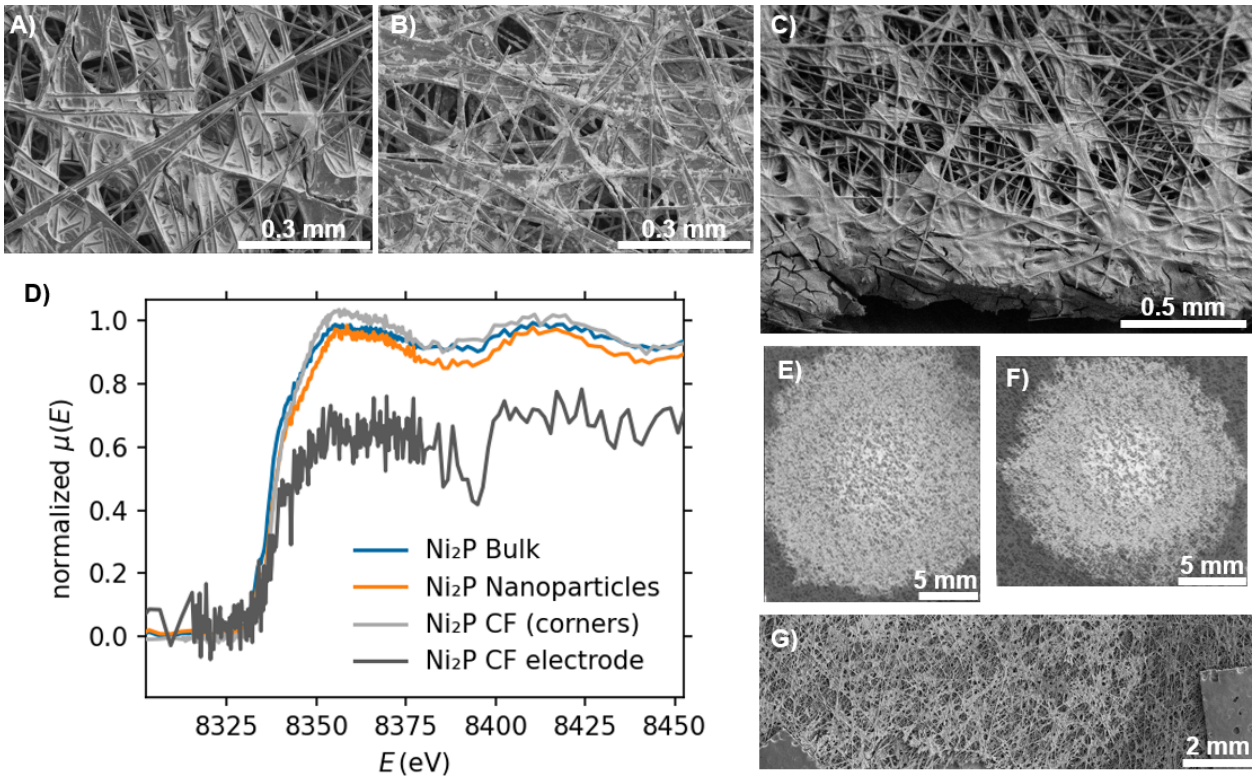

Figure 4.1. SEM images of Ni_2P nanoparticles drop cast on carbon fiber paper from (A) solution in toluene and (B) dichloromethane. (C) SEM image of the edge of the 1×1 cm^2 square after drop casting from toluene. (D) Normalized Ni K-edge X-ray absorption spectra of bulk Ni_2P (blue) and Ni_2P nanoparticle powder (red) mixed with hexagonal boron nitride. The Ni_2P powders were compared to the center (purple) and corners (green) of a 1×1 cm^2 carbon fiber square deposited with Ni_2P nanoparticles. SEM image of Ni_2P nanoparticles drop cast from toluene on 2×2 cm^2 squares of carbon fiber with (E) 20 µL drops and (F) 10 µL drops from a micropipette. (G) SEM image of Ni_2P nanoparticles drop cast from toluene via syringe pump at a rate of 5 µL/min onto a 2×2 cm^2 square of carbon fiber held by tweezers.

Before experiments in the *operando* cell, we determined the maximum amount of Ni_2P that could be deposited on each square. Depositing too thick films could lead to Ni_2P nanoparticles that do not make good electrical contact with the electrode. All deposited Ni_2P must come in electrical contact with the carbon fiber because inactive Ni_2P would make small changes in chemical structure more difficult to discern in flux-limited benchtop spectrometers. For this same reason,

we used Ni_2P nanoparticles instead of bulk particles to maximize the surface-to-bulk atom ratio for a bulk-sensitive technique like XAS, which probes all Ni atoms in the sample. To deduce the optimal Ni_2P loading on 2×2 cm^2 square electrodes, we measured capacitive current at open circuit potential (OCP) during cyclic voltammetry (CV) experiments across five Ni_2P loadings (1, 2, 3, 4, and 5 mg; Figure 4.2A). Increasing the amount of Ni_2P on the electrode should result in a linear increase in capacitive current. When increasing the loading of Ni_2P onto the electrode results in sub-linear increases in capacitive current, we can infer that a smaller portion of the Ni_2P added is in electrical contact with the electrode. For 1 through 4 mg depositions, capacitive current increased linearly; however, at 5 mg, capacitive current did not increase linearly but dropped to a similar level as measured at 3 mg.

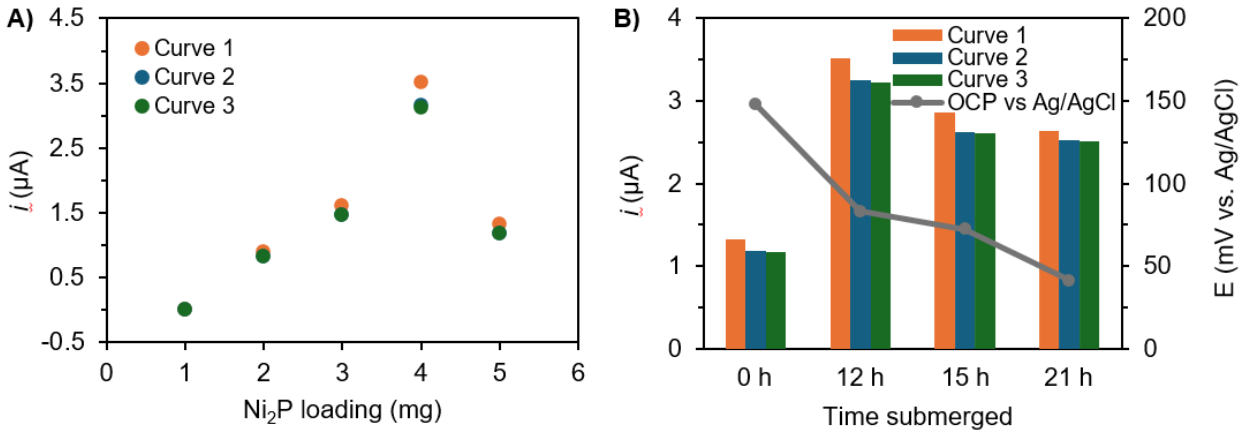

Figure 4.2. (A) Capacitive current at open circuit potential during 3 cycles of cyclic voltammetry at a scan rate of 1 V/s in 0.5 M H_2SO_4 for electrodes loaded with differing amounts of Ni_2P. Cyclic voltammetry experiments were performed on annealed Ni_2P after polarizing the catalyst to -0.5 V vs. Ag/AgCl. (B) Capacitive current at open circuit potential for the electrode deposited with 5 mg of Ni_2P over time. An overlay of the change in open circuit potential over the same amount of time is shown.

To investigate this decrease in capacitive current at 5 mg, we left the 5 mg sample in solution and ran the same CV experiment over the course of a day to see how capacitive current and open circuit potential changed over time (Figure 4.2B). After 12 h, the capacitive current in the 5 mg sample increased to match that of the 4 mg sample at 0 h (Figure 4.2A). However, when the 5 mg sample was probed after 15 h, the capacitive current decreased and continued declining through 21 h. Additionally, open circuit potential continuously decreased over 21 h of submersion in the electrolyte solution. We interpret these changes in the 5 mg sample as caused by the etching of an oxidized surface layer, which led to the initially low capacitive current and high open circuit potential for the 5 mg sample. Due to the oxidation of the 5 mg sample, it was impossible to determine the maximum loading on the electrodes definitively; however, we determined that at least up to 4 mg of Ni_2P was safe to deposit. Therefore, for future XAS experiments, we stacked multiple carbon fiber squares to meet the 16 mg of Ni_2P parameter mentioned above. Future experiments into the conductivity of Ni_2P nanoparticles on carbon fiber should test higher loadings in an oxygen-free environment.

Now that we had determined the optimal procedure for depositing Ni_2P electrodes, we performed our first electrochemical experiments in the cell by catalyzing the hydrogen evolution reaction (HER). We attempted to optimize the *operando* cell performance for HER by determining the maximum reductive potential we could apply while still removing H_2 bubbles on the electrode. By maximizing the reductive potential applied, we aimed to maximize HER current, thereby increasing the amount of Ni_2P involved in catalysis at any particular moment. At the same time, excessive polarization can lead to H_2 bubbles, which cause uneven X-ray absorption. To determine the maximum reductive potential, we ran a series of chronoamperometry experiments in 0.1 V increments starting at -0.2 V vs. Ag/AgCl and ending at -0.5 V vs. Ag/AgCl while flowing

electrolyte solution through the cell (Figure 4.3A). To set up the cell, we made the working electrode by stacking six 1×1 cm^2 squares cut from the center of 2×2 cm^2 squares. Each square was loaded with 3.4 mg Ni_2P, annealed, and dipped in electrolyte solution before being carefully stacked inside the cell. Next, the cell was pre-filled with electrolyte solution, and additional solution was flowed through the working electrode and counter electrode spaces. While 0.5 M H_2SO_4 flowed through the cell, we incremented the applied potential (Figure 4.3A). Bubbles were sufficiently removed at -0.2 and -0.3 V vs. Ag/AgCl; however, bubbles formed too quickly at more reductive potentials, as evidenced by the decrease in reductive current over time. In the end, we determined this system was not ideal for studying HER through *operando* XAS because of the inherent difficulties of probing Ni-H binding in Ni K-edge XAS and the low HER current at the maximum feasible applied potential (-0.3 V vs. Ag/AgCl). However, using this cell to study other catalytic systems could prove fruitful, especially in systems requiring less current or forming fewer bubbles, e.g., nitrate or carbon dioxide reduction reactions. Future testing in alternate conditions should be explored. Also of note, interruptions in electrolyte solution flow during chronoamperometry experiments resulted in significant and rapid drops in current due to bubble formation, again demonstrating the necessity of avoiding or removing bubbles.

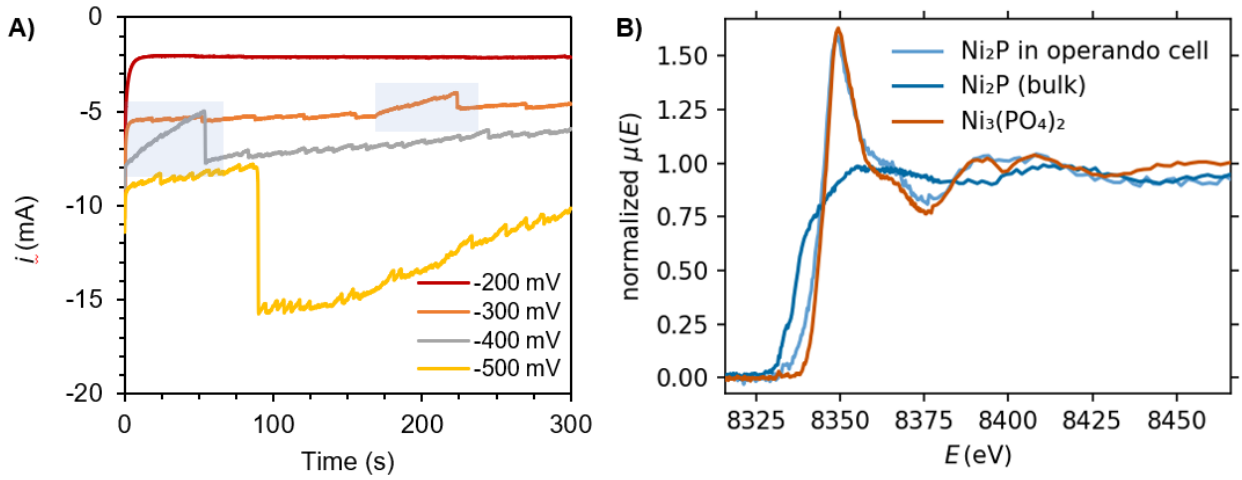

Figure 4.3. (A) Chronoamperometry of annealed Ni_2P in the *operando* cell while flowing 0.5 M H_2SO_4 through the cell. Blue highlighted regions show times when flow was not applied. (B) Normalized Ni K-edge X-ray absorption spectra of annealed Ni_2P nanoparticles in the *operando* cell after weeks of exposure to air and 0.5 M H_2SO_4 (light blue) compared to bulk Ni_2P (dark blue) and $Ni_3(PO_4)_2$ (brown).

Although studying HER via operando XAS was not feasible in our system, studying the electrochemical corrosion of Ni_2P would be an excellent use case for the operando cell because bubbles do not form on the working electrode, and changes in oxidation state are easily discernable in Ni K-edge XAS. Therefore, we performed *in situ* XAS on the same cell described in the previous experiment after weeks of exposure to air and 0.5 M H_2SO_4 (Figure 4.3B). The sample spectrum showed excellent signal-to-noise, demonstrating the efficacy of our cell preparation parameters. Additionally, the sample spectrum matched closely with $Ni_3(PO_4)_2$; therefore, we hypothesized that the electrochemical corrosion of Ni_2P in aqueous solutions would similarly oxidize to $Ni_3(PO_4)_2$. We later tested the corrosion of Ni_2P via *operando* XAS in a neutral phosphate-buffered electrolyte solution and generalized those results to acidic and basic pH. Further discussion of our application of the cell for *operando* Ni K-edge X-ray absorption spectroscopy is covered in Chapter 3.

4.2 Potentiodynamic Anodic Polarization to Study the Corrosion of Nanoparticle Materials

In situ and *operando* XAS can be a valuable tool for studying the electrochemical corrosion of materials.[9,10] Different materials and molecules often show distinctive XAS spectra that can be used as fingerprints or components in linear combination analyses to quantify speciation. Additionally, shifts in the edge energy of the spectra give information about evolving oxidation states and ligand environments for a given material or molecule. Changes in the edge step of spectra can also be used to approximate the dissolution rate of a material since the edge step is proportional to the thickness of the material present in the path of the X-ray beam. We can learn a lot about a material by coupling information from XAS and electrochemical techniques. Since benchtop XAS requires minutes to hours for a single scan and multiple scans are needed for high-quality data, chronoamperometry and chronopotentiometry are typical electrochemical techniques used in tandem with XAS. We can use *ex situ* potentiodynamic anodic polarization for electrochemical corrosion studies to determine which potentials to probe *in operando*. Through anodic polarization, we can learn about corrosion rates, passivation, and corrosion resistance. In anodic polarization curves, peaks (high corrosion rates) and plateaus (passivation regimes) signal that interesting chemistry is occurring that can be analyzed *in operando* via XAS.

Material scientists and engineers typically follow American Society for Testing and Materials (ASTM) standards for anodic polarization experiments with metals. These standards specify scan rates, experimental conditions, and more.[11–15] However, these standards serve only as starting points for corrosion analysis of advanced materials. Some important parameters for consistency across research studies include 1) deaerated electrolyte solutions, 2) long immersion times before polarization, and 3) slow scan rates. Using the ASTM standards as a foundation, we

established our procedure for the corrosion analysis of Ni_2P nanoparticles on carbon fiber paper. First, we sparged electrolyte solutions for 1 h with high-purity Ar while purging an N_2-purge glovebox to remove any O_2 dissolved in the electrolyte solution or the atmosphere of the glovebox. We moved the electrolyte solution to the glovebox after sparging for 1 h. Due to the air-sensitivity of Ni_2P nanoparticles, we placed Ni_2P electrodes in a closed container and moved them from an inert atmosphere glovebox into the N_2-purge glovebox. We did not open the container until the atmosphere in the N_2-purge glovebox had been purged for another hour. Then, we submerged the electrode in the electrolyte solution alongside a graphite-rod counter electrode and Ag/AgCl reference electrode calibrated to the H_2 redox couple. Before beginning anodic polarization experiments, we submerged the Ni_2P electrode for 1 h in the electrolyte solution or until OCP stabilized to within 1 mV/h, whichever occurred first. Finally, we polarized the electrode from OCP to 2 V vs. the reversible hydrogen electrode (RHE) (Figure 4.4).

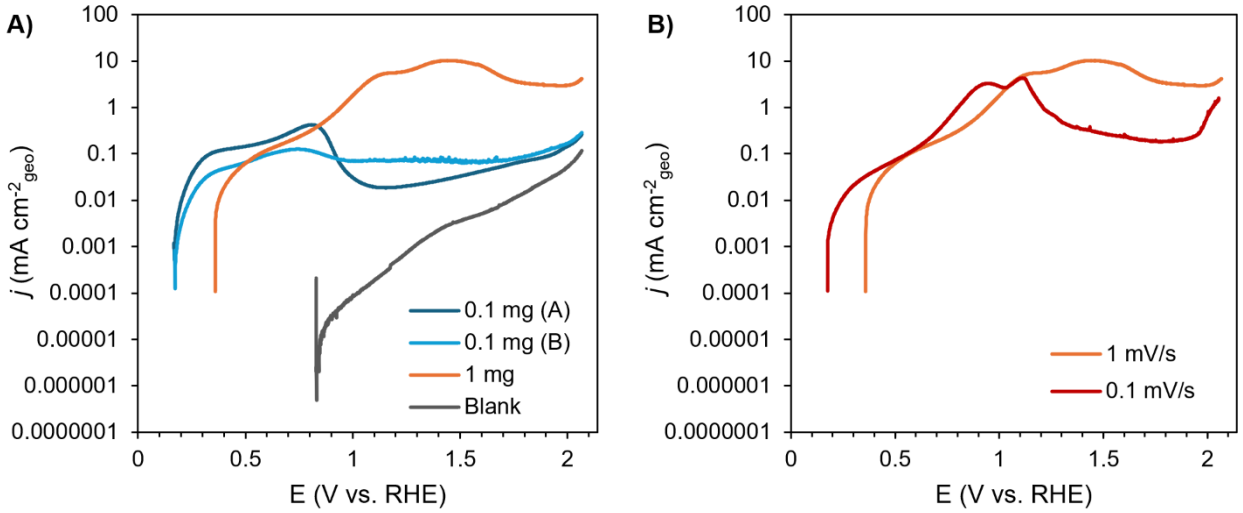

Figure 4.4. (A) Anodic polarization scans of varying amounts and sizes of annealed Ni_2P nanoparticles in 1 M neutral K_2HPO_4:KH_2PO_4 at a scan rate of 1 mV/s. Current densities were normalized to the geometric surface area of the electrode. (B) Anodic polarization scans of ~1 mg of annealed Ni_2P nanoparticles in 1 M neutral K_2HPO_4:KH_2PO_4 at varying scan rates. Current densities were normalized to the geometric surface area of the electrode.

In our anodic polarization experiments, we first compared the parameters of Ni_2P particle size and deposition quantities (Figure 4.4A). For the three samples in Figure 4.4A, nanoparticle sizes were 4.3 nm ± 0.8 nm (0.1 mg (A)), 3.2 nm ± 0.5 nm (0.1 mg (B)), and 11 nm (1 mg) (Figure 3.4, Figure 3.5). The three sample polarization curves differed in OCP, peak potentials, and peak current densities, indicating that size and deposition quantities play an important role in the corrosion of Ni_2P nanoparticles. Therefore, to compare *ex situ* and *operando* electrochemistry, we need to use consistent loadings and nanoparticle sizes. Individual carbon fiber squares in the *operando* cell require approximately 4 mg of Ni_2P for XAS measurements (approximately 1 mg in 0.5×1 cm^2 electrodes used in anodic polarization experiments), so these are the squares that we used as electrodes moving forward. Second, we lowered the scan rate to determine whether 1 mV/s was sufficiently slow for Ni_2P nanoparticles to reach a steady state during scans (Figure 4.4B). Lowering the scan rate to 0.1 mV/s resulted in lower peak potentials and, more importantly, more

well-defined peaks. These peaks can be used to determine promising potentials for chronoamperometry experiments during *operando* XAS. Consistent loadings and slow scan rates are essential when using *ex situ* anodic polarization experiments to inform *operando* XAS studies. We recommend these parameters as good starting points for electrochemical corrosion studies of materials similar to Ni_2P.

4.3 Air-free Sample Holders for Transmission-mode X-ray Absorption Spectroscopy Experiments

Acquiring high-quality X-ray absorption spectra can take a long time on benchtop spectrometers because of low photon flux. Scans often take hours, and air-sensitive materials might oxidize during an experiment. To mitigate the problem of oxidation from ambient conditions, we designed air-free sample holders (Figure 4.5). The sample holders are made with a 3D-printed clamshell design with a 2×2 cm^2 sample compartment and an optional insert for thinner/smaller samples. Samples can take the form of films deposited on low-attenuation substrates, e.g., carbon fiber paper or powders mixed with hexagonal boron nitride. The sample holder is sealed by a greased O-ring and secured by six hand-tightened screws, preserving an air-free environment when prepared inside an inert atmosphere glovebox.

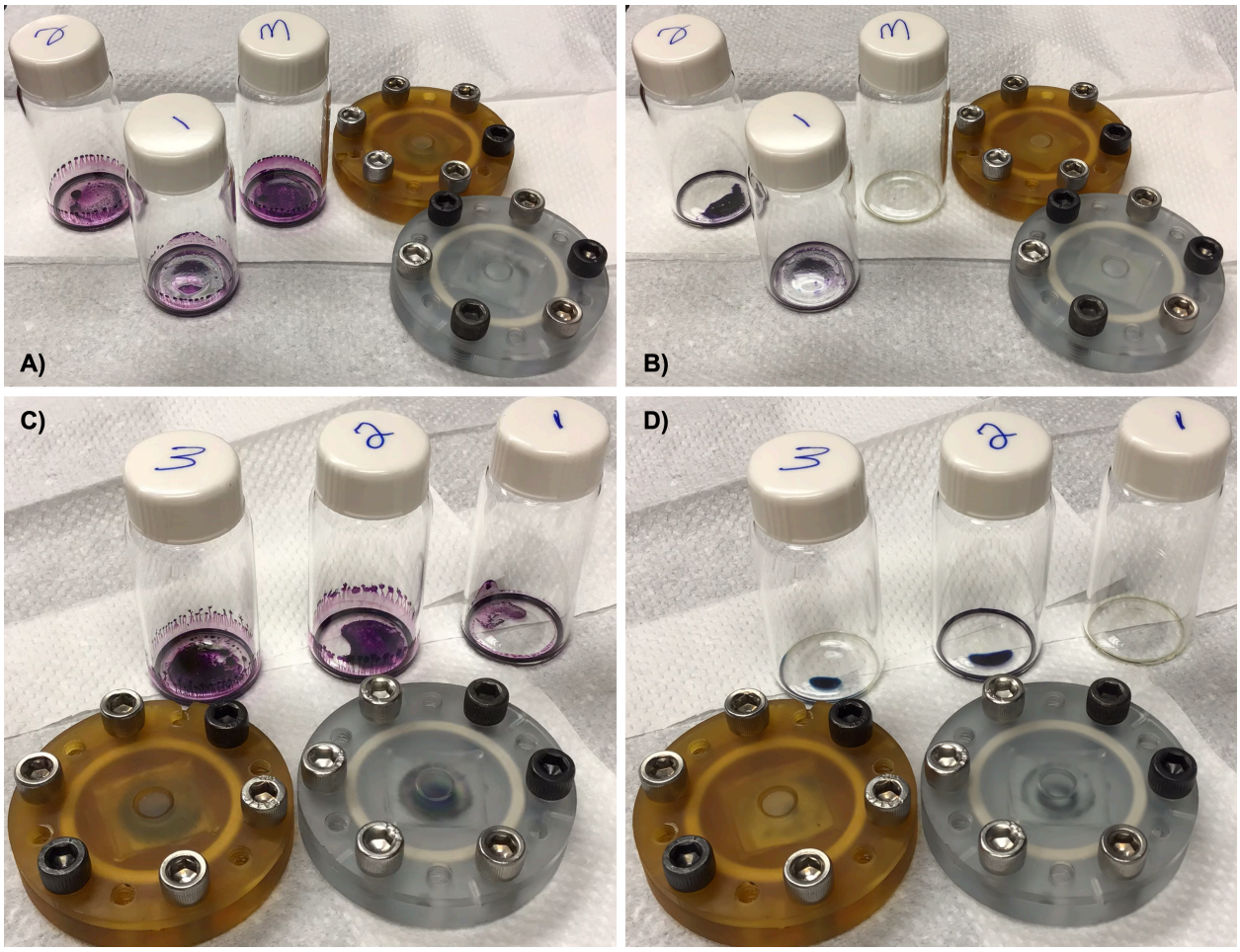

Figure 4.5. Two air-free sample holders for transmission-mode X-ray absorption spectroscopy and three scintillation vials were filled with a concentrated solution of benzophenone reduced by sodium metal and brought out into air. Before loading, air-free sample holders were placed under vacuum overnight. The color of the benzophenone solution had already dissipated significantly when the sample holders were initially brought out of the glovebox (A), and the color disappeared completely after 4 h (B). When the sample holders were placed under a vacuum for a week before loading and brought out into the air after loading (C), the solution's color lasted 4 h (D) and beyond.

To test the efficacy of these sample holders, we performed a ketyl test adapted from Carlson et al.[16] We dissolved benzophenone in tetrahydrofuran on the Schlenk line and dried it with molecular sieves. Then, inside an N_2-atmosphere glovebox, we added Na metal to the solution, which turned the solution into a deep purple color due to ketyl radical formation. We can use this

solution to test for air exclusion since the color disappears in the presence of oxidants like O_2 and H_2O. Inside the glovebox, we added the solution to concave glass slides, which we placed inside the sample holders. We then sealed the sample holders by greasing the O-ring and hand-tightening the screws before bringing them out into the ambient environment. In our initial tests, we brought the sample holders into the glovebox via overnight evacuation before filling them with the benzophenone solution. After loading the sample holders and bringing them out into the air, the benzophenone solution lost color after only 4 h (Figure 4.5A,B). We hypothesized that this result was due to the adsorption and/or absorption of O_2 and H_2O into the sample holders before we brought them into the glovebox. To address this problem, we evacuated the sample holders for one week before bringing them into the glovebox (Figure 4.5C,D). This evacuation procedure resulted in benzophenone retaining its color for 14.5 h, nearly four times as long as after the overnight evacuation procedure. From this result, we concluded that the air-free sample holders would effectively exclude air for XAS measurements of mild to moderately air-sensitive samples if properly evacuated before loading.

4.4 REFERENCES

(1) Singh, N.; Nguyen, M.-T.; Cantu, D. C.; Mehdi, B. L.; Browning, N. D.; Fulton, J. L.; Zheng, J.; Balasubramanian, M.; Gutiérrez, O. Y.; Glezakou, V.-A.; Rousseau, R.; Govind, N.; Camaioni, D. M.; Campbell, C. T.; Lercher, J. A. Carbon-Supported Pt during Aqueous Phenol Hydrogenation with and without Applied Electrical Potential: X-Ray Absorption and Theoretical Studies of Structure and Adsorbates. *J. Catal.* **2018**, *368*, 8–19. https://doi.org/10.1016/j.jcat.2018.09.021.

(2) Yang, Y.; Wang, Y.; Xiong, Y.; Huang, X.; Shen, L.; Huang, R.; Wang, H.; Pastore, J. P.; Yu, S.-H.; Xiao, L.; Brock, J. D.; Zhuang, L.; Abruña, H. D. In Situ X-Ray Absorption Spectroscopy of a Synergistic Co–Mn Oxide Catalyst for the Oxygen Reduction Reaction. *J. Am. Chem. Soc.* **2019**, *141* (4), 1463–1466. https://doi.org/10.1021/jacs.8b12243.

(3) Maniguet, S.; Mathew, R. J.; Russell, A. E. EXAFS of Carbon Monoxide Oxidation on Supported Pt Fuel Cell Electrocatalysts. *J. Phys. Chem. B* **2000**, *104* (9), 1998–2004. https://doi.org/10.1021/jp992947x.

(4) Cheaib, K.; Maurice, B.; Mateo, T.; Halime, Z.; Lassalle-Kaiser, B. Time-Resolved X-Ray Absorption Spectroelectrochemistry of Redox Active Species in Solution. *J. Synchrotron Radiat.* **2019**, *26* (6), 1980–1985. https://doi.org/10.1107/S1600577519013614.
(5) Lopez-Astacio, H.; Vargas-Perez, B. L.; Del Valle-Perez, A.; Pollock, C. J.; Cunci, L. Open-Source Electrochemical Cell for in Situ X-Ray Absorption Spectroscopy in Transmission and Fluorescence Modes. *J. Synchrotron Radiat.* **2024**, *31* (2), 322–327. https://doi.org/10.1107/S1600577524000122.
(6) Madigan, C. F.; Hebner, T. R.; Sturm, J. C.; Register, R. A.; Troian, S. Lateral Dye Distribution With Ink-Jet Dye Doping of Polymer Organic Light Emitting Diodes. *MRS Online Proc. Libr.* **2000**, *625* (1), 123. https://doi.org/10.1557/PROC-625-123.
(7) de Gans, B.-J.; Schubert, U. S. Inkjet Printing of Well-Defined Polymer Dots and Arrays. *Langmuir* **2004**, *20* (18), 7789–7793. https://doi.org/10.1021/la049469o.
(8) Sahu, P.; Prasad, B. L. V. Dilution Does the Trick: Role of Mixed Solvent Evaporation in Controlling Nanoparticle Self-Assembly. *Colloids Surf. Physicochem. Eng. Asp.* **2014**, *447*, 142–147. https://doi.org/10.1016/j.colsurfa.2014.01.070.
(9) Fayfar, S.; Zheng, G.; Sprouster, D.; Marshall, M. S. J.; Stavitski, E.; Leshchev, D.; Khaykovich, B. In-Situ Analysis of Corrosion Products in Molten Salt: X-Ray Absorption Reveals Both Ionic and Metallic Species. *ACS Omega* **2023**, *8* (27), 24673–24679. https://doi.org/10.1021/acsomega.3c03448.
(10) Lützenkirchen-Hecht, D.; Frahm, R. Corrosion of Mo in KOH: Time Resolved XAFS Investigations. *J. Phys. Chem. B* **2001**, *105* (41), 9988–9993. https://doi.org/10.1021/jp003414n.
(11) F04 Committee. Test Method for Conducting Cyclic Potentiodynamic Polarization Measurements to Determine the Corrosion Susceptibility of Small Implant Devices. https://doi.org/10.1520/F2129-24.
(12) G01 Committee. Reference Test Method for Making Potentiodynamic Anodic Polarization Measurements. https://doi.org/10.1520/G0005-14R21.
(13) G01 Committee. Test Method for Conducting Cyclic Potentiodynamic Polarization Measurements for Localized Corrosion Susceptibility of Iron-, Nickel-, or Cobalt-Based Alloys. https://doi.org/10.1520/G0061-86R24.
(14) J01 Committee. Terminology and Acronyms Relating to Corrosion. https://doi.org/10.1520/G0193-22.
(15) G01 Committee. Practice for Conventions Applicable to Electrochemical Measurements in Corrosion Testing. https://doi.org/10.1520/G0003-14R24.
(16) W. Carlson, A.; A. Primka, D.; D. Douma, E.; A. Bowring, M. Evaluation of Air-Free Glassware Using the Ketyl Test. *Dalton Trans.* **2020**, *49* (43), 15213–15218. https://doi.org/10.1039/D0DT02345K.

VITA

Ricardo hails from the beautiful island of Puerto Rico and the mighty state of New Jersey. He was first exposed to chemistry research during high school while working in the lab of Prof. Lisa Rodenburg at Rutgers University, studying the impact of polychlorinated biphenyls on the environment. Ricardo obtained a bachelor's of science in chemistry from Rice University in Houston, TX prior to beginning his PhD at the University of Washington. At Rice University, he worked in the labs of Prof. Lon Wilson and Prof. Angel Martí, where he was first introduced to materials chemistry research while working on boron nitride functionalization. While at the University of Washington pursuing his PhD, Ricardo happily married his wife, Sierra. After his PhD, he hopes to contribute to the materials chemistry industry in Seattle, especially in advancing clean energy efforts in the area.